CFD Simulation of Turbulent non-Newtonian Slurry Flows in Horizontal Pipelines

by

Mohsen Sadeghi

A thesis submitted in partial fulfillment of the requirements for the degree of

Master of Science

in

Chemical Engineering

Department of Chemical and Materials Engineering
University of Alberta

Abstract

Complex concentrated slurry flows in horizontal pipelines are widely seen in many industries for transportation of solid particles or process wastes. i.e., tailings. Slurry flows can occur in a turbulent regime, and the carrier fluid usually shows a non–Newtonian behavior. Understanding the flow behavior of slurries and the ability to predict the changes in the behavior with respect to variations in the flow conditions are of great importance and help the operators in pipeline design and optimization, and possibly developement of separation processes. CFD simulation is a powerful tool to study the multiphase slurry systems, and can be applied to a wide variaty of configurations, flow conditions, and number of phases. In this work, CFD models were developed using ANSYS® FLUENT 2020 R2 commercial package to investigate the flow behavior of slurries in laboratory and industrial scale pipelines.

The first part of this thesis investigates a model system in a lab–scale pipeline by studying the transport of monodisperse and bimodal particles in a turbulent non-Newtonian carrier using an Eulerian-Eulerian CFD model coupled with granular kinetic theory. The CFD predictions agreed satisfactorily with experimental data of solids concentration and pressure drop reported in the literature. The effects of the diameter of monodispersed particles (0.5-2 mm), solids concentration (0.1-0.4), mixture velocity (3-6 m/s), and carrier fluid density (1000-1400 kg/m^3) on flow

behavior and specific energy consumption were investigated. The mixture velocity has the most significant effect on pressure drop and radial solids distribution. An increase in mixture velocity or solids concentration led to a larger pressure drop, primarily due to the intensified particle-wall and particle-particle interactions. At the maximum velocity of 6 m/s, the solids concentration distribution reversed near the pipe invert with a local maximum in turbulent kinetic energy from a low solids concentration, while turbulence was dampened at the pipe core where the solids concentration is higher. A higher solids concentration and lower mixture velocity led to lower specific energy consumption.

In the second part, the work was extended to an indutrial–scale pipeline with the study of transport of three–phase oil sands tailings in a horizontal pipeline using the CFD technique via the mixture multiphase model coupled with the kinetic theory of granular flow. The solid particles and bitumen droplets are conveyed via a non–Newtonian carrier fluid in a turbulent regime inside an industrial–scale pipeline with 74 cm diameter and 220 m length. Ten sets of field data of velocity distribution and pressure drop were collected and used for the validation of the model. Overall, the CFD results showed exceptional agreement with the field data, with errors of $< 3.5\%$ for velocity distribution and $< 15\%$ for the pressure drop. A systematic parametric investigation was performed on the effect of mixture velocity, particles size distribution, non–Newtonian viscosity, and pipe angle on the carrier velocity distribution, pressure gradient, radial distributions of turbulent kinetic energy, and solids and bitumen concentration. Overall, our results showed the nontrivial effects of the mentioned parameters on the flow behavior, but less pronounced effects on the bitumen concentration distribution. Moreover, the majority of bitumen droplets

reside at the top region of the pipe thus selective treatment of the top flow may lead to an acceptable recovery of bitumen.

Overall, this thesis presents a reliable and affordable simulation approach for modeling turbulent non-Newtonian slurries. The results and findings of would be helpful to better understand the behavior two and three–phase slurry flows, and to optimize the slurry transport processes. Moreover, this thesis may help the design of new process for separation of bitumen residues from the tailings stream.

Preface

This thesis is my original. Some parts of this thesis are modified or directly from the following two manuscripts which I am the first author of:

1. **M. Sadeghi**, S. Li, E. Zheng, S. G. Sontti, P. Esmaeili, X. Zhang. "CFD Simulation of Turbulent non-Newtonian Slurry Flows in Horizontal Pipelines". *Industrial and Engineering Chemistry Research*, vol. 61, num. 15, p. 5324-5339 I was the main author of this work, responsible for data collection and analysis, writing and revisions. Shuo Li assited in writing the first draft, especially in the introdusction and methodology parts. S. G. Sontti and Enzu Zhaneg helped with validadtion and editing of the text and scientific analysis. P. Esmaeili contributed with technical advice, and X. Zhang was the supervisor and involved with conceptualization and edits. The introduction and methodology parts of this work have modified and included in Chapters 1 & 2, respectively. The results and discussions were included as Chapter 3 of this thesis.

   This work is available at https://doi.org/10.1021/acs.iecr.1c04471

2. **M. Sadeghi**, S. G. Sontti, E. Zheng, X. Zhang. "Computational fluid dynamics (CFD) simulation of three–phase non–Newtonian slurry flows in industrial horizontal pipelines". Submitted to *Chemical Engineering Journal*. I was the

main author of this work, responsible for data collection and analysis, writing the draft and revisions. S. G. Sontti was involved with writing–review and editing, and validation. E. Zheng contributed to this work by writing–review and editing, and X. Zhang was the supervisor in this study. The introduction and methodology parts of this work have modified and included in Chapters 1 & 2, respectively. The results and discussions were included as Chapter 4 of this thesis.

To my family, who are everything to me.

Acknowledgements

At first, I would like to express my most sincere gratitude to my supervisor, Dr. Xuehua Zhang for her continual support and valuable guidance throughout my master's program. I am forever grateful for the opportunity she gave me to join her research group and work under her supervision. This two-year program was an experience of lifetime for me. I learned so much on how to be a professional and think like a researcher, and could see my progress since the day I joined the "Soft Matter & Interfaces Research Group".

I acknowledge the funding support from the Institute for Oil Sands Innovation (IOSI) (Project Number IOSI 2019-04 (TA)) and from the Natural Science and Engineering Research Council of Canada (NSERC)-Alliance. This research was undertaken, in part, thanks to funding from the Canada Research Chairs Program.

I want to thanks Dr. Shuo Li and Dr. Somasekhara Goud Sontti whom I had the pleasure to collaborate and work with. I value their guidance and friendship and am grateful for the significant role they have had during my program as professional researchers I worked with.

I am also thankful to the past and present members of the Soft Matter & Interfaces group for their help, advice, support, and friendship. I am so delighted I had the chance to collaborate and be friends with them.

To my family, my mother and my father. This would not be possible without your support, encouragement, and love. I'm grateful for everything.

Table of Contents

List of Tables

List of Figures

List of Symbols

ΔP	area-averaged gauge pressure (M L^{-1} T^{-2}))
$\left\|\vec{v}_s'\right\|$	fluctuating solids velocity (L T^{-1})
$\overline{\overline{I}}$	second order unit tensor (–)
C_{fr}	friction coefficient between solid phases (–)
C_{vm}	virtual mass coefficient (–)
C_D	drag coefficient (–)
C_L	lift coefficient (–)
C_{vf}	chord-averaged solids concentration (–)
C_v	chord–averaged concentration (–)
D	pipe diameter (L)
d_p	particle diameter (L)
e	restitution coefficient (–)
F_{drag}	drag force per unit volume (M L^{-2} T^{-2})
F_{lift}	lift force per unit volume (M L^{-2} T^{-2})

F_{st} surface tension force per unit volume (M L^{-2} T^{-2})

F_{td} turbulent dispersion force per unit volume (M L^{-2} T^{-2})

F_{vm} virtual mass force per unit volume (M L^{-2} T^{-2})

g gravitational acceleration (L T^{-2})

g_0 radial distribution function (–)

i hydraulic gradient (–)

I_{2D} second invariant of the deviatoric stress tensor (–)

K fluid consistency coefficient (M L^{-1} T^{n-2})

K_{ls} momentum exchange coefficient between fluid and solid phase (–)

n flow behavior index (–)

p locally-averaged pressure (M L^{-1} T^{-2})

p_{fr} frictional pressure (M L^{-1} T^{-2})

R pipe radius (L)

t time (T)

v velocity (L T^{-1})

x horizontal coordinate (L)

y vertical coordinate (L)

z axial coordinate (L)

Greek Letters

α locally-averaged volume fraction (–)

α_v area-averaged solids concentration (–)

$\alpha_{s,\max}$ maximum packing limit (–)

α_v chord-averaged solids volume fraction (–)

β interphase drag coefficient between solid phases (M L^{-3} T^{-1})

$\dot{\gamma}$ shear strain rate (T^{-1})

η apparent viscosity (M L^{-1} T^{-1})

η_T turbulent viscosity (M L^{-1} T^{-1})

η_t turbulent diffusivity (–)

γ_{Θ_s} collisional dissipation of energy (E)

λ solid bulk viscosity (M L^{-1} T^{-1})

μ dynamic viscosity (M L^{-1} T^{-1})

ϕ_{ls} the energy exchange between the fluid and the solid phases (E)

ρ density (M L^{-3})

σ surface tension force (M L^{-2} T^{-2})

σ_t Prandtle/Schmidt number (–)

τ shear stress (M L^{-1} T^{-2})

Θ granular temperature (L^{-2} T^{-2})

φ angle of internal friction (–)

Subscripts

dr drift

ij	binary particles
l	liquid
m	mixture
p	p^{th} solid phase
q	q^{th} solid phase
s	solid
si	ith solid phase
sj	jth solid phase
ss	monodisperse particles
y	yield stress
col	collisional part of viscosity
fr	frictional part of viscosity
kin	kinetic part of viscosity

Abbreviations

BC boundary condition.

CFD computational fluid dynamics.

DNS direct numerical simulation.

ERT electrical resistance tomography.

FVM finite volume method.

KTGF kinetic theory of granular flow.

MFT mature fine tailings.

PSD particles size distribution.

QUICK quadratic upstream interpolation for convective kinematics.

RANS Reynolds averaged Navier–Stokes.

SEC specific energy consumption.

SIMPLE semi–implicit for pressure linked equations.

SST shear stress transport.

TKE turbulent kinetic energy.

UDF user–defined function.

VF velocity field.

Chapter 1

Introduction

1.1 Background

1.1.1 Multiphase slurry systems

Concentrated slurry flows are frequently encountered in many industries such as minerals extraction [2], food and farms [3], and petroleum [4]. Pipeline transport of slurry, due to its relatively high energy efficiency and low operating cost, has found applications in the long-distance transport of coal, tailings, among others [2, 5]. A slurry flow is a multiphase system where solid particles are transported via water as the carrier. In reality, the solid particles in the slurry are different in size, also called as polydisperse particles [2, 6]. High concentrations of solids can help meet the demand for the high volume of tailings to be transported to a specific site, where the recovery of water from tailings reduces the water consumption [7]. Considering the relevant flow velocities in the industry, and the pipeline characteristics, the transport process may occur in a turbulent regime. A turbulent slurry flow can be classified as a highly complex system, and development of a predictive model is of great importance for pipeline design and optimization of the transport process.

In the case of highly concentrated tailings, the carrier fluid typically exhibits visco-plastic non-Newtonian behavior due to the presence of fine particles (i.e., $d_p < 45\mu m$) in the tailings. The carrier possesses yield stress and viscosity that are a combined function of mineralogy, surface chemistry, particle size distribution, and shear history. The yield stress is also a strong function of solids concentration [7, 8]. According to Chhabra and Richardson [9], the transport of coarse particles in a laminar, non-Newtonian carrier fluid flow has two advantages: (i) the maximum apparent viscosity of a shear-thinning fluid occurs at the pipe center, which promotes particle suspensions so that less solids accumulate in the pipeline, and, (ii) the minimum apparent viscosity occurs at the pipe wall, which maintains relatively low frictional pressure loss associated with less energy consumption.

Particle suspensions are further facilitated by the presence of a yield stress. These advantages can also be extrapolated to the counterpart turbulent flow case as evidenced by the increasing turbulent viscosity from the pipe wall to pipe center – see Figures 5 e,f of Singh et al. [10]; these figures show the local viscosity contours of shear-thinning fluid in a round pipe using direct numerical simulations. Slower particle settling is anticipated away from the pipe wall where the fluid has a greater local viscosity. However, yield stress and the high viscosity are no longer available to support coarse particles once the carrier is sheared. Local viscosity reduces dramatically when the carrier is sheared, and studies such as the work by Arabi and Sanders [11] show that the particles are able to move freely relative to the carrier in such conditions.

1.1.2 Experimental studies of slurry flow behaviors

Several groups of researchers have conducted experimental, modeling, and simulation works to understand the slurry flow characteristics and optimize the process with various configurations and applications [12]. However, these type of studies have been performed mostly for two–phase slurries. Experimental investigations in pilot and lab–scale pipelines have been thoroughly reported in the literature for both Newtonian [13–18] and non–Newtonian [7, 19–21] carrier fluids. For a Newtonian carrier fluid, the researchers at the Saskatchewan Research Council have reported experimental data for slurry flows in various systems and different flow conditions [13–16], they extensively investigated the concentration distribution of coarse particles and determined the effect of flow parameters such as mixture velocity on the solids concentration distribution. Moreover, experimental data of concentration distribution and pressure drop has been presented by Kaushal et al. [17] and and Kaushal and Tomita [18] for flow velocities up to 5 m/s and solids volume fraction up to 0.5. Furthermore, Vlasák et al. [22] reported the pressure gradient and solids concentration distribution for turbulent flow inside inclined pipes, with flow velocities up to 2.07 m/s and solids volume fraction up to 0.34, where they identified insignificant changes in solids concentration distribution with relatively small changes in pipe inclination, e.g., less than 30°. Summaries of reported experimental data can be seen in Table 1 of Ekambara et al. [5] and Table 1 of Zhang et al. [23].

In the later studies of Kaushal et al. [17] and Kaushal and Tomita [18], their concentration measurements revealed that for fine particles, the maximum concentration occurs close to the pipe invert; for coarse particles, the maximum concentration oc-

curs away from the pipe invert. The latter effect is due to the presence of a near-wall lift force [24], which, as argued in Kaushal and Tomita [18], is a result of the viscous-turbulent interface interactions and enhanced particle-particle interactions. However, it is not possible to place any reliance on these concentration distributions results as the turbulence and particle interactions change significantly with the lift force. It is worth emphasizing that the layered models formulate force balances for each individual layer and solve the thickness and velocities of the individual layers. Although the recent advancements in noninvasive measurement techniques such as electrical resistance tomography (ERT) have increased the feasibility of the experimental studies, it is challenging to obtain detailed and reliable measurements of velocity and concentration distribution in high concentration suspensions due to limitations of current experimental techniques.

For the non–Newtonian carrier fluid, recently Pěník et al. [25] and Zheng et al. [7] reported the concentration distribution and pressure drop in a two–phase flow with a carrier fluid fitted with a Herschel–Bulkley model in a turbulent regime. The solids volume fractions were up to 0.2 and 0.16, and flow velocities were up to 4.51 and 3.67 m/s in the works by Pěník et al. [25], and Zheng et al. [7], respectively, and more symmetrical solids concentration distributions in case of higher mixture velocities were identified in both works. Matoušek et al. [26] used a Herschel–Bulkely carrier fluid to drive a solid bed to sliding and measured the pressure gradient and mean delivered solids concentration for flow velocities up to 4.76 m/s, and confirmed the suitability of a proposed two–layer model for the prediction of viscous frictions in a laminar regime. Moreover, Ignatenko et al. [21] reported only the pressure drop data for the Herschel–Bulkley carrier fluid in a turbulent regime with flow velocities

up to 5.2 m/s and particles concentration of 10%.

Turian et al. [27] presented experimental data of pressure gradient for both laminar and turbulent slurry flows with solids volume fraction up to 0.252 where the carrier fluid follows the Sisko rheological model. Studying the effect of mixture velocity on the pressure gradient is the common feature of the works by Ignatenko et al. [21], and Turian et al. [27], while the evolution of pressure gradient in full transition of laminar to turbulent flow was reported. For a power–law carrier fluid, Eesa and Barigou [20] measured the solid–phase velocity distribution in a laminar flow with outlet solids volume fraction up to 0.4 and flow velocities up to 125 mm/s. In their earlier study, Eesa and Barigou [19] they reported the velocity distribution in a similar system and flow conditions but with an Ellis carrier fluid, where they reported more symmetrical solid velocity distributions in the case of smaller solid particles and higher mixture velocities and solids concentration.

1.1.3 Modeling and computational fluid dynamics

As complement to experimental studies, the development of reliable models validated through a broad range of flow conditions is of great importance for understanding and predication of the slurry flow behavior. There are several sorts of models available for the prediction of slurry flow quantities in a pipe flow. It is well comprehended that different slurry flows exhibit somewhat different flow behaviors. Classifying the flow type is essential for successfully modeling slurry transport systems and predicting flow behavior in a pipeline. However, the available models rely on different approaches, which have different levels of complexity and refinement. Previous studies of Newtonian slurry flows cover theoretical, numerical and experimental aspects

with focal points on solids concentration distribution and frictional pressure drop. Key parameters that influence the flow behavior include particle size, solids concentration, and mixture velocity.

The attempts to simulate the slurry flow behavior started with the theoretical models and empirical and semi–empirical correlations. Gillies and Shook [14] conducted systematic experiments to measure the concentration distribution of coarse particles in radial direction, and proposed a method to predict the concentration distribution neglecting the particles interactions. In their other studies, they proposed an approach to predict the head loss called the two–layer model originated by Wilson [28] and extended it to various conditions [13, 15]. In Wilson [28]'s model, a stratified solid–liquid flow has been modeled assuming two separate layers in which the mixture was considered in single phase having uniform velocity and solid concentration. The layers can exchange momentum via shear stress at the interface, and mass and momentum balance equations are written and solved separately for each layer. Similarly, other groups of researchers have developed Two–Layer [29–31] and Three–Layer models [32, 33].

With the development of computational fluid dynamics (CFD), a number of numerical studies on pipeline slurry flows have been conducted [34, 35]. Compared to theoretical and laboratory experimental modeling, CFD is advantageous because it can provide detailed 3D flow results and is cost-effective to perform pipeline scale-up and parametric studies. Different multiphase flow modeling approaches such as Eulerian–Eulerian [5, 23, 34], Eulerian–Lagrangian [36–38], and mixture model [4, 21, 39] have been utilized. Recently, Messa and Matoušek [40] and Alobaid et al. [41] presented a comprehensive description and comparison of the multiphase modeling

approaches.

In the Eulerian–Eulerian (or Two–Fluid) model, the phases are treated as interpenetrating continua, and governing equations are applied to each phase while the phases can exchange momentum via interphase forces. The kinetic theory of granular flow is usually coupled with the Eulerian–Eulerian model to capture the effects of particles interactions on the flow field. This approach makes the consideration of chemical reactions and mass transfer between the phases possible, and offers a relatively good compromise between the computational cost and accuracy [41]. In the Eulerian–Lagrangian scheme, the particles, droplets or bubbles (based on the type of the secondary phase) are tracked individually, and Newton's law of motion is applied to each particle. This approach is especially applicable when the concentration of the secondary phase is dilute, otherwise the computational cost will be tremendous due to the high number of equations to be solved [41, 42]. The mixture model is a simplified Eulerian multiphase model that can be beneficial in modeling of complex multiphase systems , e.g., when the number of secondary phases is high or the interactions between the secondary phases are not well–known[43].

Despite the advantages of the Eulerian-Eulerian model, the fact that this model considers the particles as continua leads to the inability to represent the discrete nature of the solid phase. In the Lagrangian perspective, the particles trajectories are computed individually, and the interphase forces such as the drag force on particles are also calculated separately and summed for all of particles and more detailed particle-particle and particle wall collisions are provided. This more sophisticated treatment for the particles makes the Eulerian-Lagrangian method more successful in the prediction of solid distribution or other flow conditions in some applications.

The treatment of the multiphase mixture and lower number of differential equations to be solved, make the mixture model an efficient method for the systems with polydisperse particles and multiple phases [42]. Multiphase slurry systems, cyclone separators [44, 45], cavitation processes [46], and nanofluidics [47] are some examples of where the mixture model can be applied and has been used previously by other researchers. For the multiphase slurry systems, although numerous efforts have been made to develop models capable of predicting the flow behavior, the lack of a model which can capture the non–Newtonian behavior of the carrier and effects of particle size distribution (PSD) is sensed. Notably, the effects of an additional secondary phase and mutual effects of other phases and flow conditions on the additional phase is another aspect that is not studied in the open literature.

The choice of the multiphase model is always specific to the system being simulated and its conditions, the level of computational cost that can be afforded, and the objectives of the simulations.[43, 48] Whereas many CFD simulations consider only monodisperse particles, a few studies have attempted to describe bimodal [6, 49, 50] and multisized [51] particle distributions, by including momentum and energy exchanges between particles of different sizes.

Compared to the numerous studies on Newtonian slurry flows, the transport of coarse particles in a non-Newtonian carrier fluid has not been studied extensively, which is probably due to the complex interactions between particles and non-Newtonian carrier fluid [8]. In addition to the hydrodynamic conditions, the rheological parameters e.g. yield stress are also of paramount importance to determining the flow behavior. For a broad particle size distribution, Pullum et al. [52] divided the particle sizes into three categories according to the resulting flow patterns, i.e. carrier

equivalent fluid, heterogeneous and fully-stratified, which correspond to particle sizes $d_p < 200\mu$m, $200\mu\text{m} \leq d_p < 0.015D$ and $d_p > 0.015D$ where D is the pipe diameter, respectively. On this basis, Pullum et al. [52] proposed a three-component model to describe the overall pressure loss, whereby the pressure losses due to fine, coarse and coarser particles are assumed to be linearly additive. The three-component models of Pullum et al. [52] and Kesely [1] agree well with previous experimental measurements. A summary of experimental data found in the literature is given in Table 3.1 of the present document, where the carrier fluid is generally shear-thinning and is described with the Herschel-Bulkley model.

For CFD simulations, Eesa and Barigou [20] proposed an Eulerian-Eulerian CFD model that describes the transport of coarse, nearly neutrally-buoyant particles in a laminar power-law carrier fluid. Their parametric study shows that particle diameter and concentration have more significant effects on the flow regime, solids radial distribution and pressure drop compared to the rheological parameters. Bossio et al. [53] simulated horizontal pipeline (turbulent) slurry flows where the non-Newtonian carrier fluid is described by a three-parameter Sisko model. Bossio et al. considered monodisperse particle diameter of 0.11 mm and mean solids concentrations below 10%. They have validated their model only against the experimental data for the pressure drop, and their CFD simulation results of pressure drop are in accord with the measured data of Turian et al. [27]. Noticeably, their predicted solids radial concentration experiences a sharp reversal near the pipe invert and reduces to almost zero near the pipe obvert. Also shown in their concentration profile is that the concentration reaches a local maximum near the pipe center, where the turbulent kinetic energy reaches its minimum.

A more recent CFD study of non-Newtonian fluid and coarse particles two-phase flow has been performed by Ignatenko et al. [21]. Ignatenko et al.'s multiphase model is the mixture model, similar to but simpler than the Eulerian-Eulerian model. Specifically, the mixture model assumes that the phases are in equilibrium, and as a result, only one set of governing equations is used. Ignatenko et al.'s CFD prediction of pressure drop agrees satisfactorily with previous measurements for specified non-Newtonian rheology. Although they have validated their model against the experimental measurements of solid concentration distribution and radial velocity distribution for the Newtonian fluid, for the non-Newtonian case, the pressure drop is the only parameter they have used for validation.

1.2 Motivation

The previous CFD work has focused primarily on laminar flow [20] or turbulent flow but with model validation only for rather limited pipeline operating conditions [21, 53]. Moreover, these studies are restricted to monodisperse particles, whereas the case of non-Newtonian carrier fluid and bimodal or multisized particles is not thoroughly studied. Turbulent flow is of interest because either pseudo-homogeneous or heterogeneous suspension is made possible for solids transported under turbulent conditions [2]. It must be noted that the thickened tailings carrier is often irreversibly broken down in pumps and has reduced viscosity. Due to the wide range of industrially relevant velocities, these flows in a pipe can occur in a turbulent regime. The flow regime and fundamental flow mechanisms dictate the selection of the modeling approach to be used in numerical simulations. Particle size and size distribution are also expected to have nontrivial effects on the flow patterns [1, 52].

The oil sands tailings slurry is a byproduct of bitumen extraction, a mixture with three phases consisting polydisperse solid particles (about 55 wt%), water, and a minute fraction of residual bitumen (about 1 wt%) [54, 55]. The oil sands tailings are transported to large open areas called tailings ponds and stored so the particles settle, the water is recycled, and the land could be reclaimed. However, the residual bitumen in the slurry is not treated and separated, and can pose substantial threats to the environment, including decomposition into greenhouse gases and contribution to the global warming [56]. In this regard, separation of bitumen from the tailings before disposal to the tailings ponds is crucial. Understanding the behavior and the effective parameters of the tailings flow is a significant step toward designing a separation technology. Nevertheless, the complexity of the mixture and the low fraction of bitumen in the slurry makes the separation process difficult. There is no predictive model for the transport characteristics of slurry flow in large–diameter pipes, especially for multiple secondary phase solids along with bitumen droplets. Importantly, the effects of PSD and Casson viscosity have not been studied thoroughly in a complex multiphase flow system. Therefore, in depth understanding of slurry flow characteristics and operating conditions are important to design a suitable process.

1.3 Thesis objectives

At the first step, this study aims to: (i) establish an Eulerian-Eulerian CFD model that describes the pipeline turbulent transport of monodisperse or bimodal particles in a non-Newtonian fluid, which is validated for relatively wide ranges of particle size, area-averaged solids concentration, and rheological properties; (ii) perform a parametric study that reveals the effects of some of the key parameters that can be

managed in the pipeline operation, which in this study are particle size, area-averaged solids concentration, mixture velocity and carrier fluid density on the two-phase flow field. The parametric study section is focused on the investigation of the impact of the mentioned parameters on the slurry flow behavior individually, aiming to improve transport efficiency.

In the later part of this study, modeling of a turbulent three–phase tailings slurry flow with highly concentrated polydisperse solid particles and a non–Newtonian carrier fluid in an industrial–scale pipeline is aimed. After successful validation of the model, a systematic parametric study will be performed to investigate the effect of mixture velocity, particle size distribution, Casson viscosity, and pipe angle on the flow behavior. To the best of our knowledge, the present study is a first–of–a–kind on highly concentrated slurry transport in a industrial pipeline. The results of this study would contribute to better understanding of three–phase slurry system and may be used for pipeline design and optimization, as well as a guideline for designing a separation process inside the pipeline.

1.4 Thesis outline

In Chapter 1, a comprehensive description of the concentrated slurry flow features and the types of studies reported in the literature to study the slurry flow behavior is presented. Different modeling and CFD approaches have been introduced and compared and their implementation by other researchers has been cited. The motivation and objectives of this thesis have also been mentioned in Chapter 1. Chapter 2 provides a detailed description of the models and equations used in the CFD simulation, and the numerical approaches to solve the equations. The momentum balance equa-

tions in Eulerian-Eulerian and mixture multiphase models including the interphase forces and the KTGF sub–models are elaborated in Chapter 2. Chapter 3 presents the results of Eulerian-Eulerian modeling of two-phase flow with monodisperse coarse solid particles conveyed by a Herschel–Bulkley carrier fluid in turbulent regime in a lab–scale pipe including model validation and parametric study. In Chapter 4, the work has been extended to the simulation of a three-phase slurry flow with polydisperse solid particles in a turbulent regime on an industrial scale using the mixture model. The model validation with field data and parametric study are also presented in Chapter 4. Chapter 4 highlights the key findings and contributions of this work and the results presented in Chapters 3 and 4, along with discussions about the potential future works.

Chapter 2

Methods and procedures

2.1 Eulerian–Eulerian approach for model systems

A 3D transient Eulerian-Eulerian CFD model is employed for simulation of the hydrotransport of non-Newtonian slurry flow in a horizontal pipeline. Both liquid and solid phases are treated as mutually interpenetrating continua within the Eulerian approach. The transient simulation helps to identify the possible formation of a solid bed at the pipe invert. Particle-particle interactions are described by kinetic theory of granular flow, whereby a transport equation for the granular temperature (Eq. (2.4) d) is derived and solved. Standard models provided by Ansys Fluent 2020 R2 are used to describe the interactions between phases and particles themselves. A list of all of the equations and models used in this study is presented in this section.

2.1.1 Mass and momentum conservation equations

The governing equations used in the model are summarized in Table 2.1. The model consists of the volume-averaged mass and momentum conservation equations for each phase (Eqs. (2.1)-(2.3) in Table 2.1), this assuming that the flow is isothermal,

incompressible and has no phase change and chemical reaction. The model considers momentum exchange between the liquid and solid phases via interphase forces. In addition, constitutive relationships are provided for solid pressure and viscous stresses due to particles based on the kinetic theory of granular flow. Appropriate closure laws are taken into account to describe interphase momentum exchange, turbulence, solids pressure, and the physical properties of each phase.

Interphase interaction forces such as drag (Eqs. (2.2)b and (2.3)c), added mass (Eqs. (2.2)c and (2.3)d) and turbulent dispersion (Eqs. (2.2)d and (2.3)e) are added to the momentum equations. The effect of surface tension between two phases in the domain was included by enabling the surface tension force modeling. A source term will be added to the momentum conservation equations for both liquid and solid phases. This term (Eqs. (2.2)e and (2.3)f) is based on the continuum surface force proposed by Brackbill et al. [57] that was adjusted for the Eulerian-Eulerian model here. The velocity difference between the primary and secondary phases gives rise to the drag force, whereas velocity gradients in the flow field of the primary phase result in the lift force acting on the secondary phase. Likewise, the Eulerian CFD model involves turbulent dispersion force in two-phase turbulent flows to take into account the interphase turbulent momentum transfer, which arises from averaging the interphase drag term – see Eq. (2.2)d in Table 2.1 [58].

Turbulence in the continuous phase has a direct effect on the secondary phase (solid particles here) due to the interactions between the turbulent eddies and solid particles. Several papers in literature have proved the importance of including the turbulent dispersion force in the modeling of the pipeline transport of the slurry flows, especially its effect on the accuracy of solid concentration distribution.[5, 59,

60] Previous researches have revealed that lift force is negligible compared to drag force [5, 61, 62], thus lift force is not included in the current CFD simulation. For the drag force, the Gidaspow model [58] is chosen for all of the cases. The Gidaspow drag model is a combination of the Wen-Yu and Ergun models. This model is suitable for particulate systems and is widely used in the literature for the simulation of slurry flows and fluidized beds [5, 63–65].

2.1.2 Kinetic theory of granular flow

Particles are assumed to be smooth, spherical, inelastic, and to undergo binary collisions. Analogous to the kinetic theory of gases, the granular temperature (Eq. (2.4)c) is defined to quantify how the random and fluctuating movement of particles constitutes temperature. Granular temperature is determined by a transport equation in the general form of Eq. (2.4)d. The left-hand side of this equation determines the net change in the fluctuating energy. On the right-hand side of this equation, there are four terms for the generation and dissipation of energy: the generation of energy by the solid stress tensor, the diffusion of energy, the collisional dissipation of energy, and the energy exchange between the fluid and solid phases, respectively. Calculating of the granular temperature by solving this differential equation could be challenging; hence a simpler algebraic form of this equation is solved. In this approach, the diffusion and convection terms in Eq. (2.4)d are neglected and a local equilibrium in generation and dissipation of energy is assumed (Eq. (2.4)e). In Eq. (2.4)e, the first term in the right hand side is the generation of energy by the solid stress tensor, the collisional dissipation of energy is given by Eq. (2.4)f, and the energy exchange between the fluid and solid phases is given by Eq. (2.4)g.[5, 43, 50, 66] Table 2.2

Table 2.1: Mass and momentum equations for the Eulerian-Eulerian model employed in the CFD simulation. The equations are taken from *ANSYS FLUENT Theory Guide 15.0* [43].

Continuity

$$\frac{\partial}{\partial t}\left(\rho_q \alpha_q\right) + \nabla \cdot \left(\rho_q \alpha_q \vec{v}_q\right) = 0\,, \quad (q = l, s) \tag{2.1a}$$

$$\alpha_l + \alpha_s = 1 \tag{2.1b}$$

Momentum (liquid)

$$\frac{\partial}{\partial t}\left(\alpha_l \rho_l \vec{v}_l\right) + \nabla \cdot \left(\alpha_l \rho_l \vec{v}_l \otimes \vec{v}_l\right) = -\alpha_l \nabla p + \rho_l \alpha_l \vec{g} + \nabla \cdot \tau_l + \vec{F}_{\text{drag},l} + \vec{F}_{\text{vm},l} + \vec{F}_{\text{td},l} + \vec{F}_{\text{st},l} \tag{2.2a}$$

$$\vec{F}_{\text{drag},l} = \frac{3}{4} C_D \alpha_s \rho_l \frac{\|\vec{v}_l - \vec{v}_s\|}{d_p}\left(\vec{v}_l - \vec{v}_s\right) \tag{2.2b}$$

$$\vec{F}_{\text{vm},l} = C_{\text{vm}} \alpha_s \rho_l \left(\vec{v}_l \cdot \nabla \vec{v}_l - \vec{v}_s \cdot \nabla \vec{v}_s\right) \tag{2.2c}$$

$$\vec{F}_{\text{td},l} = \frac{3}{4} \frac{C_D \mu_{t,l}}{d_p \sigma_{t,l}} \alpha_s \|\vec{v}_l - \vec{v}_s\| \left(\frac{\nabla \alpha_s}{\alpha_s} - \frac{\nabla \alpha_l}{\alpha_l}\right) \tag{2.2d}$$

$$\vec{F}_{\text{st},l} = \sigma_{l,s} \kappa_l \nabla \alpha_l \tag{2.2e}$$

Momentum (solid)

$$\frac{\partial}{\partial t}\left(\alpha_s \rho_s \vec{v}_s\right) + \nabla \cdot \left(\alpha_s \rho_s \vec{v}_s \otimes \vec{v}_s\right) = -\alpha_s \nabla p - \nabla p_s + \rho_l \alpha_s \vec{g} + \nabla \cdot \tau_s + \vec{F}_{\text{drag},s} + \vec{F}_{\text{vm},s} + \vec{F}_{\text{td},s} + \vec{F}_{\text{st},s} \tag{2.3a}$$

$$\tau_s = \alpha_s \mu_s \left(\nabla \vec{v}_s + \left(\nabla \vec{v}_s\right)^T\right) + \alpha_s \left(\lambda_s - \frac{2}{3}\mu_s\right)\left(\nabla \cdot \vec{v}_s\right) \overline{\overline{I}} \tag{2.3b}$$

$$\vec{F}_{\text{drag},s} = -\vec{F}_{\text{drag},l} \tag{2.3c}$$

$$\vec{F}_{\text{vm},s} = -\vec{F}_{\text{vm},l} \tag{2.3d}$$

$$\vec{F}_{\text{td},s} = -\vec{F}_{\text{td},l} \tag{2.3e}$$

$$\vec{F}_{\text{st},s} = \sigma_{l,s} \kappa_s \nabla \alpha_s \tag{2.3f}$$

---

presents a frequently used model whereby the solids bulk viscosity (Eq. (2.4) a[67]), solids pressure (Eq. (2.4) h[58]) and granular viscosity (Eqs. (2.4)i) are expressed

explicitly. The solids pressure can be decomposed into two parts that are due to the streaming and collisions of particles, respectively. The granular viscosity consists of three parts, which are due to, respectively, particle collision (Eq. (2.4) j[68]), movement (Eq. (2.4) k[68]) and friction (Eq. (2.4) l[69]).

Table 2.2: Kinetic theory of granular flow employed in the Eulerian–Eulerian model [43].

$$\lambda_s = \frac{4}{3}\alpha_s^2 \rho_s d_p g_{0,ss} \left(1 + e_{ss}\right) \left(\frac{\Theta_s}{\pi}\right)^{1/2} \tag{2.4a}$$

$$g_{0,ss} = \left[1 - \left(\alpha_s / \alpha_{s,\max}\right)^{1/3}\right]^{-1} \tag{2.4b}$$

$$\Theta_s = \frac{1}{3}\left\|\vec{v}_s'\right\|^2 \tag{2.4c}$$

$$\frac{3}{2}\left[\frac{\partial}{\partial t}\left(\alpha_s \rho_s \Theta_s\right) + \nabla \cdot \left(\alpha_s \rho_s \vec{v}_s \Theta_s\right)\right] = \left(-p_s \overline{\overline{I}} + \overline{\overline{\tau_s}}\right) : \nabla \vec{v_s} + \nabla \cdot \left(k_{\Theta_s} \nabla \Theta_s\right) - \gamma_{\Theta_s} + \phi_{ls} \tag{2.4d}$$

$$0 = \left(-p_s \overline{\overline{I}} + \overline{\overline{\tau_s}}\right) : \nabla \vec{v_s} - \gamma_{\Theta_s} + \phi_{ls} \tag{2.4e}$$

$$\gamma_{\Theta_s} = \frac{12\left(1 - e_{ss}^2\right) g_{0,ss}}{d_p \pi^{1/2}} \rho_s \alpha_s^2 \Theta_s^{3/2} \tag{2.4f}$$

$$\phi_{ls} = -3 K_{ls} \Theta_s \tag{2.4g}$$

$$p_s = \alpha_s \rho_s \Theta_s + 2\rho_s \left(1 + e_{ss}\right) \alpha_s^2 g_{0,\mathrm{ss}} \Theta_s \tag{2.4h}$$

$$\mu_s = \mu_{s,\mathrm{col}} + \mu_{s,\mathrm{kin}} + \mu_{s,\mathrm{fr}} \tag{2.4i}$$

$$\mu_{s,\mathrm{col}} = \frac{4}{5}\alpha_s \rho_s d_p g_{0,\mathrm{ss}} \left(1 + e_{ss}\right) \left(\frac{\Theta_s}{\pi}\right)^{1/2} \alpha_s \tag{2.4j}$$

$$\mu_{s,\mathrm{kin}} = \frac{10\rho_s d_p \left(\Theta_s \pi\right)^{1/2}}{96\alpha_s \left(1 + e_{ss}\right) g_{0,\mathrm{ss}}} \left[1 + \frac{4}{5} g_{0,\mathrm{ss}} \alpha_s \left(1 + e_{ss}\right)\right]^2 \alpha_s \tag{2.4k}$$

$$\mu_{s,\mathrm{fr}} = \frac{p_{\mathrm{fr}} \sin \varphi}{2 I_{2D}^{1/2}} \tag{2.4l}$$

2.1.3 Turbulence model

The choice of turbulence model always compromises accuracy and computational cost. Considering the numerical stability and computational cost, from the turbulence models available in Ansys Fluent for the Eulerian-Eulerian model, the Two-Equation models (k-ϵ and k-ω) are the most promising. The choice of the turbulence model between these Two-Equation models has been widely discussed in the literature for different engineering applications.[70–72] The SST k-ω model shows a better performance in the near-wall region compared to the k-ϵ model, which is of great importance in this work. The k-ϵ model tends to overestimate the eddy viscosity in the near-wall region, but the k-ω model accounts for the transport effects of the principal turbulent shear stress, making it more accurate for modeling the near-wall turbulence.[73] In the present study, it is found that using the SST k-ω model, the CFD simulations converge relatively fast (compared to e.g. k-ϵ models) for most of the cases considered in Table 3.1, while the agreement between CFD and experiment is satisfactory – see the model validation described in section 3.2 below.

Generally, for modeling turbulence in a two-phase or multiphase slurry system, consideration of the computational cost and numeral stability are the most important aspects. Several researchers successfully implemented two-phase slurry systems using SST k-ω model in the open literature[59, 74–77], and tested the performance between k-ω and SST k-ω modeled to select the SST k-ω model. In this study, only the SST k-ω turbulence model is considered. The detailed theory underlying the SST k-ω model is referred to Chapter 4 of Ansys Fluent Theory Guide 15.0[43]. Note that the turbulence in the two-phase flow is modeled based on the mixture level,

assuming that all phases share the same turbulent flow field [78]. Based on Ansys Fluent Theory Guide 15.0[43], the mixture turbulence model is appropriate when the densities of phases are close. In our system, the primary phase (carrier fluid) density is 1 specific gravity, approximately half of the density of the solid phase (2.4 - 2.6). Under these conditions, mixture properties (velocity, mixture density, and dynamic viscosity) are sufficient to capture the crucial characteristics of the turbulent flow behavior. Although the turbulence modeling of each phase is also applied to multiphase systems,[7, 79] when applied to our system, both k and ω have to be solved for each phase, which may increase the computational time and complicate the potential issues from convergence or numerical instability.

2.1.4 Rheological model for the carrier fluid

The shear stress for the liquid phase, i.e. τ_l, remains to be specified as a closure condition to the governing equations. The Herschel-Bulkley model is adapted to describe the rheology of the non-Newtonian carrier fluid, which is mathematically by [80]

$$\begin{aligned} \tau_l &= \tau_y + K\dot{\gamma}^n \qquad \text{for } \|\tau_l\| > \left\|\tau_y\right\| \\ \dot{\gamma} &= 0 \qquad\qquad\quad \text{for } \|\tau_l\| < \left\|\tau_y\right\| \end{aligned} \tag{2.5}$$

where τ_y is the yield stress, $\dot{\gamma}$ is the shear strain rate, K and n are empirical constants and are named as the fluid consistency coefficient and flow behavior index, respectively. Assuming $n = 1$, (2.5) reverts to the linear relation, which corresponds to the Bingham plastic model. The underlying approach of this study assumes that suspensions can be described as mixtures of a carrier fluid and coarse conveyed particles[52]. The carrier fluid is usually water in mining applications plus the rheologically active

fine particles, which lead to non-Newtonian behavior. The shear-thinning behavior of this carrier is described with the Herschel-Bulkley rheological model (Eq. (2.5)). All other solid particles are conveyed as a coarse burden (e.g., 0.5 to 2 mm in this study) and will not affect rheology.

2.1.5 Bimodal particles

For bimodal particles, two secondary (solid) phases can be defined within the Eulerian-Eulerian model. The word 'bimodal' refers to two groups of particles, and in each group, the particles are the same in size and density. Compared to monodisperse particles, we should add specific terms that describe (i) the drag force between solid phases and (ii) the kinetic theory of granular flow that involves more than one particle size. To this end, the modified momentum equation and kinetic theory of granular flow are listed in Table 2.3. The drag force between the two solid phases is given by Eq. (2.6) b [81]. Eq. 2.7 presents the solution to the kinetic theory of granular flow for binary particles. The radial distribution function, $g_{0,ij}$ (Eq. (2.7) c), is a combination of $g_{0,ii}$ and $g_{0,jj}$, which are the respective radial distribution functions for the i^{th} and j^{th} solid phases. In the algebraic form of the granular temperature transport equation (Eq. (2.7) e), ϕ_{li} is the energy exchange between l^{th} solid or liquid phase and i^{th} solid phase. The maximum packing limit for binary mixtures, $\alpha_{s,\max}$ (Eq. (2.7) b), is referred to Eqs. (18.321) to (18.323) of Ansys Fluent Theory Guide 15.0[43]. For the solution strategy for bimodal particles, we adopted first-order upwind discretization scheme for the momentum equation, volume fraction, turbulent kinetic energy and turbulent specific dissipation energy as a compromise between accuracy and computational cost.

Table 2.3: Momentum equation and kinetic theory of granular flow for binary particles [43].

Momentum (ith solid phase)

$$\frac{\partial}{\partial t}\left(\alpha_{si}\rho_{si}\vec{v}_{si}\right)+\nabla\cdot\left(\alpha_{si}\rho_{si}\vec{v}_{si}\otimes\vec{v}_{si}\right)=-\alpha_{si}\nabla p-\nabla p_{si}+\rho_l\alpha_{si}\vec{g}+\nabla\cdot\tau_{si}+\vec{F}_{\mathrm{drag},si}+\vec{F}_{\mathrm{vm},si}+\vec{F}_{\mathrm{td},si}+\vec{F}_{\mathrm{st},si}+\beta_{ij}\left(\vec{v}_{sj}-\vec{v}_{si}\right) \tag{2.6a}$$

$$\beta_{ij}=\frac{3\left(1+e_{ij}\right)\left(\frac{\pi}{2}+C_{\mathrm{fr},ij}\frac{\pi^2}{8}\right)\alpha_{si}\rho_{si}\alpha_{sj}\rho_{sj}\left(d_{si}+d_{sj}\right)^2 g_{0,ij}}{2\pi\left(\rho_{si}d_{si}^3+\rho_{sj}d_{sj}^3\right)}\left\|\vec{v}_{si}-\vec{v}_{sj}\right\| \tag{2.6b}$$

kinetic theory of granular flow (ith solid phase)

$$\lambda_s=\frac{4}{3}\alpha_{si}^2\rho_{si}d_{si}g_{0,ii}\left(1+e_{ij}\right)\left(\frac{\Theta_{si}}{\pi}\right)^{1/2} \tag{2.7a}$$

$$g_{0,ii}=\left[1-\left(\sum_{i=1}^{2}\alpha_{si}/\alpha_{\mathrm{s,max}}\right)^{1/3}\right]^{-1}+\frac{d_{si}}{2}\sum_{i=1}^{2}\frac{\alpha_{si}}{d_{si}} \tag{2.7b}$$

$$g_{0,ij}=\frac{d_{si}g_{0.ii}+d_{sj}g_{0,jj}}{d_{si}+d_{sj}} \tag{2.7c}$$

$$\Theta_{si}=\frac{1}{3}\left\|\vec{v}_{si}'\right\|^2 \tag{2.7d}$$

$$0=\left(-p_{si}\bar{\bar{I}}+\overline{\overline{\tau_{si}}}\right):\nabla\vec{v}_{si}-\gamma_{\Theta_{si}}+\phi_{li} \tag{2.7e}$$

$$\gamma_{\Theta_s}=\frac{12\left(1-e_{ii}^2\right)g_{0,ii}}{d_{si}\pi^{1/2}}\rho_{si}\alpha_{si}^2\Theta_{si}^{3/2} \tag{2.7f}$$

$$\phi_{li}=-3K_{li}\Theta_i \tag{2.7g}$$

$$p_{si}=\alpha_{si}\rho_{si}\Theta_{si}\left[1+2\sum_{j=1}^{2}\left(\frac{d_{si}+d_{sj}}{2d_{si}}\right)^3\left(1+e_{ij}\right)\alpha_{sj}g_{0,ij}\right] \tag{2.7h}$$

$$\mu_{si}=\mu_{si,\mathrm{col}}+\mu_{si,\mathrm{kin}}+\mu_{si,\mathrm{fr}} \tag{2.7i}$$

$$\mu_{si,\mathrm{col}}=\frac{4}{5}\alpha_{si}\rho_s d_{si}g_{0,\mathrm{ii}}\left(1+e_{ij}\right)\left(\frac{\Theta_{si}}{\pi}\right)^{1/2}\alpha_{si} \tag{2.7j}$$

$$\mu_{si,\mathrm{kin}}=\frac{10\rho_{si}d_{si}\left(\Theta_{si}\pi\right)^{1/2}}{96\alpha_{si}\left(1+e_{ij}\right)g_{0,\mathrm{ii}}}\left[1+\frac{4}{5}g_{0,\mathrm{ii}}\alpha_{si}\left(1+e_{ii}\right)\right]^2\alpha_{si} \tag{2.7k}$$

$$\mu_{si,\mathrm{fr}}=\frac{p_{si}\sin\varphi_{si}}{2I_{2D}^{1/2}} \tag{2.7l}$$

2.1.6 Numerical methodology

The simulations were conducted using ANSYS® FLUENT 2020 R2 CFD software. The pressure-based unsteady state solver was used along with the closure laws to develop a multiphase Eulerian formalism. The pressure-velocity coupling was performed with Semi-Implicit for Pressure Linked Equations (SIMPLE) method. The second-order upwind scheme and the Quadratic Upstream Interpolation for Convective Kinematics (QUICK) scheme were chosen for spatial discretization of the momentum and phase fractions, respectively. The velocity boundary condition was defined for the flow of both phases at the pipe inlet, while the zero gauge pressure boundary condition was considered at the pipe outlet. The pipe wall was specified as no-slip boundary condition for the liquid phase and as free-slip boundary condition for the solid phase. The specularity and restitution coefficients values are 0.451 and 0.9, respectively.

A typical grid structure employed for the simulations is illustrated in Figure 2.1. This type of "butterfly" grid has shown good performance for simulating two-phase pipeline flows [82]. Moreover, the independency of computed results from the grid resolution was ascertained by examining different mesh refinements – see section 3.1 below. In the transient simulations, a constant time step of 0.001 s was specified and all the simulations were conducted for a period of over 10 s. The pipe length is fixed as 5.0 m, which is approximately $100\,D$ where D is the pipe diameter, so that the flow close to the pipe outlet can be fully developed. As far as the cross-sectionally averaged value is concerned for variables e.g. phase fraction, a spatial averaging process was carried out after each solution time step based on the area-

weighted averaging method. Such cross-sectionally averaged value from simulation results is commonly used to make comparison between the model predictions and the experimental data. A convergence in solutions was specified to reach when all tolerances fell below 10^{-4} for each time step. Another convergence criterion is that the monitored variable, i.e. the area-weighted average pressure at 4 m from the pipe inlet, reaches a stable level. The simulations were solved on the Compute Canada clusters, generally taking about 10 h for each simulation to be solved for 10,000 time steps on 32 CPUs, which is extremely more computationally efficient compared to other methods such as a direct numerical simulation (DNS) approach for the similar system [83] .

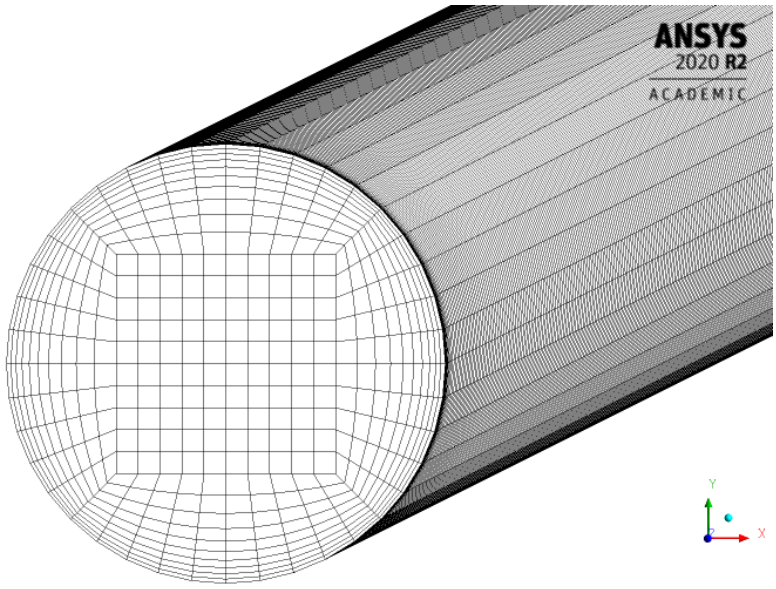

Figure 2.1: Grid structure in the computational domain of horizontal slurry pipeline.

2.2 Mixture model for tailings slurry

2.2.1 Mass and momentum conservation equations

Table 2.4: Mass and momentum equations for the mixture model employed in the present CFD simulation [43].

Continuity	$\frac{\partial}{\partial t}\left(\rho_m\right) + \nabla \cdot \left(\rho_m \vec{V}_m\right) = 0$	(2.8a)
	$\vec{V}_m = \frac{\sum_{k=1}^{n} \alpha_k \rho_k \vec{V}_k}{\rho_m}$	(2.8b)
Momentum	$\frac{\partial}{\partial t}\left(\rho_m \vec{V}_m\right) + \nabla \cdot \left(\rho_m \vec{V}_m \vec{V}_m\right) = -\nabla p + \nabla \cdot \left[\overline{\overline{\tau}}_s\right] + \rho_m \vec{g} + \vec{F} + \nabla \cdot \left(\sum_{k=1}^{n} \alpha_k \rho_k \vec{V}_{dr,k} \vec{V}_{dr,k}\right)$	(2.9a)
	$\overline{\overline{\tau}}_s = \mu_m \left(\nabla \vec{V}_m + \nabla \vec{V}_m^T\right)$	(2.9b)
	$\vec{V}_{dr,p} = \vec{V}_{pq} - \sum_{k=1}^{n} c_k \vec{V}_{qk}$	(2.9c)
	$\vec{V}_{pq} = \frac{\left(\rho_p - \rho_m\right) d_p^2}{18 \mu_q f_{drag}} \vec{a} - \frac{\eta_t}{\sigma_t}\left(\frac{\nabla a_p}{a_p} - \frac{\nabla a_q}{a_q}\right)$	(2.9d)
	$\frac{\partial}{\partial t}\left(\alpha_p \rho_p\right) + \nabla \cdot \left(\alpha_p \rho_p \vec{V}_m\right) = 0$	(2.9e)

In this section, the theory and equations of the mixture multiphase model are provided. The flow field of the mixture in the pipeline is predicated by solving the conservation of mass and momentum equations in three–dimensional Cartesian coordinates using mixture model [84] based on finite volume method. The continuity and momentum balance equations are written and solved only for the mixture phase,

with an algebraic expression for the slip velocity between the primary and secondary phases.

The equations for conservation of mass and momentum are given in Table 2.4. The continuity equation for the mixture is given as Eq. (2.8)a where $\vec{V}_m$ is the mass–averaged velocity expressed as Eq. (2.8)b, and ρ_m is the density of the mixture. In Eq. (2.8)b, α_k and ρ_k denote the volume fraction and density of k^{th} phase, respectively.

In the mixture model, the momentum balance equation is written by summing the individual momentum equations for all phases as Eq. (2.9)a. In this equation, n is the number of phases, $\vec{F}$ is a body force, and μ_m is the viscosity of the mixture ($\mu_m = \sum_{k=1}^{n} a_k \mu_k$). $\vec{V}_{dr,k}$ is the drift velocity for secondary phase k, and is defined as the relative velocity between k phase velocity and the velocity of center of mass. The slip velocity (V_{pq}) is defined as the velocity of a secondary phase (p) relative to the velocity of the primary phase (q), and is connected to the drift velocity as Eq. (2.9)c, where $c_k = \frac{\alpha_k \rho_k}{\rho_m}$. Manninen et al. [84] mixture model assumes a local equilibrium between the phases over a short spatial length scale, and uses an algebraic slip formulation. In a turbulent regime, the slip velocity can be expressed as Eq. (2.9)d. In this equation, τ_p is the particle relaxation time $\tau_p = \frac{\rho_p d_p^2}{18\mu_q}$, d is the diameter of the particles (or droplets or bubbles) of secondary phase $p, \vec{a}$ is the secondary phase particle's acceleration. σ_t is a Prandtl/Schmidt number set to 0.75 and η_t is the turbulent diffusivity.

The drag functions f_{drag} are taken from Gidaspow et al. [85] (fluid–solid) and symmetric (fluid–fluid) model between carrier and secondary phases. For the liquid–solid drag model (the drag model for the carrier fluid and solids), numerous studies in the

literature show that the model proposed by Gidaspow et al. [85] gives an accurate expression [86]. Nevertheless, as the number of studies for the three–phase simulation with two fluid phases is limited, no reliable analysis for the choice of drag model between the carrier and bitumen can be found in the literature. In this regard, the available drag models in Ansys Fluent were tested to find the most appropriate drag model in this case. The volume fraction equation for secondary phase p can be achieved from the continuity equations as shown in Eq. (2.9)e.

2.2.2 Kinetic theory of granular flow

The kinetic theory of granular flow was implemented to capture the effects of particle–particle interactions on the flow behavior. The equations of frequently used KTGF sub–models are given in Table 2.5 in detail. The effective viscosity for the mixture with respect to the the granular viscosity is obtained by constitutive equations (Eq. (2.10)a) derived by Syamlal et al. [66] and Gidaspow et al. [85]. The collisional (Eq. (2.10)b [85]) and kinetic (Eq. (2.10)c [66]) parts, and the optional frictional part (Eq. (2.10)d) are added to give the solids shear viscosity. In this way, the shear viscosity arising from particle momentum exchange due to translation and collision is taken into account.

The granular temperature is expressed as Eq. (2.10)e. Mixture model solves the algebraic equation from the granular temperature transport equation as described by Eq. (2.10)f where a balance of energy is written. The terms on the right–side of the equation represent the generation and the collisional dissipation of energy by the solid stress tensor, and the energy exchange between phases, respectively.

A general solids pressure formulation in the presence of more than one solid phases

Table 2.5: Equations of the kinetic theory of granular flow in the mixture model [43].

$$\mu_s = \mu_{s,\text{col}} + \mu_{s,\text{kin}} + \mu_{s,\text{fr}} \tag{2.10a}$$

$$\mu_{s,\text{col}} = \frac{4}{5}\alpha_s \rho_s d_p g_{0,\text{ss}} \left(1 + e_{ss}\right) \left(\frac{\Theta_s}{\pi}\right)^{1/2} \alpha_s \tag{2.10b}$$

$$\mu_{s,kin} = \frac{a_s d_s \rho_s \sqrt{\Theta_s \pi}}{6\left(3 - e_{ss}\right)} \left[1 + \frac{2}{5}\left(1 + e_{ss}\right)\left(3e_{ss} - 1\right)\alpha_s g_{0,ss}\right] \tag{2.10c}$$

$$\mu_{s,\text{fr}} = \frac{p_{\text{fr}} \sin\varphi}{2I_{2D}^{1/2}} \tag{2.10d}$$

$$\Theta_s = \frac{1}{3}\left\|\vec{v}_s'\right\|^2 \tag{2.10e}$$

$$0 = \left(-p_s \overline{\overline{I}} + \overline{\overline{\tau_s}}\right) : \nabla \vec{v_s} - \gamma_{\Theta_s} + \phi_{ls} \tag{2.10f}$$

$$\gamma_{\Theta_s} = \frac{12\left(1 - e_{ss}^2\right) g_{0,ss}}{d_p \pi^{1/2}} \rho_s \alpha_s^2 \Theta_s^{3/2} \tag{2.10g}$$

$$\phi_{ls} = -3K_{ls}\Theta_s \tag{2.10h}$$

$$p_q = \alpha_q \rho_q \Theta_q + \left(\sum_{p=1}^{N} \frac{d_{pq}^3}{d_q^3} p_{c,qp}\right) \rho_q \Theta_q \tag{2.10i}$$

$$g_{0,pq} = \frac{1}{\left(1 - \alpha_s\right)} + \frac{3\left(\sum_{k=1}^{N} \frac{\alpha_k}{d_k}\right)}{\left(1 - \alpha_s\right)^2 \left(d_p + d_q\right)} d_p d_q \tag{2.10j}$$

could be of the form of Eq. (2.10)i, where $d_{pq} = \frac{d_p + d_q}{2}$ is the average diameter, and $p_{c,qp}$ is the collisional part of the pressure between phases q and p. In Eq. (2.10)i, $p_{c,qp} = 2\left(1 + e_{pq}\right) g_{0,pq} \alpha_q \alpha_p$. When the number of solid phases is greater than 1, the radial distribution function between the p^{th} and q^{th} solid phases is expressed by Syamlal et al. [66] as in Eq. (2.10)j.

2.2.3 Turbulence model

In our previous study [86] for the Eulerian–Eulerian model, the suitability and performance of the Two–Equation turbulence models ($k-\epsilon$ and $k-\omega$) for the multiphase slurry flows was highlighted. Especially, based on the previous works in the literature and the theory of the turbulence models, the acceptable and accurate prediction of the turbulent regieme in a multiphase flow using the $k-\omega$ model proposed by Menter [73] was emphasized. In the present study, at first both $k-\epsilon$ and $k-\omega$ models were examined, and the SST $k-\omega$ showed a better numerical stability leading to faster convergence, and excellent agreements between the CFD predictions and field data.

2.2.4 Rheological model for the carrier fluid

Adeyinka et al. [87] studied the effect of particle size on the rheology of Athabasca oil sand slurries, and presented a comprehensive rheological study on the mixture of fine particles harvested from Mature Fine Tailing (MFT) and water which leads to formation of a non–Newtonian fluid highly similar to the carrier fluid of this study. They performed the rheological measurements using three samples of fine particles with different size distributions and various mixtures of them. Fraction 1 of their study has the closest size distribution to the fine particles in this study. Therefore, the Casson non–Newtonian rheological model considered in this study through user–defined function (UDF), which is a specific as carrier fluid viscosity:

$$\tau^{1/2} = \tau_{\mathrm{y}}^{1/2} + \mu_{\mathrm{c}}^{1/2}\dot{\gamma}^{1/2} \tag{2.11}$$

In Equation 2.11, τ is shear stress, τ_y represents yield stress, and μ_c is Casson viscosity [87]. In case there is a gradual transition from Newtonian behavior to yield region,

the Casson rheological model is appropriate to describe the carrier fluid viscosity [88]. The rheological behavior of tailings slurries has been successfully modeled using Casson rheological model by other researchers [89–91].

2.2.5 Numerical methodology

Finite Volume Method (FVM) based commercial CFD software Fluent 2020R2 was used in this study and to solve the governing equations mentioned above. The velocity and volume fractions were specified at the inlet for all phases. At the wall, no–slip boundary condition was chosen which applies to the mixture, and for the outlet zero gauge pressure was imposed. Computational model settings are summarized in the Table 2.6. The pressure relaxation factor and momentum relaxation factor were set as 0.3 and 0.7. The volume fraction was set as 0.4, and the default values of other factors were used. Root mean square residuals were used, and the residuals for convergence were set as 10^{-4} and a fixed time step 0.01 s utilized in this study. One of the main question for this study was whether a solid bed is formed at the pipe invert or not, and the transient scheme can help to determine that. Note that in the steady–state simulation, there is no accumulation in the domain so the possibility of bed formation is neglected in the steady–state scheme.

The flow conditions of the simulated cases such as the mixture velocity, solids fraction, carrier density and bitumen fraction can be seen in Table 2.7. These cases will be used for validation in section 4.4, and Case 2 will be used as the base case for grid–independence check and further investigations.

Table 2.6: List of different models and schemes used in multiphase mixture model for modeling three–phase (liquid–solid–liquid) slurry flow.

Model	Scheme
Multiphase model	Mixture
Viscous model	k–ω SST model
Volume Fraction Parameters	Implicit Scheme
Pressure–velocity coupling	Phase Coupled SIMPLE Scheme
Spatial discretization–Gradient	Least Squares Cell Based
Spatial discretization–Pressure	PRESTO
Spatial discretization–Momentum	First Order Upwind
Spatial discretization–Volume Fraction	First Order Upwind
Spatial discretization–Turbulent Kinetic Energy	First Order Upwind
Spatial discretization–Specific Dissipation Rate	First Order Upwind
Transient Formulation	First Order Implicit
Granular viscosity	Syamlal and O'Brien [92]
Solid pressure	Lun et al. [93]
Granular temperature	Algebraic
Frictional Pressure (pascal)	Based–KTGF
Radial distribution	Syamlal and O'Brien [92]
Drag model: Liquid–solid	Gidaspow et al. [85]
Drag model: Liquid–Liquid	Symmetric [43]
Slip velocity	Manninen et al. [84]
Restitution coefficient	0.9

Table 2.7: Flow conditions of the simulated cases via mixture model for the industrial pipeline.

Case	α_v	$\rho_{carrier}\,(kg/m^3)$	$v_m\,(\mathrm{m/s})$	Bitumen volume fraction
(1)	0.238	1335	5.62	0.0025
(2)	0.23	1278	5.35	0.0033
(3)	0.237	1328	5.43	0.0029
(4)	0.269	1227	5.54	0.003
(5)	0.26	1221	5.20	0.0037
(6)	0.264	1196	5.21	0.0032
(7)	0.223	1222	5.76	0.003
(8)	0.222	1220	5.18	0.0028
(9)	0.273	1254	5.30	0.0044
(10)	0.238	1332	5.64	0.003

2.2.6 Collection of field data

Figure 2.2 a shows the schematic of the pipeline where the measurements have been performed to collect field data that are used for model validation. This pipeline is a section of a mining operation. The pipe is 74 cm in diameter, and located horizontally with 2 pumps and measurement devices in–line. The section used to measure the flow conditions for this study is around 220 m in length. The solid composition samples are collected after the first pump discharge for every 12 hours and and the compositions of the mixture are determined using a Dean–Stark apparatus [94]. The mixture velocities are measured approximately 20 m distance from the the second pump suction. A sieving method is used to calculate the particles size distribution

for the solid particles. The pressures were measured at the discharge of the first pump and suction of the second pump using two gauge pressure meter devices. To calculate the pressure gradient, the average values of pressure at the first pump discharge and second pump suction are considered.

For the velocity measurements, a velocity profiler is used. Figure 2.2b shows the schematic view of the measurement locations, from VF1 at the top to VF5 at the bottom of the pipe. The velocities are measured using a SANDtrac Velocity Profile System (CiDRA) based on a non–invasive technique. This device is an array of five sensors attached to the pipe wall, which track the turbulent eddies inducing pressure disturbance and consequently forces on the wall. This array senses the dynamic strains applied to the pipe by these forces and converts them to electrical signals to be interpreted, and the velocity values are calculated [95]. This technique is well–established and applied commercially for slurry transport in the industry, where detection of the formation of stationary beds is a usage of the device [96, 97]. The distance where the velocities are measured from the pipe center is around 0.85R which R is the pipe radius. Measurements of velocity and flow rate are taken every two seconds, yielding multiple values for a given period with some fluctuations.

Figure 2.2 c shows a schematic representation of the tailings flow with polydisperse solid particles and bitumen droplets in the pipeline. The data of compositions (mass fractions of different components of the flow) and PSD are collected every 12 hours. For the simulation purposes, multiple time windows of 30 minutes which contain 900 time steps in the measurements are selected, and the flow conditions have been averaged over the whole or a portion of these time windows. In the data sets collected, some fluctuations in terms of flow conditions are observed, which is reasonable con-

sidering the highly turbulent flow inside an industrial–scale pipeline. To remove the effect of these fluctuations, averaging is needed. This procedure is explained in detail in section 4.2.

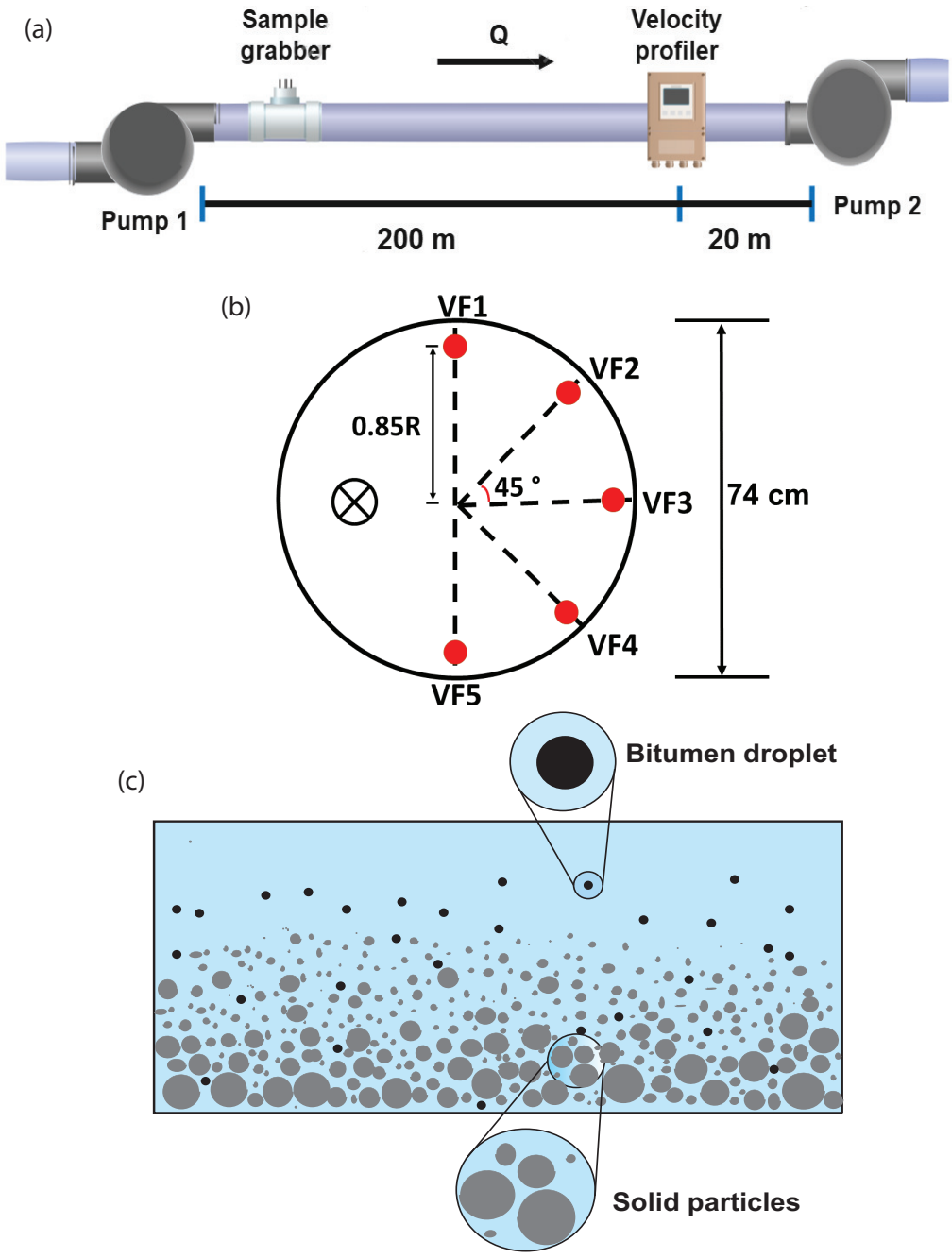

Figure 2.2: Schematics of (a) the tailings hydrotransport pipeline, (b) the velocity profiler with the tangential and radial locations of the measurement points (The flow direction is into the plane and has been marked), and (c) sketch of a tailings slurry flow in a horizontal pipeline .

Chapter 3

CFD simulation of turbulent non-Newtonian slurry flows in horizontal pipelines[1]

This chapter presents the results of the model system simulated with the Eulerian–Eulerian model. The details of the modeling approach are mentioned in Chapter 2.

3.1 Grid independence analysis

To ensure that the simulation results are independent of grid resolution, we compare the CFD simulations using the coarse, fine and finer grid structures shown in Figure 4.5. Specifically, we test the performances of the above three grids in simulating a representative case, i.e. the one presented in Figure 17 of Pullum et al. [2] – see Table 3.1. Representative results of solids concentration, area-averaged gauge pressure, solid-phase velocity, and liquid-phase velocity are illustrated in Figure 3.2.

[1] M. Sadeghi, S. Li, E. Zheng, S. G. Sontti, P. Esmaeili, X. Zhang. "CFD Simulation of Turbulent non-Newtonian Slurry Flows in Horizontal Pipelines". *Industrial and Engineering Chemistry Research*, vol. 61, num. 15, p. 5324-5339

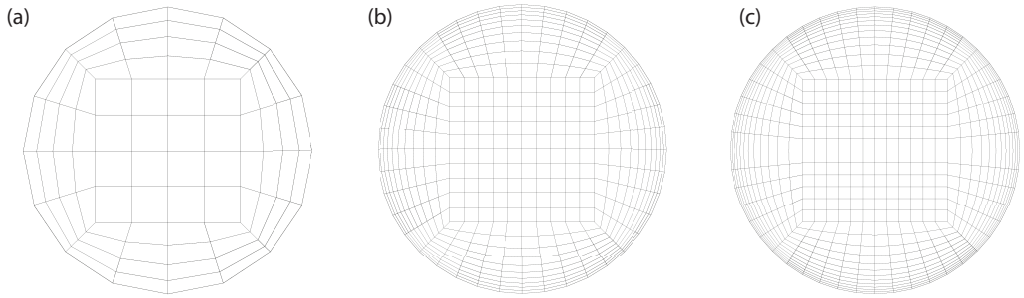

Figure 3.1: Cross-sectional view of (a) coarse, (b) fine and (c) finer grids. From panel a to c, the number of cells in the 3D grids are 46,960, 295,000 and 499,395, respectively.

Overall, excellent agreement between the fine and finer grids is observed, whereas the coarse grid predictions show some deviations. Other researchers have widely used this approach for grid-independency check for the simulation of multiphase flows in pipelines.[19, 36, 59] The values for wall y^+ were constantly monitored for the "fine" grid used for the simulations. The maximum y^+ for the solid phase was 0.033 and for the carrier phase 3.74, which clearly shows that the grid is fine enough near the wall.

To maintain good accuracy and moderate computational cost simultaneously, all the simulations are performed using the fine grid as shown in Figure 4.5 b. For better visualization of the solids concentration and carrier velocity distributions, the contours of solids concentration and carrier velocity at successive axial distances, i.e. 0, 1, 2,3, 4 and 5 m downstream of the pipe inlet, are shown in Figure 3.3. The contours at 4 m and 5 m are almost identical, which indicates a fully developed flow condition near the pipe outlet.

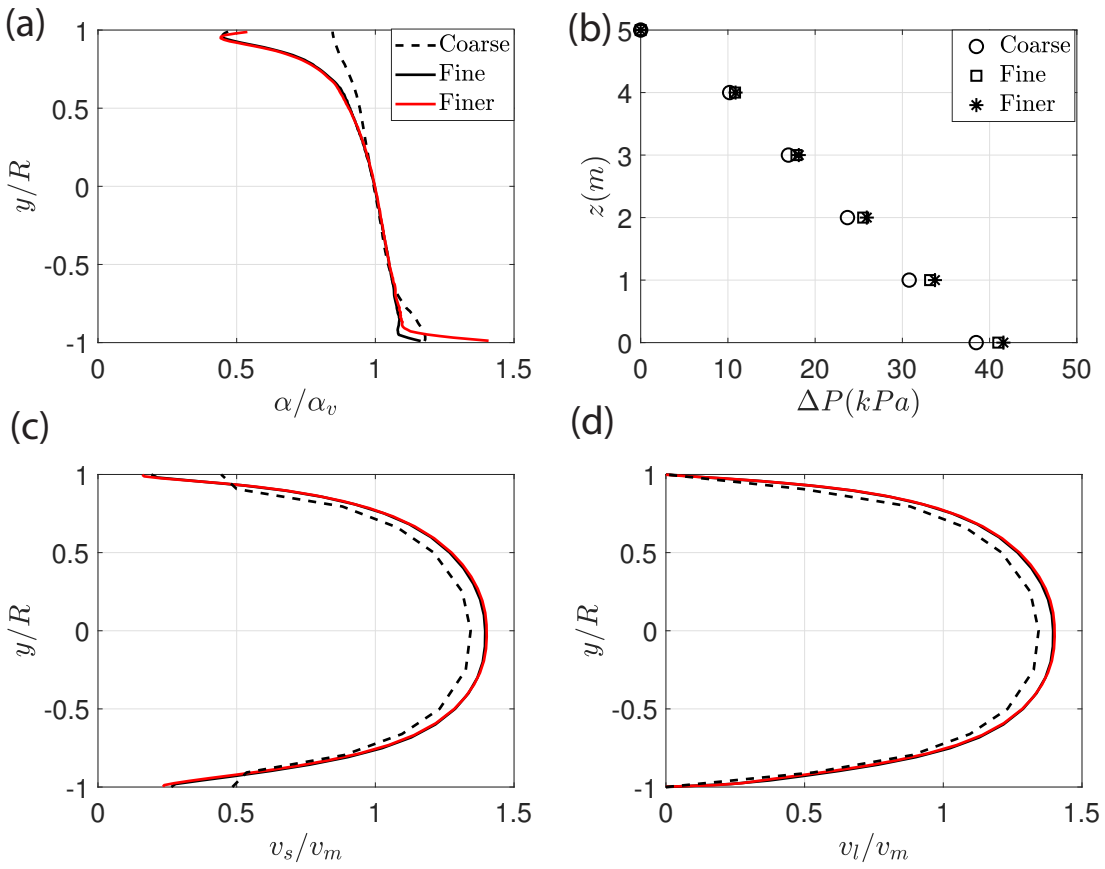

Figure 3.2: [Color] (a) Solids concentration profile. (b) Area-averaged gauge pressure (ΔP) vs. the axial distance (z) from the pipe inlet. (c) Solid-phase velocity vs. y/R where y is the vertical axis and R is the pipe radius. (d) Liquid-phase velocity profile.

3.2 Model validation

The experimental data found in literature for monodisperse particles are summarized in Table 3.1. Experimental data using bimodal particles are referred to the experimental tests 21 and 22 of Kesely [1] – see Table 3.2. Measured parameters mainly include chord-averaged solids concentration and frictional pressure drop. For the purposes of model validation, the geometrical and operating conditions in CFD

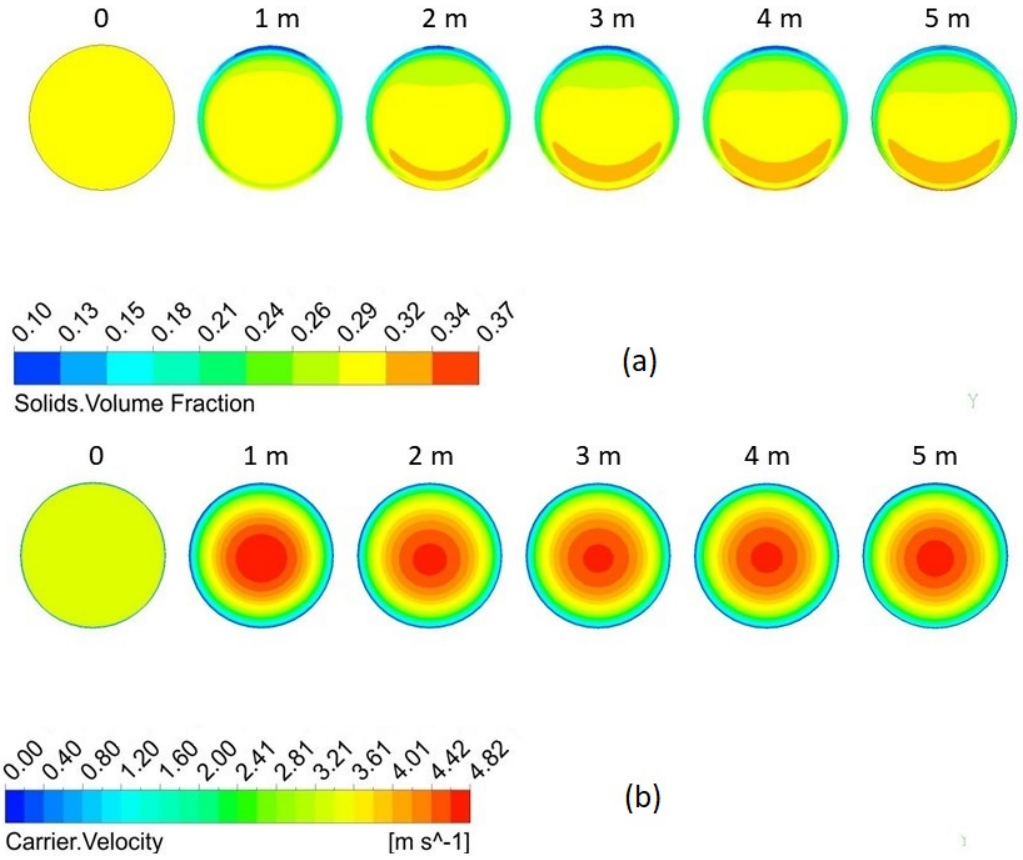

Figure 3.3: [Color] Contours of (a) solids concentration, and (b) carrier velocity at 0, 1, 2, 3, 4 and 5 m downstream of the pipe inlet.

Table 3.1: Experimental conditions for monodisperse particles.

Data source	Pipe diameter, D (mm)	Particle diameter, d_p (mm)	Solids concentration, α_v (%)	Particle density, ρ_s (kg/m^3)	Liquid density, ρ_l (kg/m^3)	Mixture velocity, v_m (m/s)	Herschel-Bulkley model		
							τ_y (Pa)	K (Pa s^n)	n
Pěník et al. [25]	51.4	1.5	20	2488	1000	3.51-4.45	1.872	2.365	0.476
Matoušek & Pěník (Figure 17 of [2])	50.0	1.5	30	2450	1000	3.3-3.4	1.4	2.3	0.5
Pěník (2015, Figure 18 a of [2])	44.0	0.18	10	2550	1000	2.2-3.8	0.9	0.29	0.6
Test 2 of [1]	50.0	0.64	15	2423	1000	2.6-4.5	1.88	1.36	0.52
Zheng et al. [7]	44.0	2	10-18	2600	1000	2.59-3.67	0.01-0.16	0.124-0.406	0.59-0.7

and experiment are maintained identical.

3.2.1 Chord-averaged solids concentration

Overall agreement between CFD and experiment is observed in Figure 3.4. The validation of the model with chord-averaged solids concentration has been performed only for monodisperse (single-sized) particles. The experimental data presented in Figure 3.4a to 3.4d is based on the experiments conducted by Pěník et al. [25]. The solids concentration data from the simulations were exported from the pipe outlet, which is 5 m in length. Overall, the comparison between CFD results and experimental data for these four figures shows very good agreement, especially for the core region i.e. $-0.75 \leq y/R \leq 0.75$. It must be noted that solid concentration distribution in the radial direction in Pěník et al. [25] paper has been measured by ERT, which is limited by low spatial resolution and the ill-posedness of the inverse problem in the image reconstruction. According to Pěník et al. [25], due to their approach for image reconstruction, there was an overestimation of solid concentration at the top and underestimation at the bottom of the pipe, particularly with the presence of a bed. Keeping this issue in mind, it can be foreseen that the agreement at the boundary would be more satisfactory with more accurate data collection. Fig 3.4e-h show the comparison between CFD-predicted solid concentration distribution and experimental data measured by Zheng et al. [7]. Excellent agreement is observed for most data points across the y-axis, except for regions near the wall, which is due to the limitations in the RANS turbulence modeling and Euerian-Eulerian model. Altogether, the results of the CFD simulations with the current model have been validated for a wide variety of experimental conditions from different sources, with

an exceptional agreement for most of the data. However, there are some limitations in the model that contribute to the relatively poor agreement near the pipe invert as mentioned.

In Figure 3.4e-h, the experimental results reveal that the solid particles are more suspended than predicted by CFD, which indicates that the particle-particle/wall interactions are not well captured by the Eulerian-Eulerian model. Generally, the Eulerian-Eulerian model assumes that both phases share the same turbulence field, but it should be considered that particle fluctuations do not vanish at the wall due to particle rotational and sliding motions. The particle-particle/wall collision and gravity also affect the particle motion in the wall-normal direction, which leads to a turbulence augmentation that can not be captured by a RANS turbulence model used in the Eulerian-Eulerian model [98]. The difference may also arise from the treatment of the solids stress term in the Eulerian-Eulerian model, which is based on empirical constitutive correlations and inter-particle (or particle-wall) collisions may not be captured well.

3.2.2 Frictional pressure drop

The frictional pressure drop is expressed in terms of hydraulic gradient, which is defined as $i = \frac{\Delta P_{4\mathrm{m}}}{\rho_w \times g \times (1\,\mathrm{m})}$ where $\Delta P_{4\mathrm{m}}$ is the area-averaged gauge pressure at 4 m from the pipe inlet (or 1 m upstream of the pipe outlet), ρ_w is the density of pure water and g is gravitational acceleration. The comparison between the CFD-predicted and experimentally measured pressure gradient for different flow conditions is presented in Figure 3.5. Overall, this comparison indicated that the model is able to predict

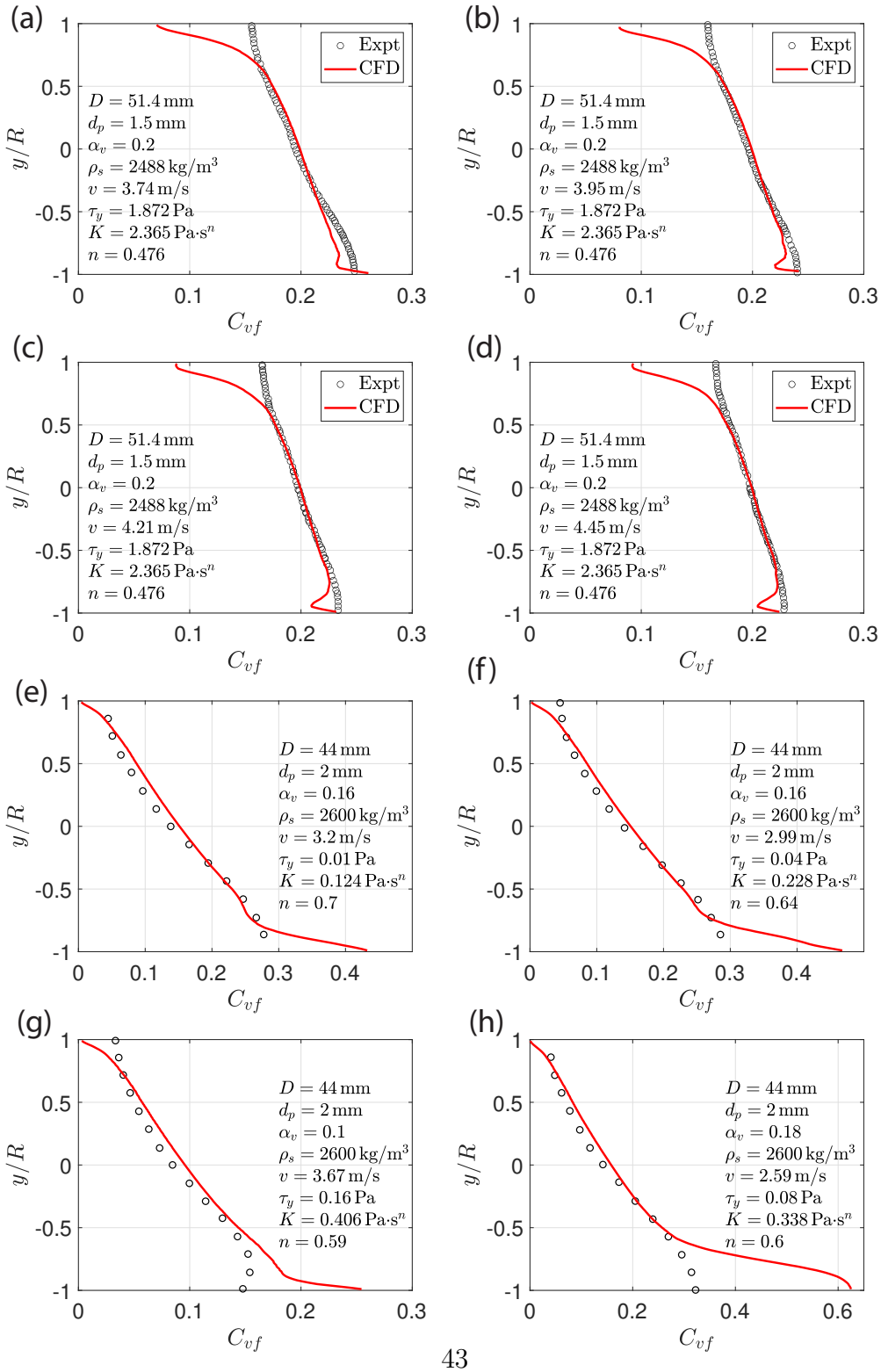

Figure 3.4: Chord-averaged solids concentration of CFD (solid curve) vs. experiment (circles). Panels a, b, c and d refer to [25] and panels e, f, g , and h refer to [7]–see Table 3.1.

Table 3.2: Experimental conditions for bimodal particles [1].

Test	21	22
d_{s1} (mm)	0.64	
d_{s2} (mm)	1.55	
ρ_{s1} (kg/m^3)	2423	
ρ_{s2} (kg/m^3)	2448	
α_{s1}	0.0644	0.0841
α_{s2}	0.0851	0.1073
τ_y (Pa)	2.41	1.15
K (Pa s^n)	2.13	1.56
n	0.5	0.51

the pressure gradient in the pipeline with good accuracy, considering that the error margin is 15%, and all of the data points fall below this margin. For the monodisperse case, better agreement is observed when the particle size is relatively small e.g. $d_p < 1\,\text{mm}$ or the area-averaged solids concentration is relatively low e.g. $\alpha_v \leq 0.1$. For large d_p and/or α_v, the granular kinetic theory may overestimate particle-particle interactions in non-Newtonian fluid thus leading to higher pressure drop. In the case of bimodal particles, the drag force between two solid phases has a minimal impact on the predicted pressure drop when CFD predictions are compared without drag force between the particles. This is not surprising due to the relatively dilute particles. The presented results for the bimodal particles are with consideration of the drag force between solids.

In summary, the model was in good agreement with a wide variety of experimental

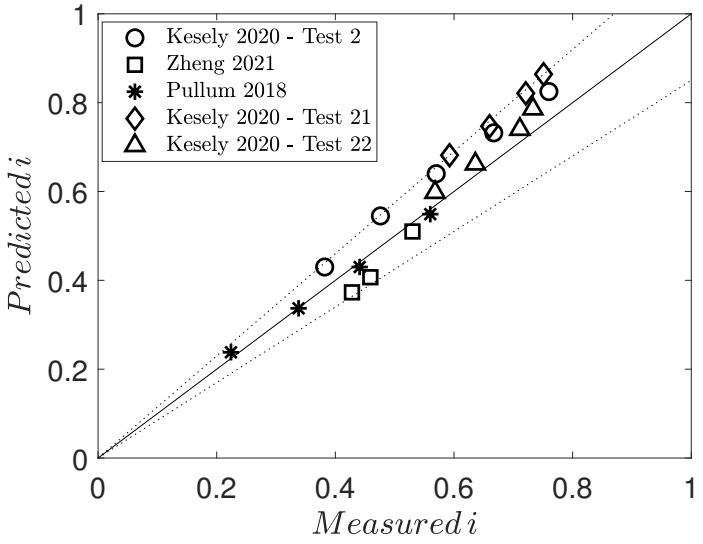

Figure 3.5: Parity plot of frictional pressure drop obtained from CFD vs. experiment for monodisperse and bimodal particles. The solid line is the bisector and the two dashed lines denote errors of ±15%.

data found in the literature for the chord-averaged solids concentration and pressure gradient. It was proven that the model shows a good performance in the prediction of the flow behavior of two-phase slurry flows, hence it can be utilized for a parametric study to further understand the effect of flow parameters and slurry characteristics – see section 3.3.

For accurate modeling of the dense slurry systems, our work shows the drag force is vital and has to be included in the model. Virtual mass force and turbulence dispersion are also important in our model. Other forces such as the lift force due to shear and the force due to the rotation of the reference frame that are considered in the Eulerian-Lagrangian model are not included in the Eulerian-Eulerian method.[43]

In the simulation of slurry flows in the literature, both no-slip[5, 83] and free-

slip[20, 99] boundary conditions have been extensively used. In our case, we compared free-slip and no-slip boundary conditions for the cases simulated for the validation purpose, and also systematically explored the possibility of using partial-slip. However, our results showed that the free-slip boundary condition gives the excellent agreement with a minimum overall error for the cases with the most discrepancy at the pipe invert.

3.3 Parametric study

In this section, we investigate the effects of particle diameter (d_p), area-averaged solids concentration (α_v), mixture velocity (v_m), and carrier fluid density (ρ_l) on the solid-phase velocity, frictional pressure drop and solids concentration distribution. The aim of this parametric study based on the mentioned flow condition was to determine the effect of each parameter on the efficiency of the hydrotransport process by comparing the suspension of the particles and the area-averaged pressure gradient. The parametric study has been performed only for the monodisperse particles. The results can help to design and optimize the process in a way that the most possible capacity of the pipeline is used to transport slurries with the minimum pressure loss. The chosen parameters are easy to manage by the operator, with the carrier fluid density manageable by the amount of fine particles in the flow, and as the results show, are of great importance in this process. It is worth noting that the present study mainly focused on the flow conditions and parameters mentioned above. Further investigations also can be extended based on the effect of different rheological models and set of parameters such as yield stress and fluid consistency coefficient with proper validation of the CFD model.

The baseline case to consider is the one shown in Figure 17 of Pullum et al. [2] with the following operating conditions:

$$D = 50.0\,\text{mm}, d_p = 1.5\,\text{mm}, \alpha_v = 0.3, \rho_s = 2450\,\text{kg/m}^3, \rho_l = 1000\,\text{kg/m}^3,$$

$$v_m = 3.35\,\text{m/s}, \tau_y = 1.4Pa, K = 2.3\,\text{Pa.s}^\text{n}, n = 0.5.$$

The flow conditions for this case are close to the cases used for the validation but with a higher solids concentration which is favourable for this process.

3.3.1 Effects of particle diameter

After demonstrating an excellent and acceptable agreement of simulation with a different set of experimental results, this study analyses the flow behavior at different conditions. In this section, results focus on coarse particles in the range of 0.5 to 2 mm, which can settle in the pipeline based on flow conditions. Figure 3.6 a shows asymmetric solid-phase velocity profiles for all the particle sizes considered. Notably, the degree of asymmetry increases with increasing particle diameter due to gravitational effects. Similar asymmetric solid-phase velocity profiles have been reported by Eesa and Barigou [20] for the laminar flow case. The maximum solid-phase velocity, which occurs near the pipe center is between v_m and $1.5v_m$ in magnitude. Figure 3.6 b shows that pressure drop increases with increasing particle diameter, although smaller rates of increase are observed for larger particles. For larger particles, particle settling is more frequent and more particles accumulate near the pipe invert (Figure 3.6 d), thus enhancing particle-wall interactions and the associated pressure drop. On the other hand, the increase in pressure drop with particle diameter is approximately 30% and less significant than expected, which is probably due to the

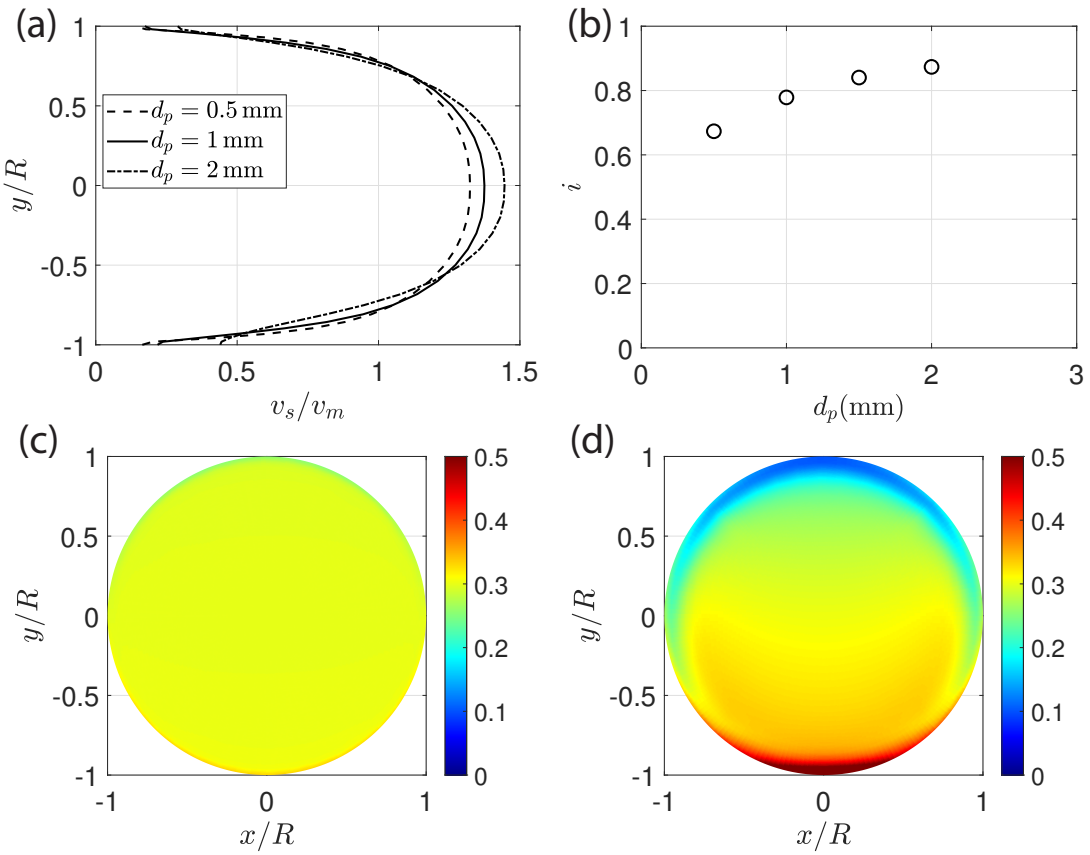

Figure 3.6: Effects of particle diameter on (a) nondimensional solid-phase velocity, and (b) pressure drop . Contours of solids concentration at the pipe outlet for (c) $d_p = 0.5\,\mathrm{mm}$, and (d) $2\,\mathrm{mm}$. ($D = 50.0\,\mathrm{mm}, \alpha_v = 0.3, \rho_s = 2450\,\mathrm{kg/m^3}, \rho_l = 1000\,\mathrm{kg/m^3}, v_m = 3.35\,\mathrm{m/s}, \tau_y = 1.4\,\mathrm{Pa}, K = 2.3\,\mathrm{Pa.s^n}, n = 0.5$)

reduction in surface area anticipated for larger particles while the solids volume fraction is fixed. For relatively small particles e.g. $d_p = 0.5\,\mathrm{mm}$, Figure 3.6 c shows that the solids concentration is approximately uniform except for the near wall region. By contrast, more stratification in solids concentration is seen for larger particles e.g. $d_p = 2\,\mathrm{mm}$ – see Figure 3.6 d. Both particles settling and frictional pressure drop showed to be intensified by increasing the particles size, which is unfavourable

for the hydrotransport process. Generally, larger particles are more likely to settle due to gravitational forces and form a bed at the bottom of the pipe. However, this stratification can significantly affect scale-up, which needs to be taken into account in predicting the pressure drop.

3.3.2 Effects of area-averaged solids concentration

The area-averaged solids concentration ranges from 0.1 to 0.4. Figure 3.7 a shows that the overall effect of area-averaged solids concentration on the solid-phase velocity profile is small. Figure 3.7 b shows that, as expected, pressure drop increases monotonically with increasing α_v. As α_v increases, the total surface area of particles increases; particle-particle collisions become more frequent; same as particle-wall collisions. This indicates that the particle-liquid, particle-particle, and particle-wall interactions are all enhanced, thus leading to a steady increase in pressure drop. However, the pressure gradient should not be considered solely in this process. The key parameter here is the amount of energy required for the transport of slurries over various conditions. Specific energy consumption (SEC) which was defined by Wilson et al. [24] is a proper criterion to determine whether going to higher concentrations is more economically favourable:

$$SEC = \frac{i_{\mathrm{m}}}{S_{\mathrm{s}} C_{\mathrm{v}}} \tag{3.1}$$

where i_m is the hydraulic gradient, C_v is the delivered solids volume fraction , and S_s is the specific gravity of the particles which is 2.65 for all cases. The solids concentration in the delivered mixture was calculated based on the definition proposed by Gillies [100]. For the considered range of solid concentrations, the specific

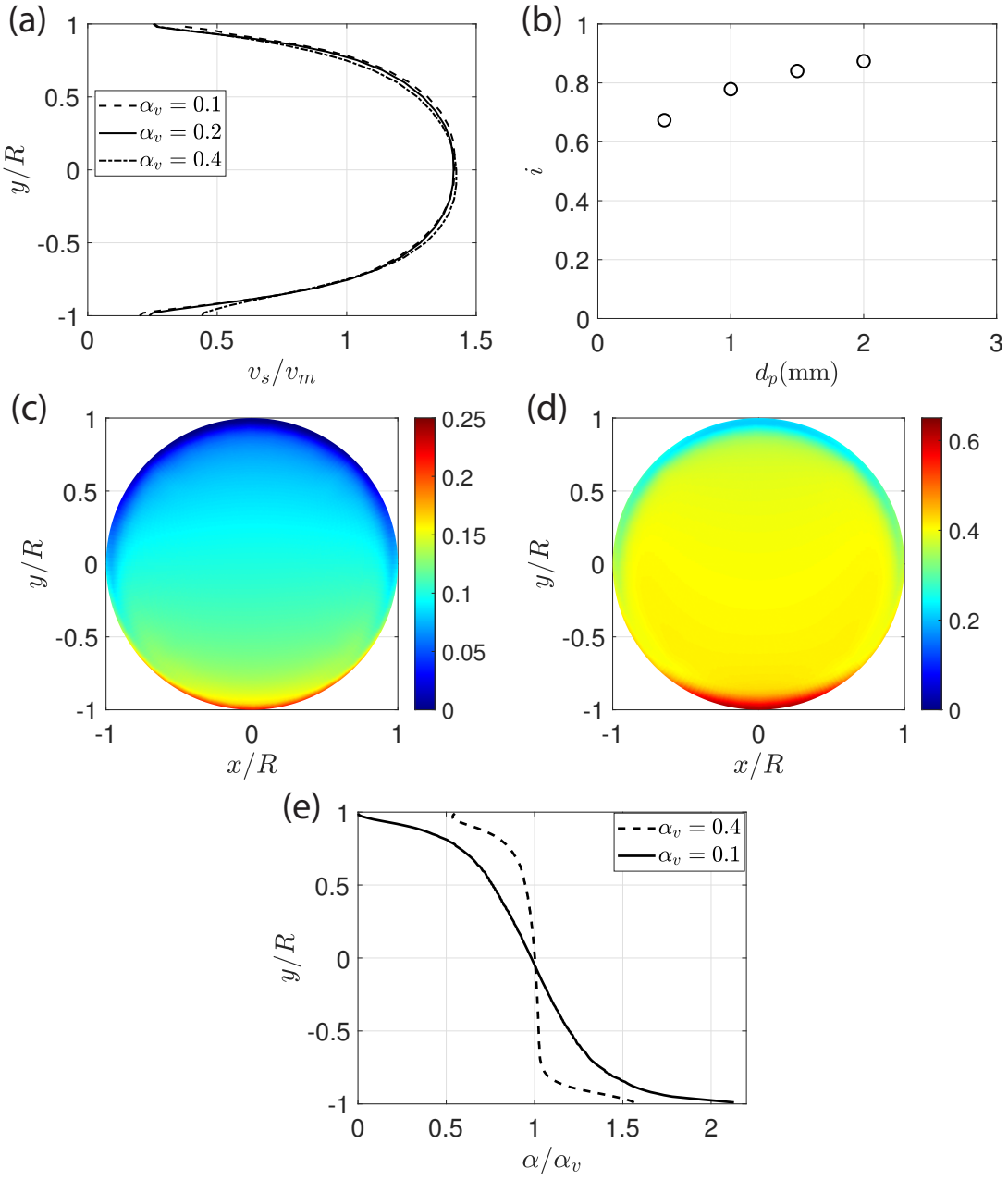

Figure 3.7: Effects of area-averaged solids concentration on (a) nondimensional solid-phase velocity, and (b) pressure drop. Contours of solids concentration at the pipe outlet for (c) $\alpha_v = 0.1$, and (d) 0.4. (e) Normalized chord-averaged solids concentration. Note the difference in the colorbar limits of panels c and d. (D = 50.0 mm, d_p = 1.5 mm, $\rho_s = 2450\,kg/m^3$, $\rho_l = 1000\,kg/m^3$, v_m=3.35 m/s, τ_y = 1.4 Pa, K = $2.3\,Pa.s^n$, n = 0.5)

energy consumption is 7.31 kWh/tonne-km for the lowest concentration and 2.32 kWh/tonne-km for the case with the highest solids concentration. It can be concluded that although the highest considered solids concentration leads to the highest pressure gradient, it also has the lowest specific energy consumption, meaning that considering the delivered concentration, the corresponding energy consumption is minimum for higher concentrations. It should be noted that other parameters can also affect SEC, and the optimum concentration is not always the highest possible concentration [101].

Figures 3.7 c and d show the contours of solids concentration distribution for the cases with $\alpha_v = 0.1$ and 0.4, respectively. For smaller α_v, the normalized solids concentration distribution shown in Figure 3.7 e is more asymmetric, with an increase near the bottom, which shows a portion of the particles tend to accumulate at the bottom. In contrast, for the $\alpha_v = 0.4$ case shown in Figure 3.7 e, the degree of asymmetry is lower compared to the previous case. This finding is in agreement with the results achieved by Zhang et al. [23], they argued that with a higher concentration, the random collisions between particles become more frequent, which promote the particles interactions and result in more suspension of particles. Shown also in Figure 3.7 d is that the solids distribution is relatively uniform except for the near wall region. For α_v that is large enough so that the maximum packing limit ($\alpha_{s,\max}$ in (2.4) b) is approached, there is no extra space near the pipe invert for particle settling and thereby more particle suspensions are allowed [20]. Meanwhile, the hindered settling velocity decreases with increasing α_v in case of relatively larger particles [24], which also contributes to the uniform solids concentration distribution.

3.3.3 Effects of mixture velocity

The mixture velocity ranges from 3 m/s to 6 m/s in order to examine the flow behavior over a range of velocities below and over the baseline case while assuring the flow is in the turbulent regime. Figure 3.8 a shows that the maximum nondimensional solid-phase velocity decreases marginally when the mixture velocity increases. When the mixture velocity is low e.g. $v_m = 3\,\mathrm{m/s}$, more particles accumulate at the pipe invert (Figure 3.8 c), which reduces the effective flow area and as a result the fluid velocity in the upper region increases. In turn, the solid-phase velocity (nondimensionalized by v_m) in the core region tends to increase as v_m decreases.

The pressure drop shown in Figure 3.8 b increases monotonically with increasing mixture velocity. This profile is consistent with the trend of tailings transport characteristics curve shown in e.g. Figure 5 of Pullum et al. [2] and experimentally measured pressure drop profiles shown in e.g. Figure 2 of Pěník et al. [25] in the turbulent regime. Figure 3.8 d shows concentration depletion near the pipe invert for relatively large mixture velocity of $v_m = 6\,\mathrm{m/s}$. When the mixture velocity is high, high turbulent mixing is anticipated thus resulting in more particle suspensions [2]. Shown in Figure 3.8 e is a bimodal distribution of TKE with two peaks located near the wall. For the lower mixture velocity,the TKE profile is approximately symmetric, whereas this profile is asymmetric for larger mixture velocity. The higher peak in the boundary regions of the pipe (solid curve of Figure 3.8 e) corresponds to regions of more turbulence, where solid particles are dilute. It is also noticeable that a local minimum in the TKE occurs near the pipe center for the case with a higher mixture velocity, where the solids concentration is maximum. This plot accords with the

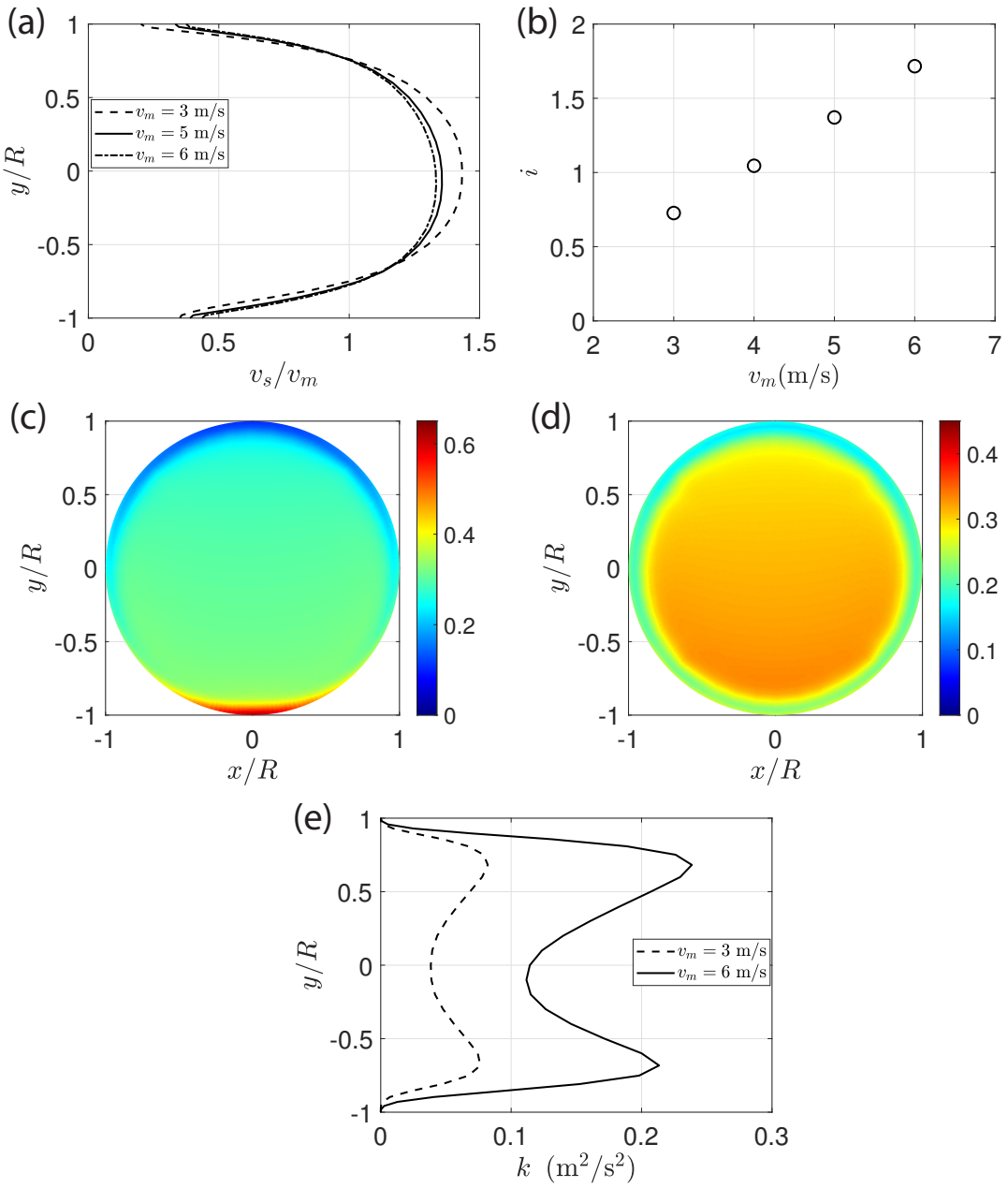

Figure 3.8: Effects of mixture velocity on (a) nondimensional solid-phase velocity, and (b) pressure drop. Contours of solids concentration at the pipe outlet for (c) $v_m = 3\,\mathrm{m/s}$, and (d) $6\,\mathrm{m/s}$. (e) Plots of turbulence kinetic energy for $v_m = 3\,\mathrm{m/s}$ and $6\,\mathrm{m/s}$. ($D = 50.0\,\mathrm{mm}, d_p = 1.5\,\mathrm{mm}, \alpha_v = 0.3, \rho_s = 2450\,\mathrm{kg/m^3}, \rho_l = 1000\,\mathrm{kg/m^3}, \tau_y = 1.4\,\mathrm{Pa}, K = 2.3\,\mathrm{Pa.s^n}, n = 0.5$)

contours of solids concentrations, indicating that for higher mixture velocity, there is a reversal in concentration at the pipe invert, and maximum concentration occurs at the core region of the pipe. Although particles suspension is promoted with higher velocities, by considering SEC (For instance, 2.49 and 5.89 kWh/tonne-km for mixture velocity (v_m) of 3 m/s and 6 m/s, respectively) it is revealed that operating with higher velocities is less efficient. As shown, the pressure drop will significantly increase by increasing velocity while the concentration is the same, leading to a larger value of SEC. Wilson et al. [24] present a comprehensive discussion on SEC and effective parameters, with experimental evidence showing that an increased velocity results in higher specific energy consumption.

3.3.4 Effects of carrier fluid density

In this section, the effects of carrier fluid density on the flow conditions have been analyzed. For the slurry transport processes, the non-Newtonian carrier fluid is a mixture of water and fine particles, and its density can be close to water density at minimum and can be as high as $1400\,\mathrm{kg/m^3}$ in some processes [102]. In this section, the carrier fluid density ranges from $\rho_l = 1000\,\mathrm{kg/m^3}$ to $1400\,\mathrm{kg/m^3}$. Overall, as indicated in Figure 3.9, the effects of carrier fluid density are shown to be less significant compared to other parameters mentioned before, especially on pressure gradient and particles velocity. Figure 3.9 a shows that increasing the carrier fluid density, the solid-phase velocity results in more symmetry in the solid-phase velocity plot. When the carrier fluid density decreases, the larger difference between the fluid and solids density leads to more accumulation of solid particles at the pipe invert, which can be concluded from Figures 3.9 c and d. This accumulation of solid

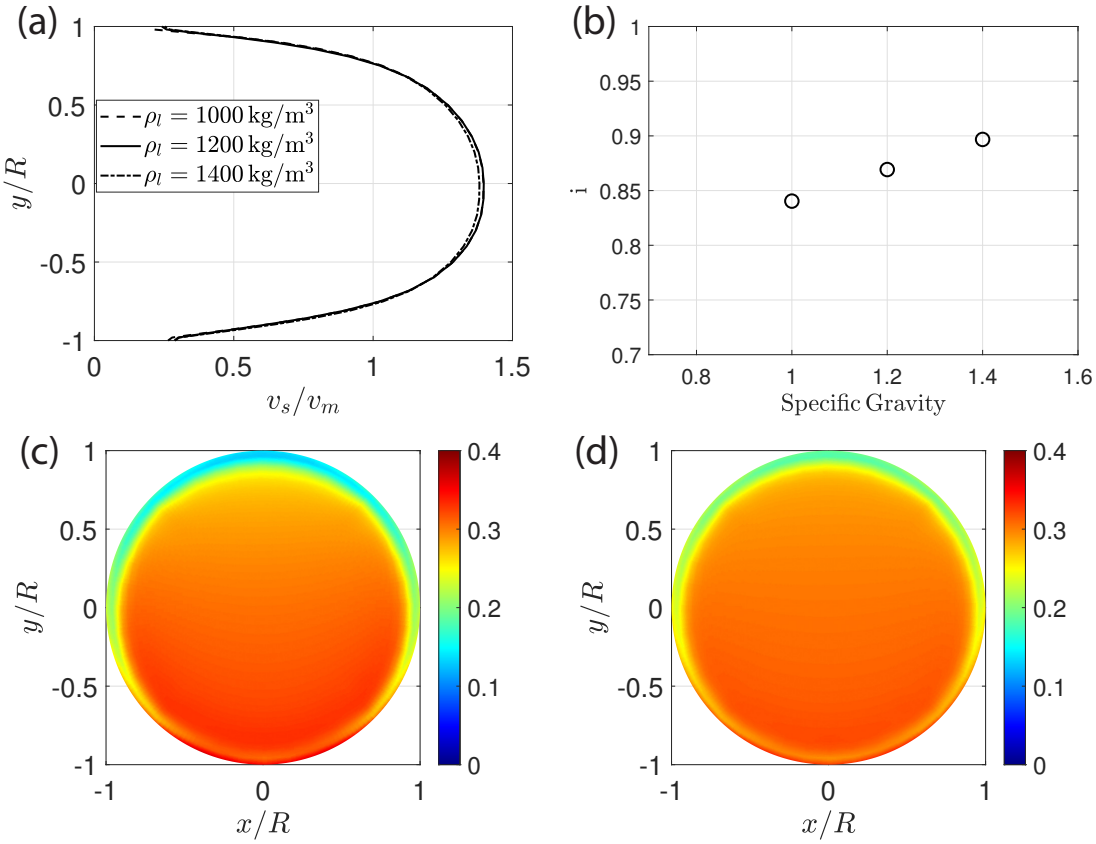

Figure 3.9: Effects of carrier fluid density on (a) nondimensional solid-phase velocity, and (b) pressure drop. Contours of solids concentration at the pipe outlet for (c) $\rho_l = 1000\,\mathrm{kg/m^3}$ and (d) $1400\,\mathrm{kg/m^3}$. ($D = 50.0\,\mathrm{mm}, d_p = 1.5\,\mathrm{mm}, \alpha_v = 0.3, \rho_s = 2450\,\mathrm{kg/m^3}, v_m = 3.35\,\mathrm{m/s}, \tau_y = 1.4\,\mathrm{Pa}, K = 2.3\,\mathrm{Pa.s^n}, n = 0.5$)

particles gives rise to a reduction in the effective flow area and consequently higher velocities at the upper regions with more asymmetry in velocity distribution. Figure 3.9 b reveals that the pressure drop across the pipe slightly increases with carrier fluid density, which is probably due to more particle/wall collisions as a result of more suspended solid particles. Based on these findings, it can be concluded that a higher density for the carrier fluid, e.g. from fines may be more favourable for slurry transport, as in this case the particles are more suspended and the delivered concentration of solids can be enhanced, while the increase in the pressure gradient is not significant.

3.4 Conclusions

In this work, a 3D Eulerian-Eulerian CFD model is developed for simulation of turbulent non-Newtonian slurries in a horizontal pipeline. The model is validated for both monodisperse and bimodal particles in a turbulent non-Newtonian carrier covering a range of $d_p = 0.18-2\,\text{mm}$, $\alpha_v = 0.1-0.3$, and $v_m = 2.2-4.5\,\text{m/s}$. Good agreement is found between the CFD predictions and experimental data of chord-averaged solids concentration, especially in the core region i.e., $-0.75 \leq y/R \leq 0.75$. The surface tension modeling was added to the momentum balance equations to help improve the model's performance in the prediction of the flow behavior, which is a novelty to this model. The relatively poor agreement near the pipe invert may arise from the treatment of the solids stress term in the Eulerian-Eulerian model, which is based on empirical constitutive correlations, and inter-particle (or particle-wall) collisions may not be captured well. The model predicts the frictional pressure drop mostly within 15% difference of the experimental data. For a bimodal particles system, the

drag force between two solid phases has a minimal impact on the predicted pressure drop.

Our parametric studies of monodisperse particles in a turbulent non-Newtonian carrier suggest that the frictional pressure drop increases monotonically with increasing particle size, solids concentration, mixture velocity, and carrier fluid density. Although a higher solids concentration leads to an increased pressure gradient, a significantly reduced specific energy consumption is observed when increasing solids concentration from 0.1 to 0.4. A reversal in concentration at the pipe invert is observed in the flow with a higher mixture velocity, with the maximum concentration occurring at the core region of the pipe.

The results of our study confirm that our CFD model can predict the hydrodynamic properties of solid-liquid slurry flow in a broad range of operating conditions. Despite the advantages of the Eulerian-Eulerian model, the fact that this model treats the solid phase as a fluid and considers the particles as continua leads to the inability to represent the discrete nature of the solid phase and is a limitation for this model. The findings are expected to provide guidelines for pipeline operators to optimize the process, considering the specific energy consumption in delivering concentrated slurries in horizontal pipelines. Future work can be extended based on the effect of different rheological models and set of parameters such as yield stress and fluid consistency coefficient with proper validation of the CFD model.

Chapter 4

Computational fluid dynamics (CFD) simulation of three–phase non–Newtonian slurry flows in industrial horizontal pipelines[1]

This chapter presents the results of the oil sands tailings flow simulated with the mixture model. The details of the modeling approach are mentioned in Chapter 2.

4.1 Composition of tailings slurry

The PSD information in five different measurements is presented in Figure 4.1a. As discussed earlier, a sieving method is used to determine the size distribution for solid particles, with mesh sizes from 1.3 to 2000 μm. Particles with sizes below 44 μm are considered as fines and incorporated in the carrier fluid, and the fraction for particles larger than 2000 μm is zero in all of the cases. With these considerations, eight bins for coarse solid particles are formed, from $d_p = 75$ to 1000 μm. The

[1] M. Sadeghi, S. G. Sontti, E. Zheng, X. Zhang. "Computational fluid dynamics (CFD) simulation of three–phase non–Newtonian slurry flows in industrial horizontal pipelines". Submitted to *Chemical Engineering Journal*

compositions data is reported in the form of mass fraction, which is first converted to volume fraction with having the densities of solids and water, and later on, used to calculate the carrier fluid density. It must be noted that Set 1 in Figure 4.1 is the PSD information for the base case and used for all of the cases simulated in the validation section. The slurry density of three representative time windows is depicted in Figure 4.1b.

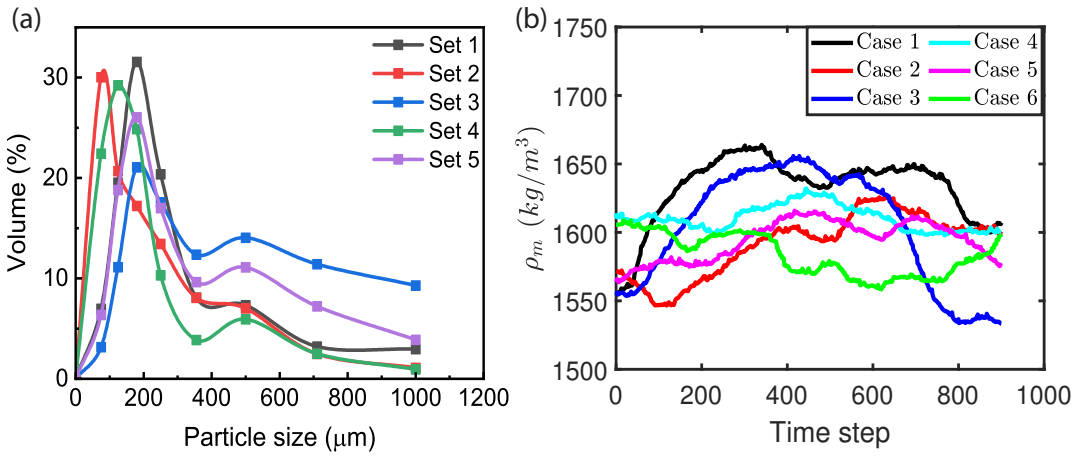

Figure 4.1: [Color] Plots of (a) PSD of the coarse particles for three measurements and (b) mixture density for six representative cases.

4.2 Velocity profiles and flow conditions

Figure 4.2 represents the values of the velocities over 900 time steps for six representative cases (Case 1 to Case 6 in Table 2.7). The velocity values are fairly consistent with a narrow range of fluctuations for VF1 to VF4. However, as observable in Figure 4.2e, VF5 is prone to more frequent and significant fluctuations. This is observed almost for the entire set of data points, indicating that the velocity values at the

pipe invert are significantly influenced by some sort of interference. As mentioned, the velocity values are calculated based on the force exerted by the turbulence eddies on the pipe wall, and due to the presence of solid particles and frequent collisions between them and the pipe wall, the force sensed by the device is not only because of the eddies and contains the effect of solid particles. To eliminate this effect from the average value of VF5, the significantly large and small values compared to the normal range (VF5 $> 18\, ft/s$ and VF5 $< 14\, ft/s$) were removed from the range used for averaging.

The flow characteristics for the representative cases are shown in Figure 4.3 in which panels a to c depict the flowrate, mixture velocity, and pressure at the discharge of the first stage, respectively. The mixture velocity is calculated with respect to the flowrate, which is the reason for the similar trends seen in panels (a) and (b). In each time window, there are specific ranges where the fluctuations are weaker and the flow parameters are more consistent.

Over around a million data points collected, the selection of a proper time window must be made carefully, with monitoring the fluctuations and significant shifts in the flow conditions. A 30–minute time window is selected as the initial step, and the data points are plotted against the time steps. If the oscillations over the entire time window or a portion of it are insignificant and the flow conditions are relatively consistent, that time window is chosen for simulations. Averaging the values over the selected time window is performed, and the cases are prepared.

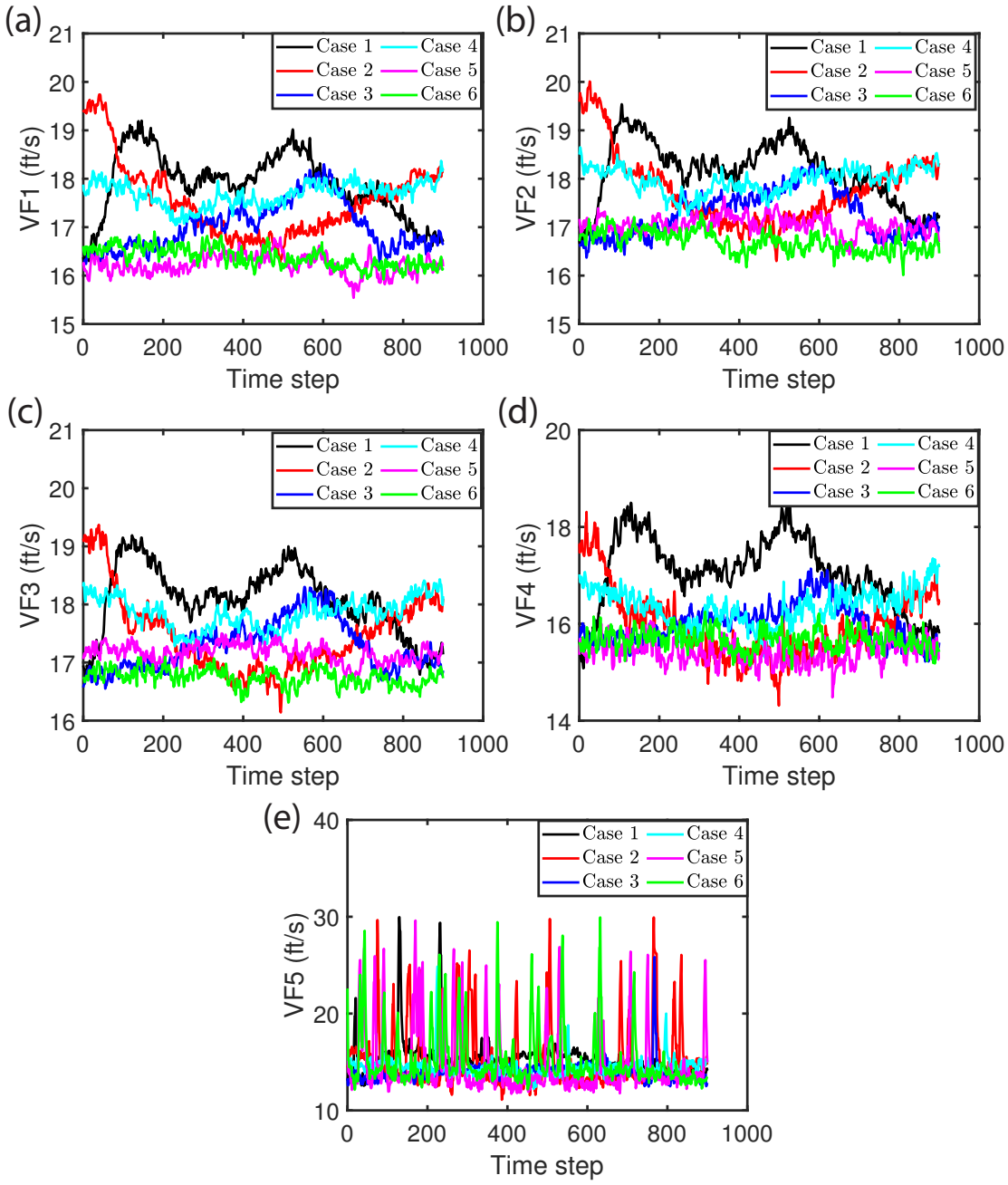

Figure 4.2: [Color] Plots of (a) VF1, (b) VF2, (c) VF3, (d) VF4, and (e) VF5 vs time step for six representative cases.

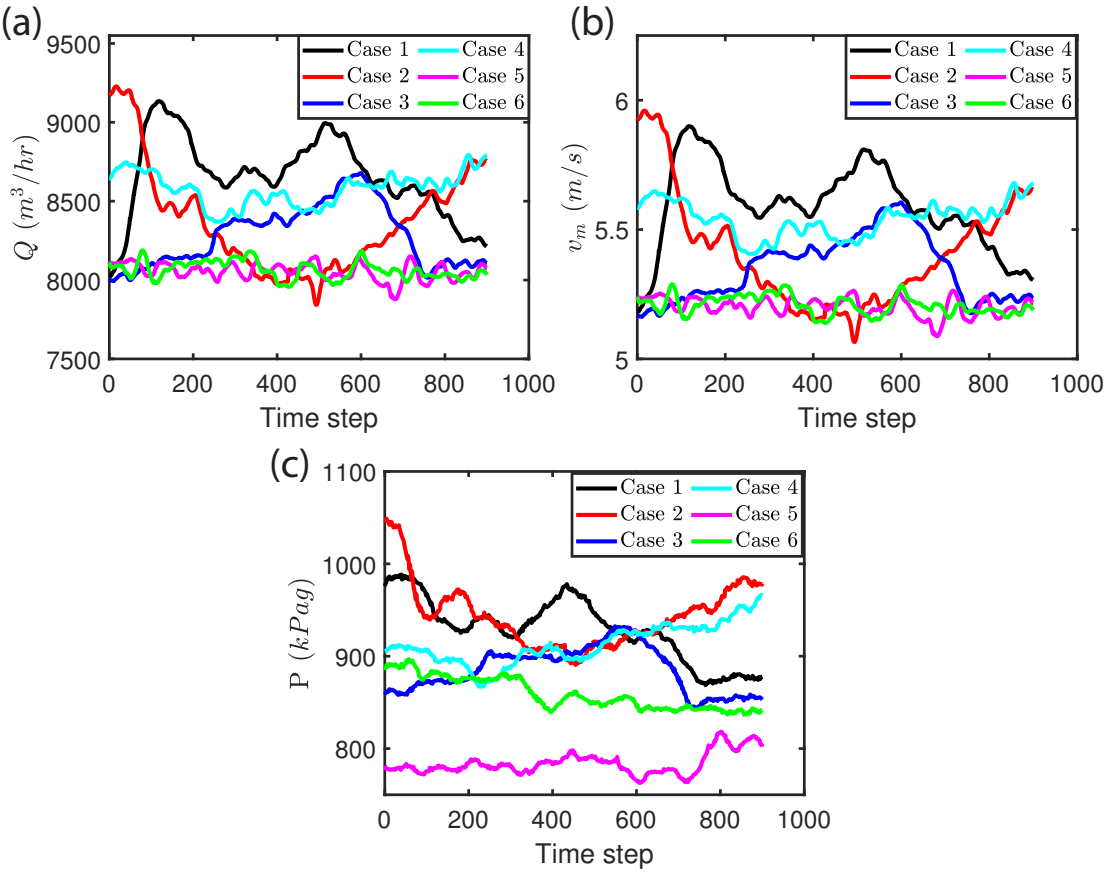

Figure 4.3: [Color] Plots of (a) volumetric flowrate, (b) mixture velocity, and (c) gauge pressure at the first pump discharge vs time step for six representative cases.

4.3 Grid independence

Three grids with similar structure but different number of elements (109125, 438000, and 741065 elements) were designed as shown in Figure 4.4 b–d. The details of the flow conditions of the simulated case can be seen in Table 2.7 as Case 2. Figure 4.5a–c exhibit the comparison of the calculated carrier velocity distribution, the first solid phase velocity distribution and carrier concentration distribution, respectively at a distance of 100 m from the inlet over the three designed grids. The distributions are

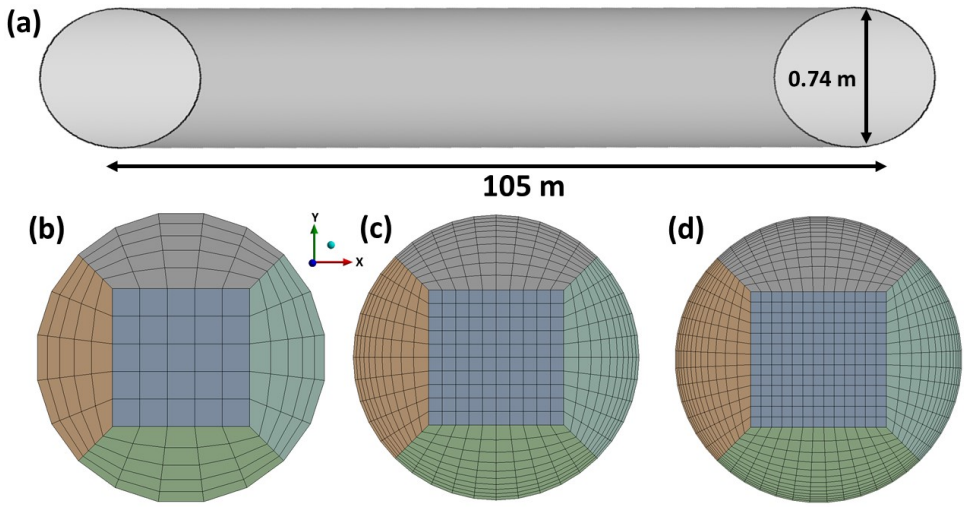

Figure 4.4: (a) Schematic of the three–dimension computational geometry with the channel dimensions. Axial view of different grid structure (b) coarse, (c) fine, and (d) finer meshes.

almost uniform for the coarse, fine, and finer grids. Especially for the fine and finer meshes, nearly no differences are seen for both carrier and first solid velocity and concentration distribution, proving that the so–called 'fine' mesh in this section is appropriate to be used for all of the simulations, as the results are independent of the number of elements. Figure 4.6 shows the contours of velocity and volume fraction of the carrier fluid on separate cross–sectional planes at the inlet, and axial distances of 25, 50, 75, and 100 m. As depicted in Figure 4.6, the distributions do not change after 50 m of the pipe inlet for both velocity and volume fraction. This analysis demonstrates that the flow has reached the fully–developed state before the pipe outlet, where the flow behavior is independent of the axial distance. Accordingly, for the analysis of the CFD results in the the radial direction, a plane at z = 100 m was used to export the data.

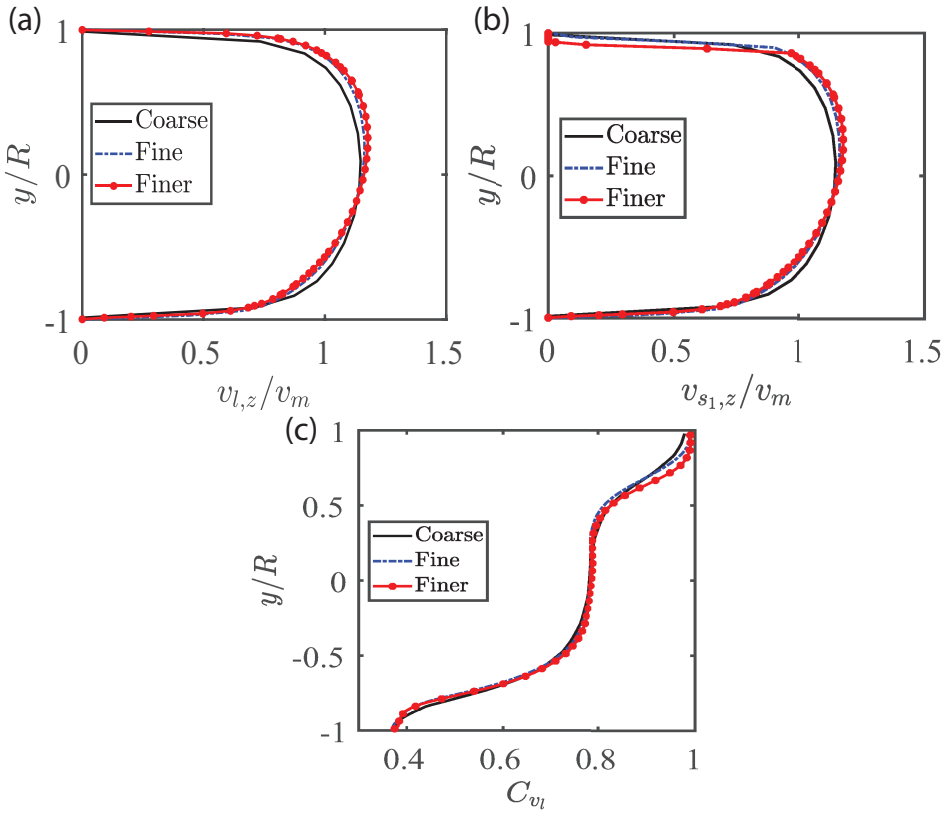

Figure 4.5: Plots of (a) carrier velocity, (b) first solid phase velocity, and (c) carrier volume fraction distributions with the coarse, fine and finer grids. ($D = 74.0\,\text{cm}, \alpha_v = 0.23, v_m = 5.35\,m/s, \rho_s = 2650\,\text{kg/m}^3, \rho_l = 1278\,\text{kg/m}^3, \tau_y = 0.04696\,\text{Pa}, \mu_c = 0.00165\,\text{Pa}^{1/2}.\text{s}^{1/2}$)

4.4 Model validation

To demonstrate the accuracy and validity of the developed model, CFD simulations were compared with field data of velocity distribution and pressure gradient. The accordance of the CFD predictions with field data demonstrates that the physics of the system has been well defined, and the model can be considered a reliable tool to perform a parametric study on a similar system. The comparisons between

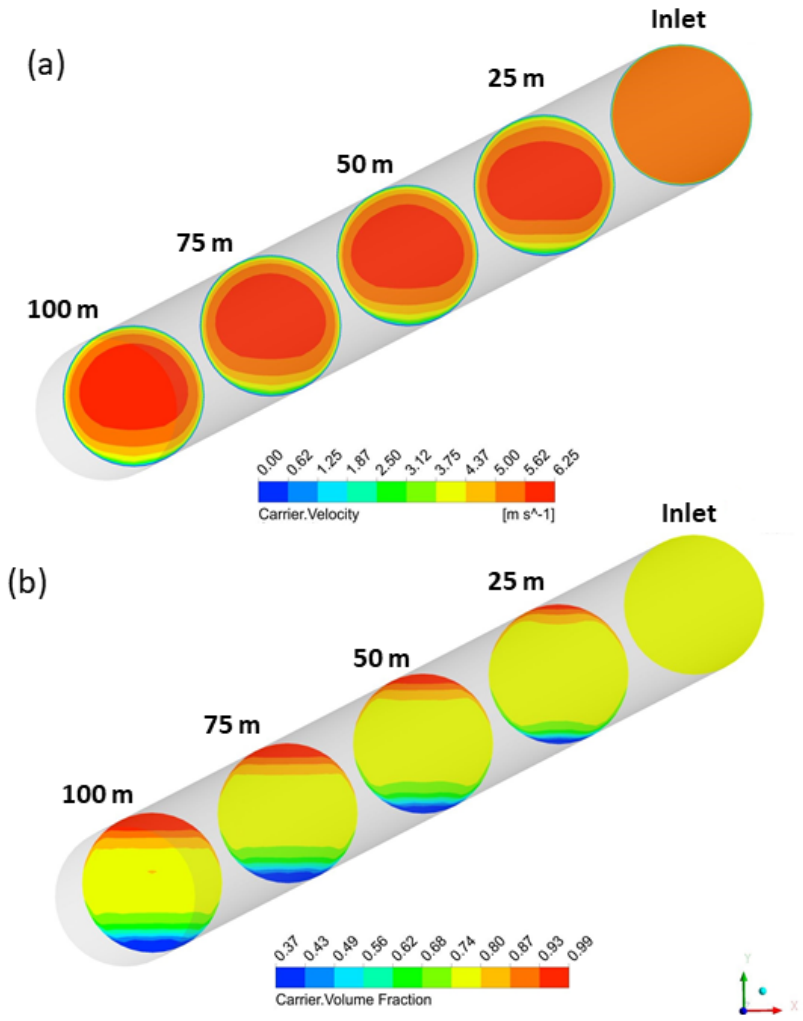

Figure 4.6: [Color] Contours of (a) carrier velocity and (b) volume fraction distributions at the inlet and axial distances of 25, 50, 75, and 100 m. ($D = 74.0\,\text{cm}, \alpha_v = 0.23, v_m = 5.35\,m/s, \rho_s = 2650\,\text{kg/m}^3, \rho_l = 1278\,\text{kg/m}^3, \tau_y = 0.04696\,\text{Pa}, \mu_c = 0.00165\,\text{Pa}^{1/2}.\text{s}^{1/2}$)

CFD–predicted and measured velocity distribution and pressure gradient are presented in this section.

The details of the flow conditions for the cases simulated for the validation pur-

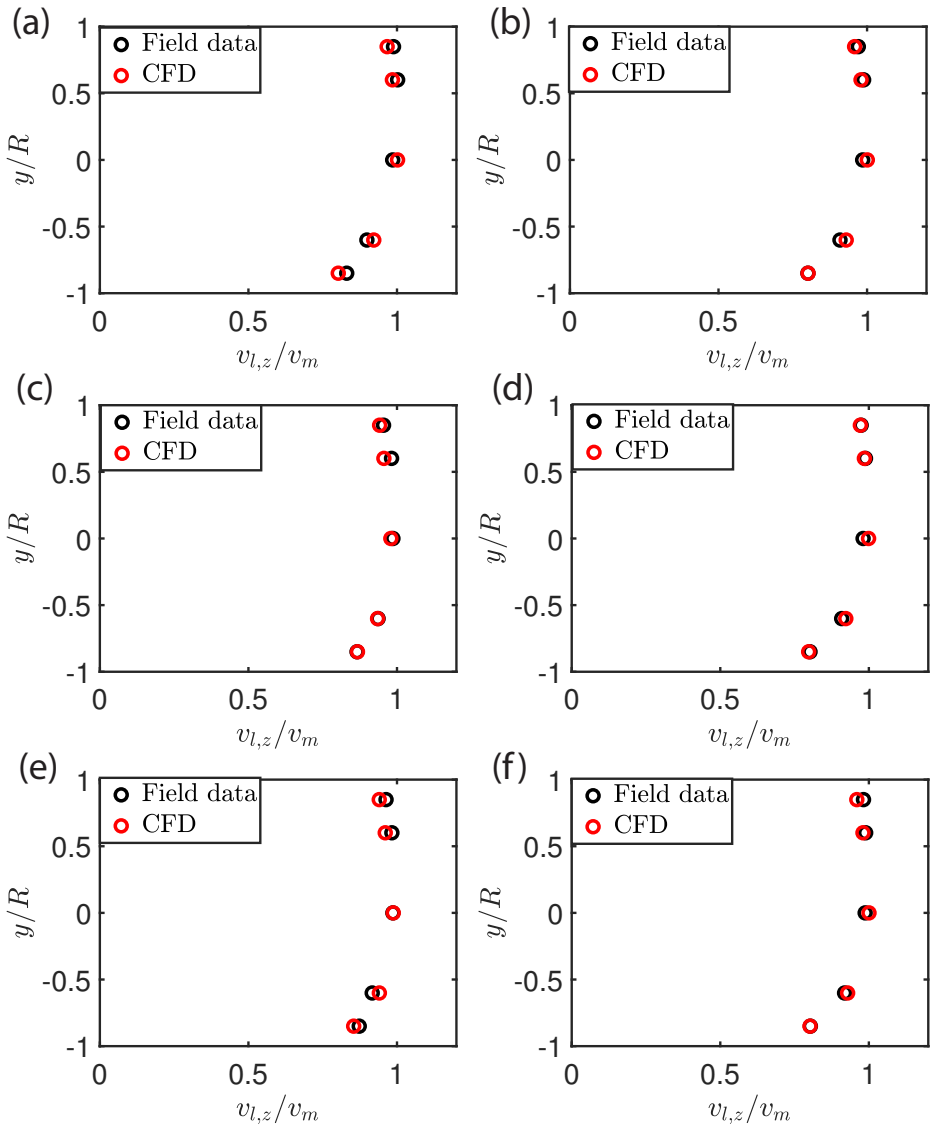

Figure 4.7: [Color] Comparisons of the velocity distributions predicted by CFD (the red circles which represent the interpolated CFD values) and measured at the field (black circles) for six different cases (a) Case 2, (b) Case 3, (c) Case 7, (d) Case 8, (e) Case 9, and (f) Case 10.

pose are provided in Table 2.7. Figure 4.7 depicts the comparison between the CFD–predicted velocity distribution and the measured ones at the field for six dif-

ferent cases. The results demonstrate exceptional agreement between the carrier fluid velocity data exported from the CFD simulations and measured at the field. For most of the data points, the CFD and field values overlap, with insignificant discrepancies for some data points.

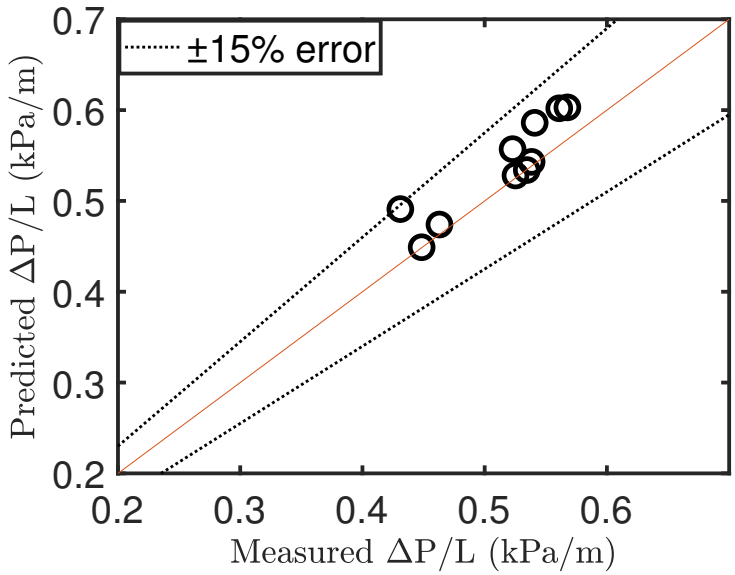

Figure 4.8: Parity plot of frictional pressure drop obtained from CFD vs. field data. The solid line is the bisector and the two dashed lines denote errors of ±15%.

The accuracy of the model and validity of the physics defined for the system was also examined by the comparison of pressure gradients predicted by CFD and measured pressure at the industrial pipeline. Overall, the comparison was made for 10 distinct cases over 10 different time windows, and the results are presented in Figure 4.8. For all of the cases, the predictions are in accord with the field data with an error margin of less than 15% which can be considered highly accurate for an industrial–scale pipeline. The details of the flow conditions, such as the mixture velocity, carrier density, total solids concentration, etc., are presented in

Table 2.7. The frictional pressure drop inside a pipe results from particle–wall and particle–particle interactions [24]. The field measurements and CFD predictions show an increase in the frictional pressure gradient as the mixture velocity and total solids concentrations increase. A higher mixture velocity and solids concentration lead to enhanced and more frequent collisions between particles and with the pipe wall, resulting in a higher pressure drop.

In summary, the model was proven to be accurate and sufficiently sophisticated in physics based on the comparison of CFD–predicted velocity distribution and pressure gradient with field measurements.

4.5 Sensitivity analysis

4.5.1 Selection of the drag model

Choosing an appropriate drag model is crucial in the CFD simulation of any multiphase flow with mixture model as it will directly influence the slip velocity which is the only parameter that distinguishes the phases in mixture model. In Ansys Fluent, the available drag models are (a) schiller–naumann [103], (b) morsi–alexander [104], (c) universal–drag [105], (d) symmetric [43], (e) ishii–zuber [106], and (f) tomiyama [107]. Figure 4.9 shows the contours of bitumen concentration distribution in radial direction with different drag models between bitumen and the carrier fluid. The results show that except for the symmetric drag model, all other drag models lead to total accumulation of bitumen droplets at the pipe obvert. Data collection from precise location for bitumen concentration distribution is challenging. We compared the bitumen concentration in two samples collected from the top and middle parts

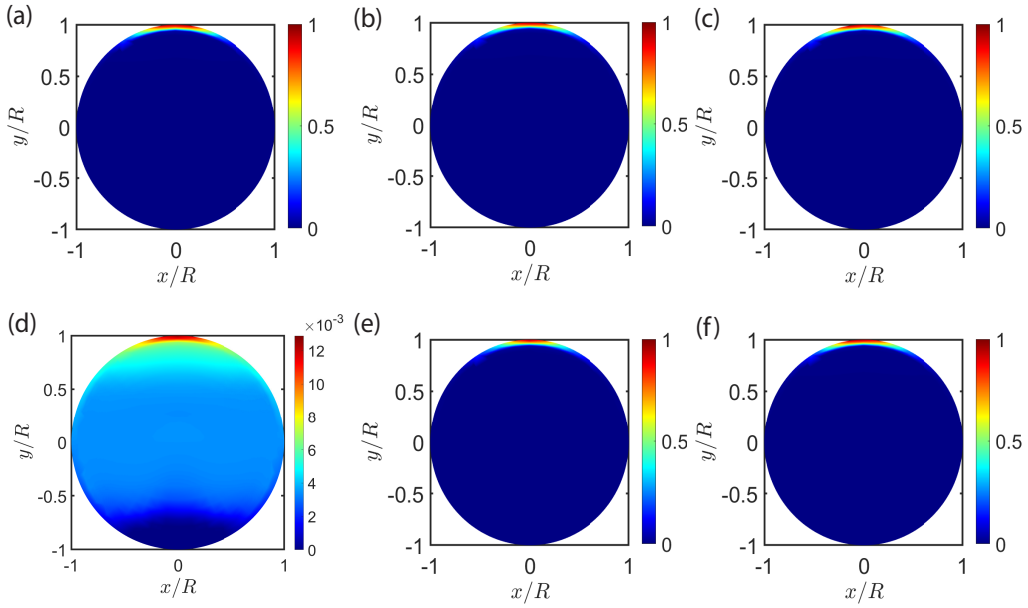

Figure 4.9: [Color] Contours of concentration distribution of bitumen with using different drag models between the carrier fluid and bitumen. The drag models are: (a) schiller–naumann, (b) morsi–alexander, (c) universal–drag, (d) symmetric, (e) ishii–zuber, and (f) tomiyama

of the pipe, and bitumen concentration at the top region was twice as high as in the core region. On this basis, the symmetric model was selected as the carrier–bitumen drag model for this study.

4.5.2 Bitumen droplet size

As bitumen is a dispersed phase in the form of droplet, a diameter needs to be considered for these droplets in the simulation. There are multiple studies in the literature for size characterization of bitumen droplets and aggregates in the flotation column, however, no data has been reported for bitumen droplet size in the flow in a horizontal pipeline. For the size distribution of bitumen droplets in a flotation

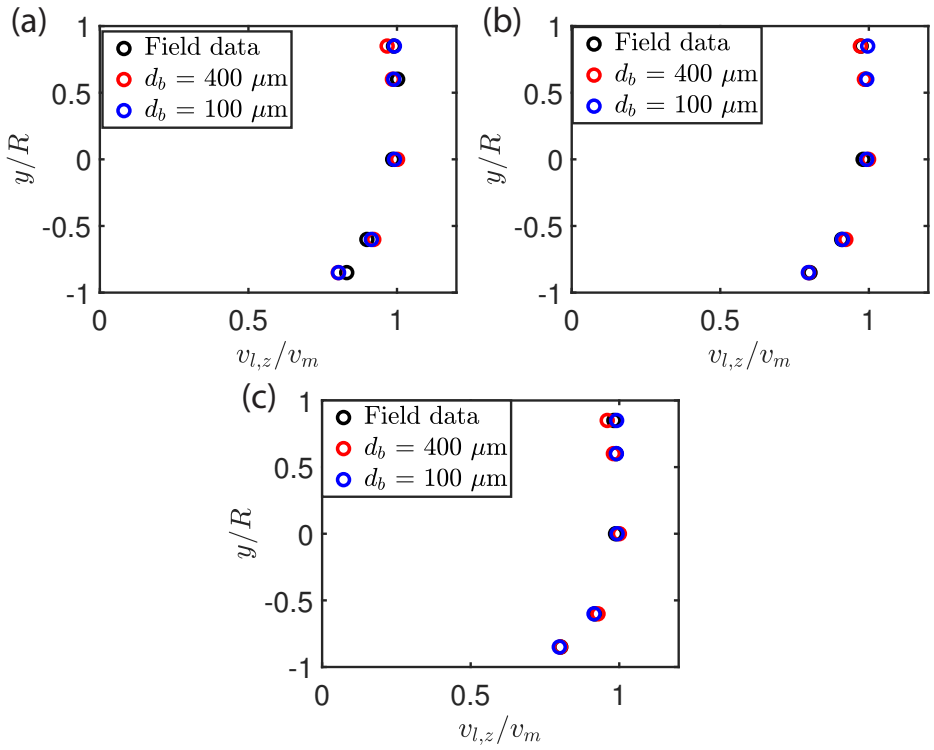

Figure 4.10: [Color] Effect of bitumen droplet size on the velocity distribution for three different cases (a) Case 2, (b) Case 7, (c) Case 10.

column, it has been reported that most droplets are less than 800 μm in size [108, 109]. On this basis, a comprehensive analysis was performed to find the appropriate diameter for bitumen droplets in which the CFD prediction are in accord with the field data with the lowest error. The maximum diameter considered for the droplet was 800 μm as it was assumed that the droplets can not be larger than the aggregates in the flotation column, and the lower band was considered to be 100 μm. It was found that the flow behavior is almost insensitive to the bitumen droplet size. This was expected as the volume fraction of bitumen is low and the considered range for the size is not very broad. Figure 4.10 shows the velocity distribution is in the same form

with droplets sizes of 100 μm and 400 μm for three representative cases. However, the diameter of 400 μm overall gave better predictions of velocity and pressure gradient, and was selected as the input for the simulations in this study.

4.6 Bitumen concentration distribution

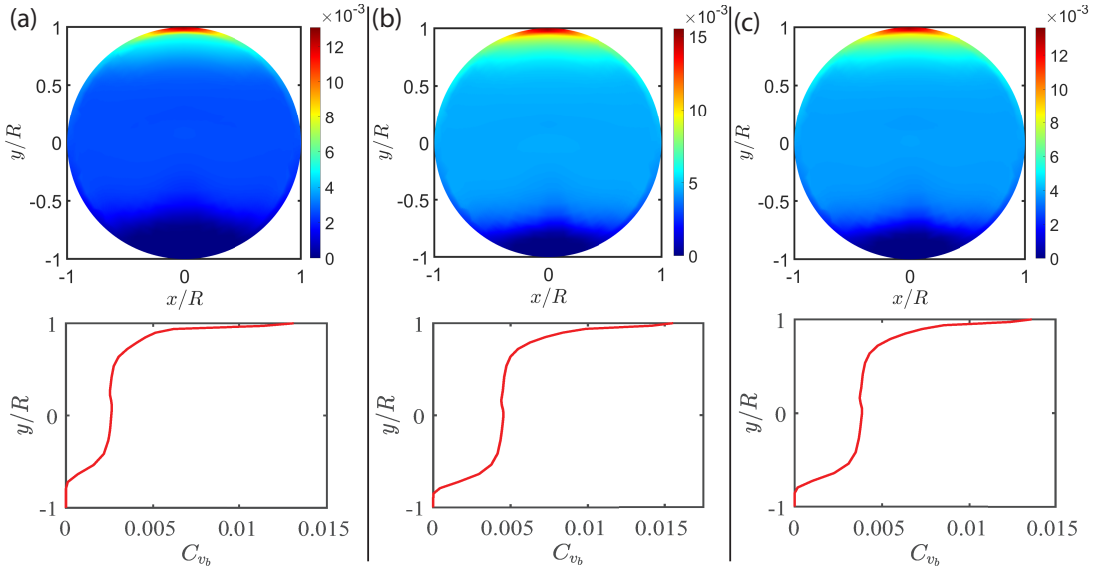

Figure 4.11: [Color] Contours of bitumen concentration distribution and plots of bitumen concentration distribution on the vertical centerline for three representative cases (a) Case 1, (b) Case 9, and (c) Case 5.

Figure 4.11 depicts the contours of bitumen concentration distribution in radial direction and plots of bitumen concentration on the vertical centerline at a distance of 100 m from the inlet for three representative cases. As shown in Figure 4.11, bitumen droplets mostly move to the top region of the pipe due to a lower density, but some droplets are still dispersed into the flow and bitumen concentration in the core is around half of the top region of the pipe. The distribution of bitumen droplets

in the radial direction is a result of competition between the buoyancy effect which leads to accumulation of the drops at the top part, and turbulent dispersion which tries to bring the droplets back into the flow. This prediction of the trend in bitumen concentration distribution is crucial for future analysis on separation of the bitumen or any other third phase as long as it is a fluid and immiscible with water.

In the first section of Table 4.1, the distribution of bitumen droplets at the top one–fourth (upper 25 %) and top half (upper 50 %) of the pipe (cross–sectional view) is presented for the cases shown in Figure 4.11. This analysis helps to design an efficient method for further treatment of the slurry for bitumen separation, with targeting the appropriate section of the pipe where a high percentage of droplets reside. As the results demonstrate, the majority of bitumen droplets are at the top half of the pipe, with around 72 % for Case 1 and 67 % for the other two cases. Therefore, the treatment of the flow of the top half section of the pipe can lead to an acceptable recovery of bitumen.

4.7 Solids concentration distribution

One of the most important aspects of the slurry flow behavior is the distribution of solid particles in radial direction. The solids concentration distribution influences other flow parameters and conditions such as pressure drop and velocity distribution directly and is of great importance in pipeline design [5]. As discussed earlier, the solid particles in this study are polydisprese and have been considered as separate secondary phases in the mixture model. This approach makes the investigation of concentration distribution for solid particle with specific sizes possible. In Figure 4.12, the contours of concentration distribution of solid particles are shown

Case	Upper 25%	Upper 50%
1	47.02	71.97
5	42.31	67.37
9	41.27	66.27
v_m = 3.5 m/s	48.96	74.09
v_m = 4.5 m/s	45.21	70.77
v_m = 5.5 m/s	42.93	68.58
v_m = 6.5 m/s	41.13	66.68
PSD: Set 1	43.08	68.65
PSD: Set 2	43.7	73.16
PSD: Set 3	43.35	71.48
PSD: Set 4	43.7	75.28
$\mu_c = 0.001\ Pa^{1/2}.s^{1/2}$	44.26	70.8
$\mu_c = 0.003\ Pa^{1/2}.s^{1/2}$	42.52	67.57
$\mu_c = 0.006\ Pa^{1/2}.s^{1/2}$	41.35	65.52
$\mu_c = 0.01\ Pa^{1/2}.s^{1/2}$	40.31	63.87
θ = -10	43.19	68.12
θ = -5	44.15	69.12
θ = 5	44.0	70.29
θ = 10	42.53	69.19

Table 4.1: Bitumen distribution at top 25% and 50% sections of the pipe. Note that the mentioned values are the ratio of bitumen volume fraction at each section to the total bitumen volume fraction in percentage. Case 2 is the base case for parametric study.

for Case 2 from the smallest to largest particles, respectively. As depicted in Figure 4.12a–h, the particles with smaller sizes (75 to 250 μm) are more dispersed in the flow while larger particles (Figure 4.12e–h) tend to settle and accumulate at the pipe invert. This observation is consistent with the experimental measurements of solids concentration distribution for multisized zinc particles through a lab–scale pipe reported by Kaushal and Tomita [110]. This trend in solids distribution is mainly due to gravitational effect, which makes the larger particles with higher weights to settle, but smaller particles are more prone to dispersion owing to lower weights. Based on these results, the pipe in the cross–sectional view can be divided into three zones as explained by Liu et al. [39]. The bottom section is the first zone where the larger particles settle, the second zone is the central region where the flow is steady and the particles are transported with the flow and are smaller in size, and the top part is the third zone where the small particles are suspended.

4.8 Parametric study

In this section, a systematic parametric study is presented to investigate the effect of various flow conditions on the behavior of the three–phase slurry flow. The effects of particles size distribution, mixture velocity, Casson viscosity, and pipe angle on the pressure drop, solids concentration distribution, carrier velocity distribution, turbulent kinetic energy, and bitumen concentration distribution were studied. The solids concentration distribution and pressure drop determine the specific energy consumption (SEC) for the pipeline, which is a critical economic and environmental parameter. A lower SEC is favorable, and leads to transportation of more solid particles with a lower energy consumption. The magnitude and distribution of turbulent

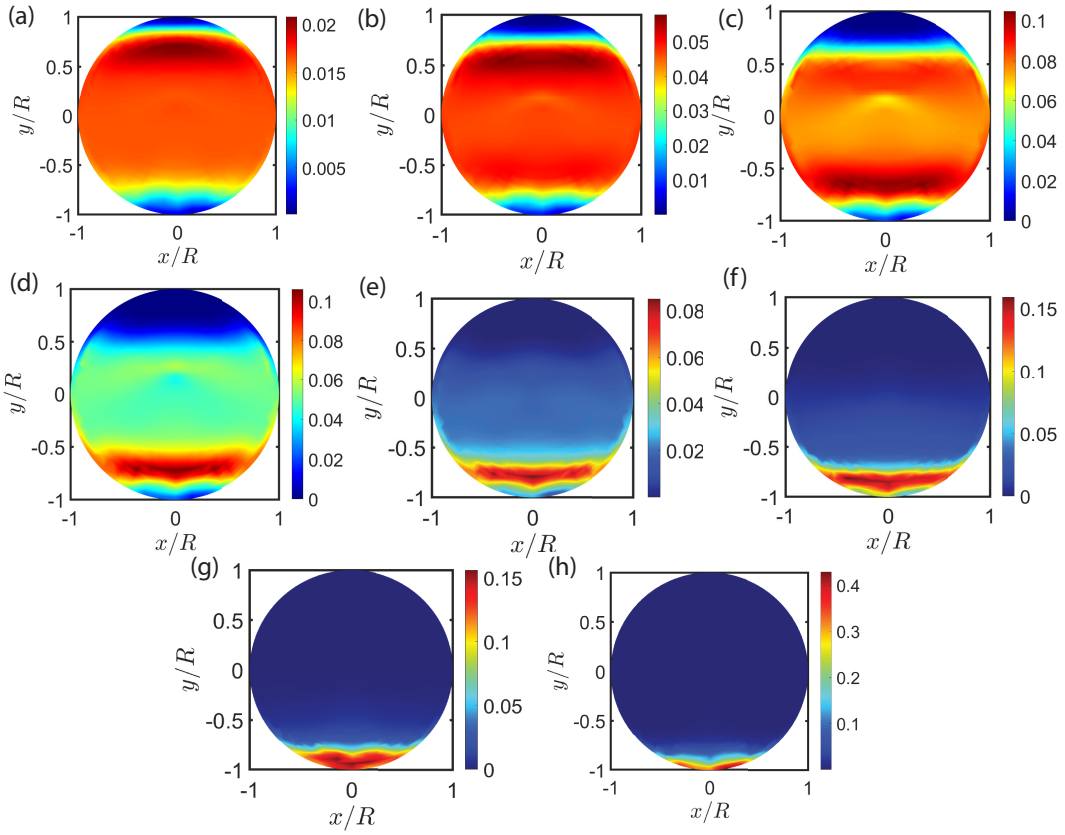

Figure 4.12: [Color] Contours of concentration distribution of solid particles with sizes (d_p) of (a) 75 μm, (b) 125 μm, (c) 180 μm, (d) 250 μm, (e) 355 μm, (f) 500 μm, (g) 710 μm, and (h) 1000 μm.

kinetic energy was investigated to evaluate the strength and regime of turbulence in the flow.

For this parametric study, a base case with the flow conditions described as Case 2 in Table 2.7 was chosen. The particles size distribution information was provided in Figure 4.1a (Set1). To understand the role of each parameter on the flow behavior, other flow conditions were kept constant. The results demonstrate the nontrivial effect of aforementioned parameters on the flow behavior of the described slurries.

4.8.1 Effect of mixture velocity

The mixture velocity has been proven to have a significant effect on the flow behavior of slurries [86]. In this section, the effect of mixture velocity has been investigated by varying the flow velocity from 3.5 m/s to 6.5 m/s. In the real process which has been used for validation, the mixture velocity is in a range of 5.1 to 5.7 m/s, which leads to a highly turbulent flow considering the pipe diameter. Reducing the flow velocity to 3.5 m/s can give an idea about the flow behavior in a weak turbulent regime, and by increasing the velocity, the role of a stronger turbulence can be better understood in a three–phase flow with a Casson carrier fluid.

In Figure 4.13 a, the normalized carrier velocity distributions in the vertical centerline have been plotted for the four simulated cases. While the curves of different mixture velocities seem to overlap, a slight shift of the velocity distribution toward a more asymmetrical form is observable with increasing the mixture velocity. The similar normalized velocity distribution demonstrates that the flows for all of the cases are in a similar regime. Similar trend is seen in the work by Zhang et al. [23] but for the solid phase velocity distribution, where the mixture velocity seems to

have a trivial effect on the normalized velocity compared to other parameters.

The pressure drop shows a significant dependency on mixture velocity as depicted in Figure 4.13 b. As the mixture velocity increases and the flow becomes more turbulent, the particle–particle and particle–wall collisions are enhanced significantly, leading to an intensified pressure drop in the pipeline. The pressure drop shows an increase of 200 % from an increase in the mixture velocity of 3.5 to 6.5 m/s. The increase of pressure drop with mixture velocity is fairly linear as shown in this figure. Scaling equation is proposed to predict the pressure drop with any mixture velocity in the turbulent regime. By considering the specific energy consumption for the simulated cases, the pressure drop is increasing with mixture velocity while the delivered concentration is almost the same. It indicates that more power is required for the pumps to operate the transportation per delivered solids.

The plots of nondimensionalized turbulent kinetic energy distribution are presented in Figure 4.13 c. CFD predictions demonstrate that the distribution of TKE is almost in the same form for all cases. Although increasing the mixture velocity intensifies turbulence, the flow regime seems to be similar which is accord with the velocity distributions shown in Figure 4.13 a. The lower TKE at the top region of the pipe for the cases with higher mixture velocities is probably due to presence of more solid particles dispersed in the flow.

Figure 4.13d shows the total solids concentration distribution in radial direction. From the lowest mixture velocity to the highest one, a gradual decrease in the solids concentration in the lower region of the pipe is seen. This shows that more solid particles are suspended owing to the intensified turbulent regime and its mixing effects, but still turbulence is not able to fully suspend the large particles settled on

the pipe invert. Particle–particle interactions also contribute to higher suspension of solids at higher velocities, as these interactions are enhanced with increasing the velocity [5]. These findings are in accord with the results achieved by Kaushal et al. [34] for a two–phase slurry flow with fine particles, they mention that at the higher mixture velocity solid particles tend to migrate to the central part of the pipe due to slip velocity, and higher mixing effect from turbulence. Similar trend was also reported by Li et al. [111] from both experimental and simulation results with the mixture model, where the concentration of solid particles decreases near the pipe invert, and the asymmetry of the concentration curve is reduced at higher velocities.

The effect of mixture velocity on the cross–sectional bitumen concentration distribution is presented in Table 4.1. As the mixture velocity increases, the droplets are more dispersed in the flow leading to a decline in the fraction of bitumen droplets at the top 25 one–fourth and half of the pipe. More specifically, the ratio of bitumen droplets present at the top 25 % of the pipe to the total droplets decreases from 48.96 % for the case with $v_m = 3.5\,\mathrm{m/s}$ to 41.13 % for the case with the highest mixture velocity of $v_m = 6.5\,\mathrm{m/s}$. This change is attributed to the higher mixing as a results of stronger turbulence as the velocity rises, similar to the effect of mixture velocity on the total solids concentration distribution discussed above.

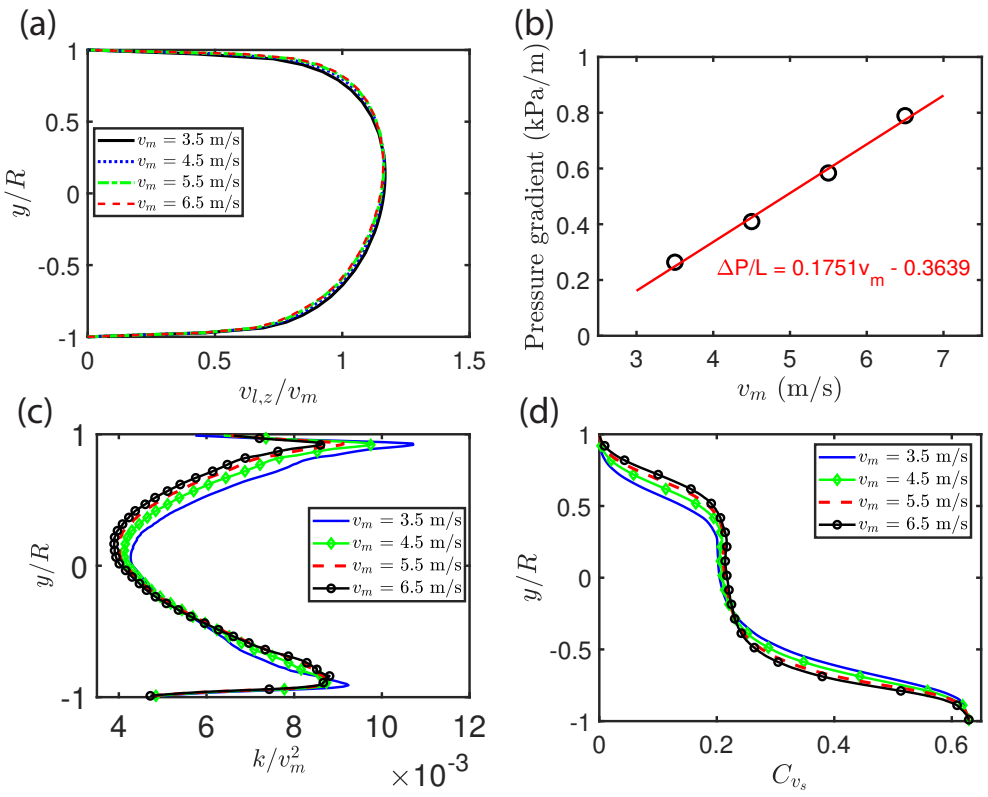

Figure 4.13: Effect of mixture velocity on (a) carrier fluid velocity distribution, (b) pressure gradient, (c) chord–averaged turbulent kinetic energy, and (d) chord–averaged total solids concentration. (D = 74.0 cm, $\alpha_v = 0.23$, $\rho_s = 2650\,kg/m^3$, $\rho_l = 1278\,kg/m^3$, $\tau_y = 0.04696$ Pa, $\mu_c = 0.00165\,Pa^{1/2}.s^{1/2}$)

4.8.2 Effect of particles size distribution (PSD)

In this section, the effect of PSD is investigated, by keeping the total solids concentration constant and varying the fraction of solid phases (corresponding to different sizes). Figure 4.14a depicts PSD information for the four cases simulated for this section. Set 1 represents the base case of the parametric studies, other sets are a result of shifting the maximum fraction to larger solid sizes. Set 4 represents the case with the highest fraction of large solid particles, i.e., $d_p > 500\,\mu m$.

Figure 4.14b–e show the contours of solids concentration distribution for Set 1 to Set 4 cases, respectively. As the concentration of larger particles increases, more particles tend to settle at the pipe invert, and form a sliding bed. Figure 4.14 confirms this argument, showing a higher solids concentration at the pipe bottom and a wide gap between the solids concentration at the top and bottom regions for the Set 4 case (panel e).

Figure 4.15 a shows the carrier velocity distribution at the vertical centerline. The carrier velocity distribution is directly dependent on the solids concentration distribution [5]. The carrier velocity declines near the bottom and shows an increase near the top of the pipe when the fraction of larger sizes increases–see the red curve in Figure 4.15 a. The formation of the bed leads to a decline in the effective flow area and in the mixture and consequently carrier velocity at the bottom region. Contrariwise, less solid particles are present at the top region, and the carrier can freely flow in this region, with having a higher velocity. Zhang et al. [23] reported the similar results for the monodisperse solid particles, where by increasing the size the maximum velocity occurs at a higher vertical position.

The effect of PSD on the frictional pressure drop in the pipe is presented in Figure 4.15 b. The pressure drop increases with shifting the maximum fraction to larger particle sizes, with showing a significant rise from Set 3 to Set 4. This increase in pressure drop was expected and is in accord with other results shown in this section. More particles settlements and particle–wall collisions, also intensified particle–particle collisions due to the lower distance between the particles lead to more energy loss and pressure drop. As mentioned before, the pressure drop in a slurry flow is mostly a result of particle–particle and particle–wall interactions, both intensified for the cases with higher fractions of large solid particles. From Set 1 to Set 3 case, the pressure gradient shows a 5% increase, while from Set 3 to Set 4, a 20% shift is seen in the value of pressure gradient. The effect of PSD on the pressure gradient is similar to the effect of particle size in a two–phase flow with monodisperse particles. Several researchers have studied the effect of particle size on the flow behavior, and reported an increase in the pressure gradient as the particle size is raised [23, 86, 112]. It must be noted that the trend and magnitude of changes in the pressure gradient with respect to PSD is different from slurries with single–sized particles.

In Figure 4.15 c, the chord–averaged turbulent kinetic energy is presented to evaluate the effect of PSD on turbulent regime and velocity fluctuations. The results show that for all of the cases, the turbulent kinetic energy shows a minimum at the pipe center, and local maximums in the bottom half of the pipe. For the fourth case (Set 4), the turbulent kinetic energy is approaching to zero near the wall, which is due to a dense solid bed at the pipe invert, damping the turbulence dramatically. This is consistent with the analysis presented by Antaya et al. [59] and Gopaliya and

Kaushal [113], which show a lower magnitude in the turbulence modulation where the solids concentration is higher. However, for the top region of the pipe in the Set 4 case, the turbulent kinetic energy is higher the other cases. This shows that for this case, turbulent is stronger and more active in this region, constantly changing the direction of the velocity vectors. This is in accord with the velocity distribution depicted in Figure 4.15 a which shows higher velocities at the top region for Set 4.

The effect of PSD on the bitumen concentration distribution is quantitatively analyzed in Table 4.1. As shown, with increasing the fraction of larger sizes from Set 1 to Set 4, a slight increase in the bitumen concentration at the top half of the pipe is seen, which is due to less small particles present in the flow to occupy that region along bitumen. However, the difference for the top 25 % is less pronounced, from 43.08 % for Set 1 to 43.7 % for Set 4 case. Overall, the bitumen concentration distribution in the vertical direction seem to be insignificantly dependent on PSD along with the other parameters.

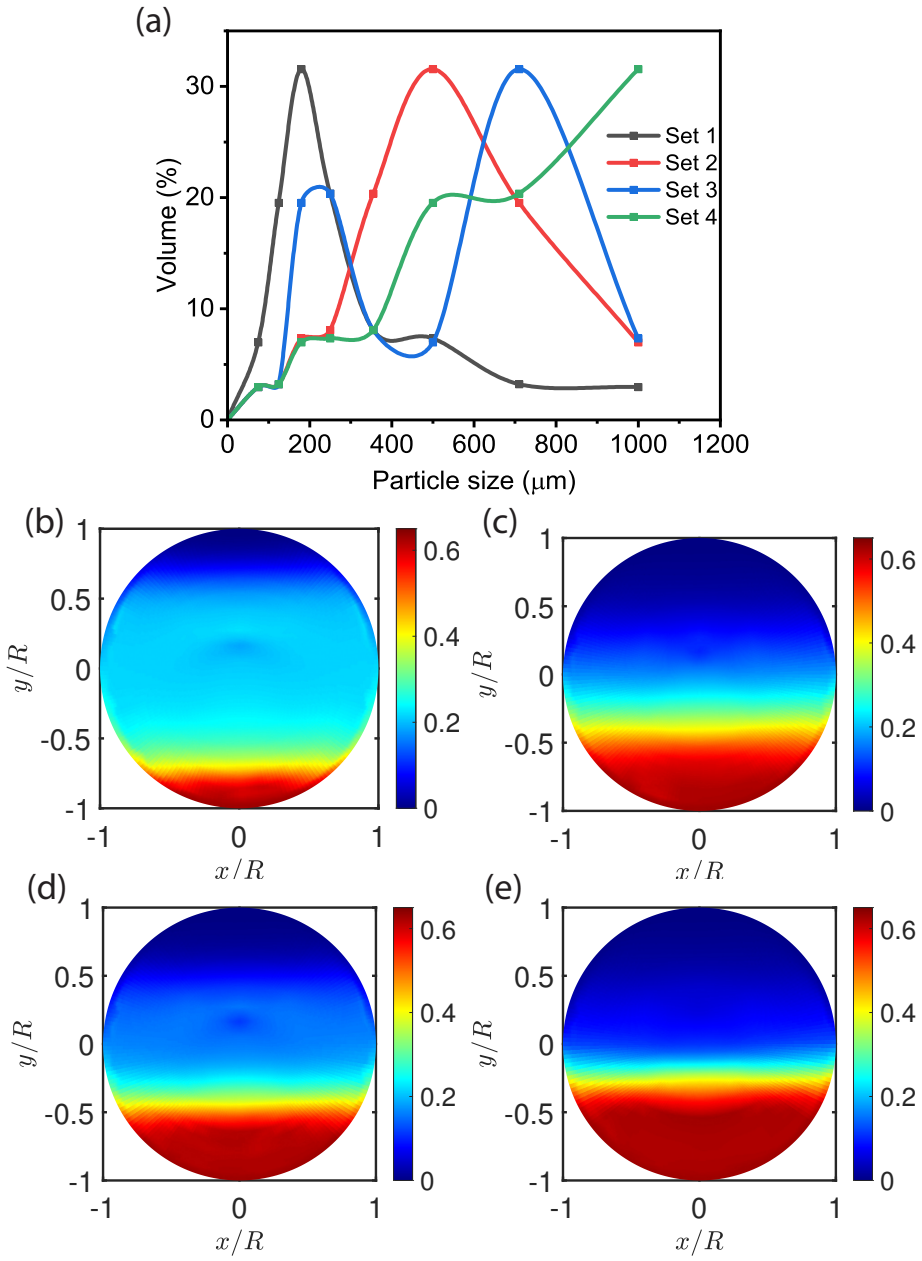

Figure 4.14: [Color] (a) Plot of PSD information for the simulated cases to investigate the effect of PSD, Contours of total solids concentration distribution for (b) Set 1, (c) Set 2, (d) Set 3, and (e) Set 4 cases. (D = 74.0 cm, $\alpha_v = 0.23$, $v_m = 5.35$ m/s $\rho_s = 2650\, kg/m^3$, $\rho_l = 1278\, kg/m^3$, $\tau_y = 0.04696$ Pa, $\mu_c = 0.00165\, Pa^{1/2}.s^{1/2}$)

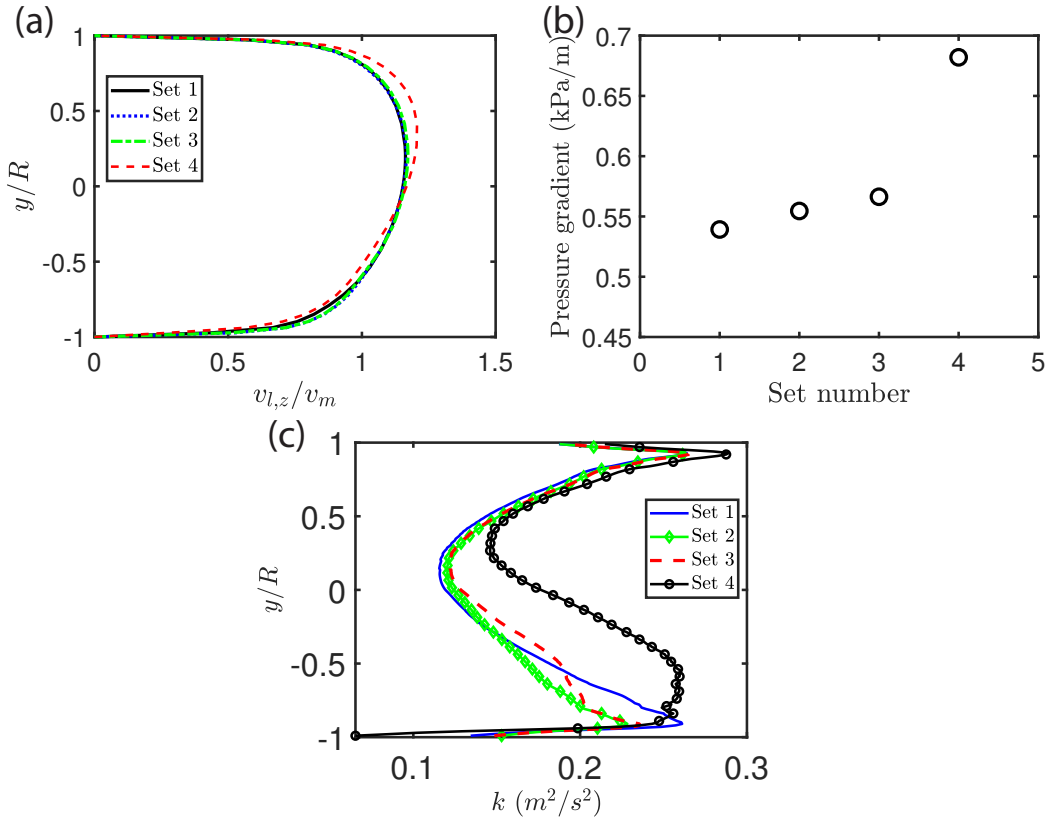

Figure 4.15: Effect of PSD on (a) carrier fluid velocity distribution, (b) pressure gradient, and (c) chord–averaged turbulent kinetic energy. (D = 74.0 cm, α_v = 0.23, v_m = 5.35 m/s ρ_s = 2650 kg/m^3, ρ_l = 1278 kg/m^3, τ_y = 0.04696 Pa, μ_c = 0.00165 $Pa^{1/2}.s^{1/2}$)

4.8.3 Effect of Casson viscosity

Figure 4.16 shows the effect of Casson viscosity on the solids concentration distribution in radial direction inside the pipe. The results show that a higher Casson viscosity results in more suspension of the particles in the carrier fluid (Figure 4.16 d). With increasing Casson viscosity, there is a consistent decrease in total solids concentration at the pipe invert. This observation could be due to the more viscous carrier

fluid, having a higher core viscosity which leads to more support of the particles in the flow and more suspension. Casson plastic viscosity quantifies the internal frictions of a fluid, and it is proven that a more viscous carrier fluid can support more particles in the core region and prohibit the stratification of the flow.

The carrier velocity distributions for the simulated cases are presented in Figure 4.17 a. For case with a higher Casson viscosity, the velocity distribution is more symmetric. In case of a higher viscosity and constant mixture velocity, the Reynolds number decreases as the Casson viscosity rises, resulting in a weaker turbulence in the system. The weaker turbulence in a flow with the higher Casson viscosity is also identified from plots of turbulent kinetic energy.

The pressure gradient for the flows with different Casson viscosity for the carrier fluid was compared as shown in Figure 4.17 b. The results show that the increase in Casson viscosity leads to a lower pressure gradient, however, the changes in pressure gradient are not dramatic. From the case with $\mu_c = 0.001$ to $\mu_c = 0.01\, Pa^{1/2}.s^{1/2}$, a decrease of 7% is identified on pressure gradient. Additionally, the pressure gradient changes are not uniform, with less significant changes occurring as Casson viscosity increases. The interactions between the wall and particles are dampen as the solid particles are more suspended in the flow. On the other hand, the internal frictions are enhanced as the Casson viscosity is raised, which act against each other in affecting the pressure drop. Furthermore, the effect of weakened particle–wall collisions are more effective in reducing the pressure compared to the increase in pressure drop due to more viscous fluid.

In Figure 4.17 c, the radial distributions of turbulent kinetic energy for the four cases are depicted, showing an inverse proportion especially in the core region of the

pipe between the turbulent kinetic energy and Casson viscosity. The relatively lower turbulent kinetic energy for $\mu_c = 0.01$ case at the pipe bottom half may be due to the presence of more solid particles in that region for this case (see Figure 4.16 d) similar to our previous studied parameters. Also as mentioned, turbulence is weaker for the cases with higher Casson viscosity.

These results are consistent with the analysis performed by Zheng et al. [7] on the effect of flow index (n) in a Herschel–Bulkley carrier fluid on the flow behavior of a two–phase slurry. In their study, by increasing the value of flow index, the flow shifts toward a laminar flow, leading to a more uniform solid distribution, lower values for turbulent kinetic energy, and a change in the velocity profile from a turbulent to a laminar flow with a more symmetrical curve.

In the fourth section of Table 4.1, the ratio of the bitumen droplets present at the top 25 and 50 % of the pipe is shown. The results demonstrate that the bitumen ratio at the top region is inversely proportional with Casson viscosity. When the value of Casson viscosity is raised from 0.001 to 0.01 $Pa^{1/2}.s^{1/2}$, the bitumen ration decreases from 44.26 to 40.31 % for the top one–fourth, and from 70.8 to 63.87 % for the top half of the pipe. There is a decrease in the bitumen ratio due to the coexistence of more solid particles with the bitumen droplets at the top region for the case with the highest Casson viscosity, as shown in Fig 4.16.

4.8.4 Effect of pipe angle

In this section, two cases for the inclination with angles of +5 and +10° and two cases for declination with angles of -5 and -10° are simulated. Other pipe characteristics such as diameter and length also the flow conditions are kept constant in these cases.

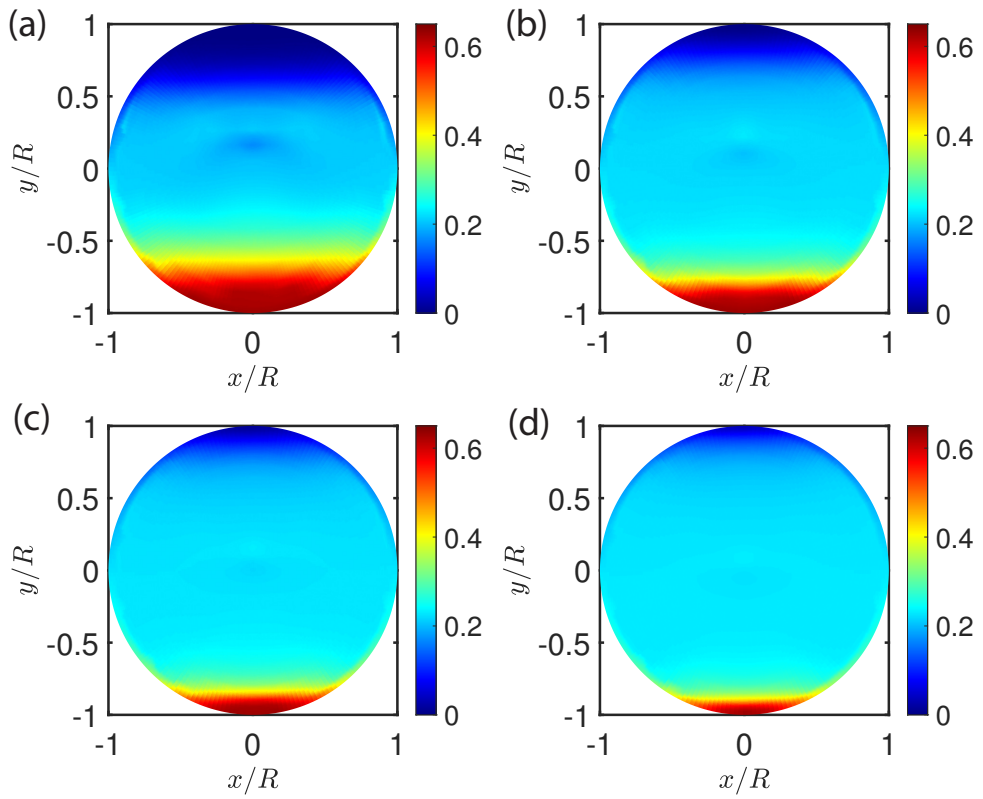

Figure 4.16: [Color] Contours of total solids concentration distribution for the cases with Casson viscosity of (a) 0.001 $Pa^{1/2}.s^{1/2}$, (b) 0.003 $Pa^{1/2}.s^{1/2}$, (c) 0.006 $Pa^{1/2}.s^{1/2}$, and (d) 0.01 $Pa^{1/2}.s^{1/2}$. (D = 74.0 cm, $\alpha_v = 0.23$, $v_m = 5.35$ m/s $\rho_s = 2650\, kg/m^3$, $\rho_l = 1278\, kg/m^3$, $\tau_y = 0.04696$ Pa)

Figure 4.18a shows the carrier velocity distribution in z–direction. The pipe angle has a significant effect on the velocity distribution as the effect of gravity is changing in the cases with the angle (in y–direction). In an inclined pipe, the flow has a higher velocity at the upper half of the pipe, while the velocity distribution is fairly symmetrical in case of a declined pipe. The effect of pipe angle on the pressure drop is shown in Figure 4.18b. The results demonstrate that the pressure drop has a linear relationship with the pipe angle. It must be noted that the negative sign of

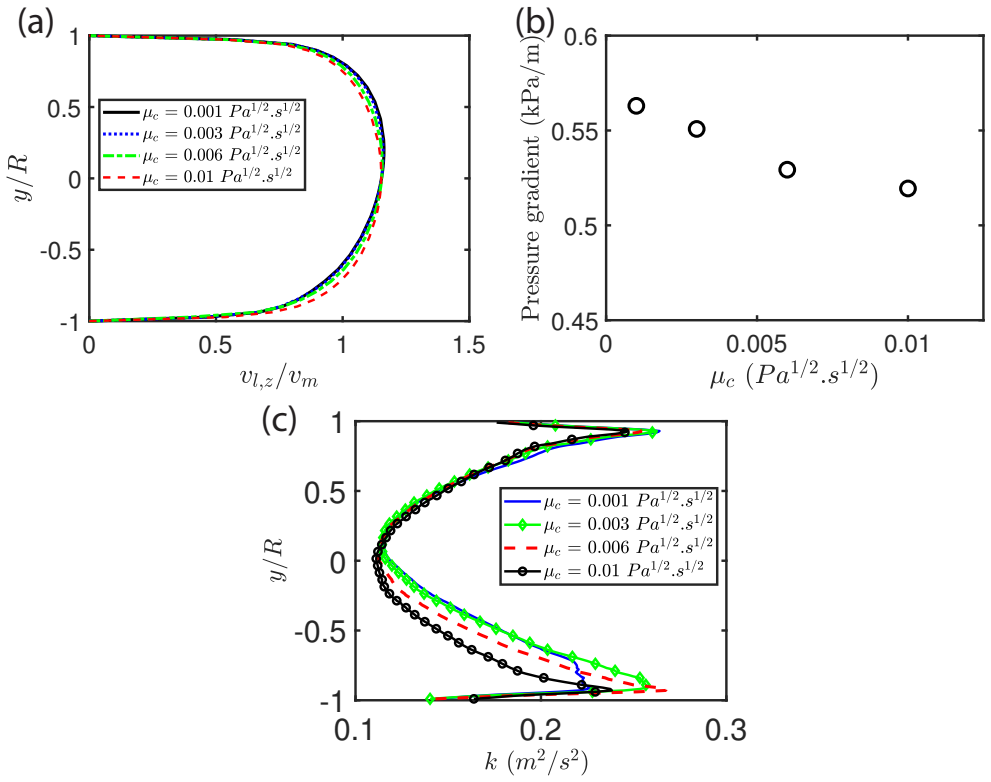

Figure 4.17: Effect of Casson Viscosity on (a) carrier fluid velocity distribution, (b) pressure gradient, and (c) chord–averaged turbulent kinetic energy. (D = 74.0 cm, $\alpha_v = 0.23$, $v_m = 5.35$ m/s $\rho_s = 2650\,kg/m^3$, $\rho_l = 1278\,kg/m^3$, $\tau_y = 0.04696$ Pa)

the pressure drop in the declined cases comes from the zero gauge pressure defined at the pipe outlet as a boundary condition. The experimental and model results achieved by Doron et al. [114] confirm this trend in the pressure drop with the pipe tilt. In case of the declined pipe, the gravity acts as an driving force for the flow and can eliminate the energy required from the pumps if the slope is high enough.

The pipe angle was proven to have also a nontrivial effect on the turbulence regime as shown with the analysis of chord–averaged turbulent kinetic energy in the radial direction in Figure 4.18c. As shown in Figure 4.18c, there are more significant ve-

locity fluctuations and consequently stronger turbulence at the top region for the declined cases as well as at the bottom for the inclined cases. As shown in Figure 4.18d, solids concentration distribution is weakly dependent on the pipe angle, with slight differences at the pipe obvert and invert. This observation is in accord with the experimental results reported by Kesely et al. [115] and Vlasák et al. [22] for two–phase slurries in declined and inclined pipes, which shows when the difference in the pipe angle is not large (less than 20°), the particles distribution is similar. The tendency of solid particles to settle is slightly higher in inclined pipes, which is in accord with previously shown results for velocity distribution and pressure drop. Since the effective flow area of inclined pipes is smaller due to more solid particles at the invert, velocities at the top are higher, while enhanced particle–wall particle–wall interactions result in higher pressure drops.

As shown in Table 4.1, the pipe angle has a non–uniform effect on the bitumen concentration distribution. In the case of shifting from the negative values of the pipe angle to the positive values of the pipe angle (inclined pipes), the bitumen ratio increases at first, then declines further as the angle increases. However, the magnitude of the changes in bitumen concentration distribution with the pipe angle is insignificant and can almost be ignored.

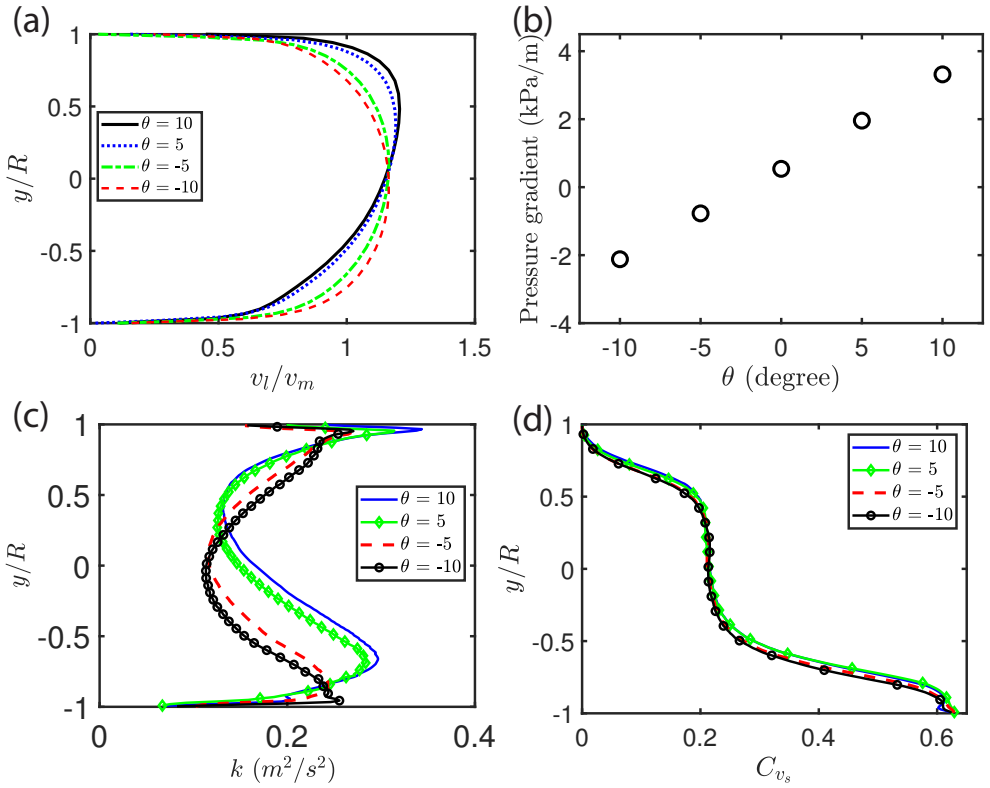

Figure 4.18: Effect of pipe angle on (a) carrier fluid velocity distribution in the z direction, (b) pressure gradient, (c) chord–averaged turbulent kinetic energy, (d) chord–averaged total solids concentration. (D = 74.0 cm, $\alpha_v = 0.23$, $v_m = 5.35$ m/s $\rho_s = 2650\, kg/m^3$, $\rho_l = 1278\, kg/m^3$, $\tau_y = 0.04696$ Pa, $\mu_c = 0.00165\, Pa^{1/2}.s^{1/2}$)

4.9 Conclusions

We developed an efficient three-dimensional computational CFD model to study the flow behavior of a turbulent three-phase non-Newtonian tailings slurry flow in an industrial pipeline. The Gidaspow drag model was selected for carrier–solids, and the sub–models for KTGF were selected from the tested standard models. The SST k–ω turbulence model was used to model highly turbulent flow in a pipeline. The Casson rheological model coupled to capture the non–Newtonian behavior of the

carrier fluid in a slurry system. The accuracy of the model was proved by validating the results against collected filed data. The CFD results showed exceptional agreement with the field data, with errors of $< 3.5\%$ for velocity distribution and $< 15\%$ for the pressure drop. We further extended our CFD model applicability to study a comprehensive parametric study to investigate the influence of mixture velocity, particle size distribution, carrier fluid rheology, and pipe angle on the behavior of the slurry flow, including bitumen concentration, solids concentration, and pressure drop. It must be noted that although the mixture model provided an acceptable description of the flow behavior, the lack of interphase interactions in this model is a drawback to the mixture model which may be important for accurate and detailed simulation of a multiphase system.

The results of the CFD demonstrated that most bitumen droplets reside in the top region of the pipe and selective treatment of the top region may lead to an acceptable bitumen recovery. The CFD predictions on the bitumen concentration distribution would be helpful for the separation of bitumen residues. The developed CFD model provides a powerful tool to predict flow behaviors during highly turbulent slurry transport and may guide the process design for bitumen recovery on an industrial scale.

Chapter 5

Conclusions & future works

5.1 Main results & contributions

The potential of using the CFD technique to model the behavior of concentrated non–Newtonian slurry flows in horizontal pipelines was explored in this thesis. CFD models with Eulerian–Eulerian and mixture approaches coupled with the kinetic theory of granular flow were developed to study the flow of turbulent non–Newtonian two- and three–phase slurries in horizontal pipelines. The Eulerian–Eulerian model was developed for a model system with monodisperse solid particles and validated against the experimental data of solid concentration distribution and pressure gradient from the literature. The CFD predictions by the Eulerian–Eulerian model showed good agreement with the experimental measurements. Overall, the Eulerian–Eulerian model provided a detailed description of the flow features with capturing the effect of interphase forces such as the drag force and turbulent dispersion force. In terms of computational cost, this model was adequately efficient compared to similar DNS and Eulerian–Lagrangian simulations.

Furthermore, the highly complex oil sand tailings flow with polydisperse solid par-

ticles was simulated using the mixture model in an industrial–scale pipeline. The kinetic theory of granular flow was implemented to capture the effect of particle interactions. The model was validated against ten sets of collected filed data of velocity distributions and pressure gradient. The results showed exceptional agreements and the velocity distributions and pressure gradient were predicted with remarkable precision by the mixture model. The mixture model provided an accurate description of the flow behavior with notable efficiency in terms of the computational cost. The mixture model proved to be a promising approach for the study of more complex flows with a higher number of phases and polydisperse solid particles.

The parametric studies were performed with both models and revealed the non-trivial effects of flow conditions such as mixture velocity, solids concentration, particle size distribution, and rheology on flow behavior. Between the examined parameters, the mixture velocity had the most pronounced effects on the flow, which indicated the central role of turbulence in the flow field. With analysis of the specific energy consumption, the results of the Eulerian–Eulerian model would contribute to the optimization of the transport process. The mixture model showed that the majority of bitumen droplets reside at the top section of the pipe with minimal dependency on the tested parameters. Then, selective treatment of the pipe top region would lead to an acceptable bitumen recovery. The results of the simulation of the oil sand tailings flow with the mixture model may contribute to the design and development of separation technology for the bitumen residues inside the pipeline before the tailings ponds which would be significantly beneficial from both environmental and financial aspects.

5.2 Recommendations for future work

This thesis provided systematic CFD studies of slurry flow behaviors with a non–Newtonian carrier fluid in a turbulent regime. Based on the performed work, some extensions and further investigations can be built on the basis presented by this thesis. To this end, the following suggestions can be followed for future studies.

1. Although the mixture model provided valuable insight into the flow behavior of oil sands tailings, the development of an Eulerian–Eulerian model can offer a more detailed description of the phase interactions, and the effect of these interactions on the flow. This is further important for bitumen separation, where the phases interactions can play a major role.

2. Experimental investigations prove the significant improvement of bitumen recovery from the tailings stream by injection of micro/nano—bubbles. The development of CFD simulations to model the behavior of four–phase slurry (solids + carrier fluid + bitumen + air bubbles) can be of tremendous importance for understanding the physical mechanism, the effective parameters, and optimization or enhancement of bitumen recovery.

3. Further investigations on the rheological behavior and the effects of other rheological parameters such as the yield stress, and consistency coefficient and flow behavior index in the Herschel–Bulkley model will give deeper insight into the effect of rheology on the slurry flow behavior.

Bibliography

[1] M. Kesely, "A modification of predictive three-component model for turbulent flows of complex slurries in pipelines based on experimental results," *J. Hydrol. Hydromech.*, vol. 68, no. 3, pp. 223–230, 2020.

[2] L. Pullum, D. V. Boger, and F. Sofra, "Hydraulic mineral waste transport and storage," *Annu. Rev. Fluid Mech.*, vol. 58, pp. 157–185, 2018.

[3] M. Mohaibes and H. Heinonen-Tanski, "Aerobic thermophilic treatment of farm slurry and food wastes," *Bioresour. Technol.*, vol. 95, no. 3, pp. 245–254, 2004, ISSN: 0960-8524. DOI: https://doi.org/10.1016/j.biortech.2004.02.022.

[4] H. Zambrano, L. D. G. Sigalotti, J. Klapp, F. Peña-Polo, and A. Bencomo, "Heavy oil slurry transportation through horizontal pipelines: Experiments and cfd simulations," *Int. J. Multiphase Flow*, vol. 91, pp. 130–141, 2017, ISSN: 0301-9322. DOI: https://doi.org/10.1016/j.ijmultiphaseflow.2016.04.013.

[5] K. Ekambara, R. S. Sanders, K Nandakumar, and J. H. Masliyah, "Hydrodynamic simulation of horizontal slurry pipeline flow using ANSYS-CFX," *Ind. Eng. Chem.*, vol. 48, no. 17, pp. 8159–8171, 2009.

[6] M. Li, Y. He, Y. Liu, and C. Huang, "Hydrodynamic simulation of multi-sized high concentration slurry transport in pipelines," *Ocean Engineering*, vol. 163, pp. 691–705, 2018.

[7] E. Zheng, M. Rudman, S. Kuang, and A. Chryss, "Turbulent coarse-particle non-Newtonian suspension flow in a pipe," *Int. J. Multiphase Flow*, vol. 142, p. 103 698, 2021.

[8] C. Guenther and R. Garg, "Technical report on NETL's non-Newtonian multiphase slurry workshop: A path forward to understanding non-Newtonian multiphase slurry flows," Tech. Rep., 2013.

[9] R. P. Chhabra and J. F. Richardson, *Non-Newtonian Flow in the Process Industries: Fundamentals and Engineering Applications*. Butterworth-Heinemann, 1999.

[10] J Singh, M Rudman, and H. Blackburn, "The influence of shear-dependent rheology on turbulent pipe flow," *J. Fluid Mech.*, vol. 822, p. 848, 2017.

[11] A. S. Arabi and R. S. Sanders, "Particle terminal settling velocities in non-newtonian viscoplastic fluids," *Can. J. Chem. Eng.*, vol. 94, pp. 1092–1101, 2016.

[12] R. Mishra, K. C. Ghanta, A. N. Mullick, and S. L. Sinha, "Experimental and numerical prediction of slurry flow in pipe: A review," *Int. J. Fluid Mech. Res.*, vol. 46, no. 2, pp. 167–185, 2019, ISSN: 2152-5102.

[13] R. Gillies, C. Shook, and K. Wilson, "An improved two layer model for horizontal slurry pipeline flow," *Can. J. Chem. Eng.*, vol. 69, no. 1, pp. 173–178, 1991.

[14] R. G. Gillies and C. A Shook, "Concentration distributions of sand slurries in horizontal pipe flow," *Part. Sci. Technol.*, vol. 12, no. 1, pp. 45–69, 1994. DOI: https://doi.org/10.1080/02726359408906641.

[15] R. G. Gillies and C. A. Shook, "Modelling high concentration settling slurry flows," *Can. J. Chem. Eng.*, vol. 78, no. 4, pp. 709–716, 2000. DOI: https://doi.org/10.1002/cjce.5450780413.

[16] R. G. Gillies, C. A. Shook, and J. Xu, "Modelling heterogeneous slurry flows at high velocities," *Can. J. Chem. Eng.*, vol. 82, no. 5, pp. 1060–1065, 2004. DOI: https://doi.org/10.1002/cjce.5450820523.

[17] D. Kaushal, K. Sato, T. Toyota, K. Funatsu, and Y. Tomita, "Effect of particle size distribution on pressure drop and concentration profile in pipeline flow of highly concentrated slurry," *Int. J. Multiphase Flow*, vol. 31, no. 7, pp. 809–823, 2005.

[18] D. Kaushal and Y. Tomita, "Experimental investigation for near-wall lift of coarser particles in slurry pipeline using γ-ray densitometer," *Powder Technol.*, vol. 172, no. 3, pp. 177–187, 2007.

[19] M. Eesa and M. Barigou, "Horizontal laminar flow of coarse nearly-neutrally buoyant particles in non-newtonian conveying fluids: Cfd and pept experiments compared," *Int. J. Multiphase Flow*, vol. 34, no. 11, pp. 997–1007, 2008.

[20] M Eesa and M Barigou, "CFD investigation of the pipe transport of coarse solids in laminar power law fluids," *Chem. Eng. Sci.*, vol. 64, no. 2, pp. 322–333, 2009.

[21] Y. Ignatenko, O. Bocharov, R. May, A. Gavrilov, A. Shebelev, and A. Dekterev, "Continual modeling of cutting transport during drilling," in *AIP Conference Proceedings*, AIP Publishing LLC, vol. 1939, 2018, p. 020 044.

[22] P. Vlasák, V. Matoušek, Z. Chára, J. Krupička, J. Konfršt, and M. Kesely, "Concentration distribution and deposition limit of medium-coarse sand-water slurry in inclined pipe," *J. Hydrol. Hydromech.*, vol. 68, no. 1, pp. 83–91, 2020. DOI: https://doi.org/10.2478/johh-2019-0023.

[23] M. Zhang, Y. Kang, W. Wei, D. Li, and T. Xiong, "CFD investigation of the flow characteristics of liquid–solid slurry in a large-diameter horizontal pipe," *Part. Sci. Technol.*, vol. 39, no. 6, pp. 712–725, 2021.

[24] K. C. Wilson, G. R. Addie, A. Sellgren, and R Clift, *Slurry Transport Using Centrifugal Pumps*. Springer Science & Business Media, 2006.

[25] V. Pěník, M. Kesely, and V. Matoušek, "Coarse particle support in turbulent flow of visco-plastic carrier," in *EPJ Web of Conferences*, EDP Sciences, vol. 114, 2016, p. 02 090.

[26] V. Matoušek, V Pěník, L. Pullum, and A. Chryss, "Experimental study of bed friction in stratified flow with viscoplastic carrier in pipe," in *International Conference on Transport and Sedimentation of Solid Particles, Delft, The Netherlands*, 2015.

[27] R. Turian, T. Ma, F. Hsu, and D. Sung, "Flow of concentrated non-Newtonian slurries: 1. friction losses in laminar, turbulent and transition flow through straight pipe," *Int. J. Multiphase Flow*, vol. 24, no. 2, pp. 225–242, 1998.

[28] K. Wilson, "A unified physically based analysis of solid-liquid pipeline flow," *Proc. 4th Int. Conf. on Hydraulic Transport of Solids*, pp. 1–16, 1976.

[29] A. A. Gavignet and I. J. Sobey, "Model Aids Cuttings Transport Prediction," *J. Pet. Technol.*, vol. 41, no. 09, pp. 916–921, Sep. 1989. DOI: https://doi.org/10.2118/15417-PA.

[30] P Doron, D Granica, and D Barnea, "Slurry flow in horizontal pipes-experimental and modeling," *Int. J. Multiphase Flow*, vol. 13, pp. 535–547, 1987.

[31] M. R. Rojas and A. E. Sáez, "Two-layer model for horizontal pipe flow of newtonian and non-newtonian settling dense slurries," *Ind. Eng. Chem.*, vol. 51, pp. 7095–7103, 2012.

[32] P. Doron and D. Barnea, "A three-layer model for solid-liquid flow in horizontal pipes," *Int. J. Multiphase Flow*, vol. 19, no. 6, pp. 1029–1043, 1993.

[33] A. Ramadan, P. Skalle, and A. Saasen, "Application of a three-layer modeling approach for solids transport in horizontal and inclined channels," *Chem. Eng. Sci.*, vol. 60, no. 10, pp. 2557–2570, 2005, ISSN: 0009-2509. DOI: https://doi.org/10.1016/j.ces.2004.12.011.

[34] D. Kaushal, T Thinglas, Y. Tomita, S. Kuchii, and H. Tsukamoto, "CFD modeling for pipeline flow of fine particles at high concentration," *Int. J. Multiphase Flow*, vol. 43, pp. 85–100, 2012.

[35] J. P. Singh, S. Kumar, and S. Mohapatra, "Modelling of two phase solid-liquid flow in horizontal pipe using computational fluid dynamics technique," *Int. J. Hydrogen Energy*, vol. 42, no. 31, pp. 20 133–20 137, 2017.

[36] M. Zhou, S. Kuang, K. Luo, R. Zou, S. Wang, and A. Yu, "Modeling and analysis of flow regimes in hydraulic conveying of coarse particles," *Powder Technol.*, vol. 373, pp. 543–554, 2020.

[37] Q. Chen, T. Xiong, X. Zhang, and P. Jiang, "Study of the hydraulic transport of non-spherical particles in a pipeline based on the cfd-dem," *Eng. Appl. Comput. Fluid Mech.*, vol. 14, no. 1, pp. 53–69, 2020. DOI: 10.1080/19942060.2019.1683075.

[38] J. Capecelatro and O. Desjardins, "Eulerian–lagrangian modeling of turbulent liquid–solid slurries in horizontal pipes," *Int. J. Multiphase Flow*, vol. 55, pp. 64–79, 2013, ISSN: 0301-9322. DOI: https://doi.org/10.1016/j.ijmultiphaseflow.2013.04.006.

[39] L. Liu, Z. Fang, C. Qi, B. Zhang, L. Guo, and K.-I. Song, "Numerical study on the pipe flow characteristics of the cemented paste backfill slurry considering hydration effects," *Powder Technol.*, vol. 343, pp. 454–464, 2019, ISSN: 0032-5910. DOI: https://doi.org/10.1016/j.powtec.2018.11.070.

[40] G. V. Messa and V. Matoušek, "Analysis and discussion of two fluid modelling of pipe flow of fully suspended slurry," *Powder Technol.*, vol. 360, pp. 747–768, 2020.

[41] F. Alobaid et al., "Progress in cfd simulations of fluidized beds for chemical and energy process engineering," *Prog. Energy Combust. Sci.*, vol. 91, p. 100 930, 2022, ISSN: 0360-1285. DOI: https://doi.org/10.1016/j.pecs.2021.100930.

[42] G. V. Messa et al., "Computational fluid dynamics modelling of liquid–solid slurry flows in pipelines: State-of-the-art and future perspectives," *Processes*, vol. 9, no. 9, 2021, ISSN: 2227-9717. DOI: 10.3390/pr9091566.

[43] *ANSYS FLUENT Theory Guide 15.0*. ANSYS, Inc, 2013.

[44] M. Padhi, N. Mangadoddy, T. Sreenivas, T. R. Vakamalla, and A. Mainza, "Study on multi-component particle behaviour in a hydrocyclone classifier using experimental and computational fluid dynamics techniques," *Sep. Purif. Technol.*, vol. 229, p. 115 698, 2019, ISSN: 1383-5866. DOI: https://doi.org/10.1016/j.seppur.2019.115698.

[45] J. Kou, Y. Chen, and J. Wu, "Numerical study and optimization of liquid-liquid flow in cyclone pipe," *Chem. Eng. Process.: Process Intensif.*, vol. 147, p. 107 725, 2020, ISSN: 0255-2701. DOI: https://doi.org/10.1016/j.cep.2019.107725.

[46] H. Shi, M. Li, P. Nikrityuk, and Q. Liu, "Experimental and numerical study of cavitation flows in venturi tubes: From cfd to an empirical model," *Chem. Eng. Sci.*, vol. 207, pp. 672–687, 2019, ISSN: 0009-2509. DOI: https://doi.org/10.1016/j.ces.2019.07.004.

[47] A. Rezaei Gorjaei, M. Soltani, M. Bahiraei, and F. M. Kashkooli, "Cfd simulation of nanofluid forced convection inside a three-dimensional annulus by two-phase mixture approach: Heat transfer and entropy generation analyses," *Int. J. Mech. Sci.*, vol. 146-147, pp. 396–404, 2018, ISSN: 0020-7403. DOI: https://doi.org/10.1016/j.ijmecsci.2018.08.002.

[48] X. Chen and W. Junwu, "A comparison of two-fluid model, dense discrete particle model and cfd-dem method for modeling impinging gas–solid flows," *Powder Technol.*, vol. 254, pp. 94–102, 2014.

[49] L. Chen, Y. Duan, W. Pu, and C. Zhao, "CFD simulation of coal-water slurry flowing in horizontal pipelines," *Korean J. Chem. Eng.*, vol. 26, no. 4, pp. 1144–1154, 2009.

[50] M. Li, Y. He, Y. Liu, and C Huang, "Effect of interaction of particles with different sizes on particle kinetics in multi-sized slurry transport by pipeline," *Powder Technol.*, vol. 338, pp. 915–930, 2018.

[51] R Tarodiya, S Khullar, and B. Gandh, "CFD modeling of multi-sized particulate slurry flow through pipe bend.," *J. Appl. Fluid Mech.*, vol. 13, no. 4, pp. 1311–1321, 2020.

[52] L. Pullum, A. Chryss, L. Graham, V. Matoušek, and V Pěník, "Modelling turbulent transport of solids in non-Newtonian carrier fluids applicable to tailings disposal," in *Int. Conf. Transp. Sediment. Solid Part.*, 2015, pp. 229–239.

[53] B. M. Bossio, A. J. Blanco, and F. H. Hernandez, "Eulerian-Eulerian modeling of non-Newtonian slurries flow in horizontal pipes," in *Fluids Engineering Division Summer Meeting*, vol. 43727, 2009, pp. 525–533.

[54] J. Z. Zhou, H. Li, R. S. Chow, Q. Liu, Z. Xu, and J. Masliyah, "Role of mineral flotation technology in improving bitumen extraction from mined athabasca oil sands—ii. flotation hydrodynamics of water-based oil sand extraction," *Can. J. Chem. Eng.*, vol. 98, no. 1, pp. 330–352, 2020. DOI: https://doi.org/10.1002/cjce.23598.

[55] R. J. Chalaturnyk, J. D. Scott, and B. Özüm, "Management of oil sands tailings," *Pet. Sci. Technol.*, vol. 20, no. 9-10, pp. 1025–1046, 2002. DOI: 10.1081/LFT-120003695.

[56] A. Motamed Dashliborun, J. Zhou, P. Esmaeili, and X. Zhang, "Microbubble-enhanced recovery of residual bitumen from the tailings of oil sands extraction in a laboratory-scale pipeline," *Energy Fuels*, vol. 34, no. 12, pp. 16 476–16 485, 2020. DOI: https://doi.org/10.1021/acs.energyfuels.0c03000.

[57] J. U. Brackbill, D. B. Kothe, and C. Zemach, "A continuum method for modeling surface tension," *J. Comput. Phys.*, vol. 100, pp. 335–354, 1992.

[58] D. Gidaspow, *Multiphase Flow and Fluidization: Continuum and Kinetic Theory Descriptions*. Academic Press, 1994.

[59] C. L. Antaya, K. F. K. Adane, and R. S. Sanders, "Modelling Concentrated Slurry Pipeline Flows," in *Fluids Engineering Division Summer Meeting*, vol. Volume 1: Symposia, Parts A and B, Jul. 2012, pp. 1659–1671. DOI: 10.1115/FEDSM2012-72379.

[60] A. Burns, T. Frank, I. Hamill, and J.-M. Shi, "The favre averaged drag model for turbulent dispersion in eulerian multi-phase flows," in *Conf. on Multiphase Flow, ICMF2004*, vol. 392, Jan. 2004.

[61] P. Chen, "Modeling the fluid dynamics of bubble column flows," Ph.D. dissertation, Washington University in St. Louis, 2004.

[62] C. Laborde-Boutet, F. Larachi, N. Dromard, O. Delsart, and D. Schweich, "CFD simulation of bubble column flows: Investigations on turbulence models in RANS approach," *Chem. Eng. Sci.*, vol. 64, no. 21, pp. 4399–4413, 2009.

[63] W. Liu, Y. He, M. Li, Q. Chen, Y. Liu, and C. Huang, "Computational fluid dynamics modeling of slurry flow in horizontal pipes: Effect of specularity coefficient on hydraulic gradient," *Ocean Engineering*, vol. 238, p. 109 625, 2021.

[64] R. Zhou, N. Yang, and J. Li, "Cfd simulation of gas-liquid-solid flow in slurry bubble columns with emms drag model," *Powder Technol.*, vol. 314, pp. 466–479, 2017.

[65] D. J. Kubicki and S. Lo, "Slurry transport in a pipeline – comparison of cfd and dem models," in *Ninth International Conference on CFD in the Minerals and Process Industries*, 2012.

[66] M Syamlal, W Rogers, and T. J. O'Brien, "Mfix documentation theory guide," Tech. Rep., Dec. 1993.

[67] C. K. K. Lun, S. B. Savage, D. J. Jeffrey, and N. Chepurniy, "Kinetic theories for granular flow: Inelastic particles in couette flow and slightly inelastic particles in a general flowfield," *J. Fluid Mech.*, vol. 140, 223–256, 1984.

[68] D Gidaspow, R Bezburuah, and J Ding, "Hydrodynamics of circulating fluidized beds: Kinetic theory approach," in *Proceedings of the 7th Engineering Foundation Conference on Fluidization*, Jan. 1991, pp. 75–82.

[69] D. G. Schaeffer, "Instability in the evolution equations describing incompressible granular flow," *J. Differ. Equ.*, vol. 66, no. 1, pp. 19–50, 1987, ISSN: 0022-0396.

[70] B. Wu, "CFD simulation of gas and non-Newtonian fluid two-phase flow in anaerobic digesters," *Water Res.*, vol. 44, no. 13, pp. 3861–3874, 2010.

[71] A. Rezaeiha, H. Montazeri, and B. Blocken, "On the accuracy of turbulence models for cfd simulations of vertical axis wind turbines," *Energy*, vol. 180, pp. 838–857, 2019.

[72] F. Kuznik, G. Rusaouën, and J. Brau, "Experimental and numerical study of a full scale ventilated enclosure: Comparison of four two equations closure turbulence models," *Build. and Environ.*, vol. 42, no. 3, pp. 1043–1053, 2007.

[73] F. R. Menter, "Two-equation eddy-viscosity turbulence models for engineering applications," *AIAA J.*, vol. 32, no. 8, pp. 1598–1605, 1994.

[74] A. Rawat, S. N. Singh, and V. Seshadri, "Computational methodology for determination of head loss in both laminar and turbulent regimes for the flow of high concentration coal ash slurries through pipeline," *Part. Sci. Technol.*, vol. 34, no. 3, pp. 289–300, 2016.

[75] J Singh, M Rudman, and H. Blackburn, "The effect of yield stress on pipe flow turbulence for generalised Newtonian fluids," *J. Non-Newtonian Fluid Mech.*, vol. 249, pp. 53–62, 2017.

[76] M. K. Singh, S. Kumar, and D. Ratha, "Computational analysis on disposal of coal slurry at high solid concentrations through slurry pipeline," *Int. J. Coal Prep. Util.*, vol. 40, no. 2, pp. 116–130, 2020.

[77] A. Bordet, S. Poncet, M. Poirier, and N. Galanis, "Advanced numerical modeling of turbulent ice slurry flows in a straight pipe," *Int. J. Therm. Sci.*, vol. 127, pp. 294–311, 2018, ISSN: 1290-0729.

[78] D Cokljat, M Slack, S. Vasquez, A Bakker, and G Montante, "Reynolds-stress model for Eulerian multiphase," *Prog. Comput. Fluid Dyn.*, vol. 6, no. 1-3, pp. 168–178, 2006.

[79] N. Kumar, M. Kumar Gopaliya, and D. R. Kaushal, "Experimental investigations and cfd modeling for flow of highly concentrated iron ore slurry through horizontal pipeline," *Part. Sci. Tech.*, vol. 37, no. 2, pp. 232–250, 2019.

[80] R. Chhabra and J. Richardson, *Non-Newtonian Flow and Applied Rheology: Engineering Applications*. Elsevier, 2011, p. 14.

[81] M. Syamlal, "The particle-particle drag term in a multiparticle model of fluidization," EG and G Washington Analytical Services Center Inc. Morgantown WV (USA), Tech. Rep., 1987.

[82] V. Hernandez-Perez, M. Abdulkadir, and B. Azzopardi, "Grid generation issues in the CFD modelling of two-phase flow in a pipe," *J. Comput. Multiph. Flows*, vol. 3, no. 1, pp. 13–26, 2011.

[83] E. Zheng, M. Rudman, S. Kuang, and A. Chryss, "Turbulent coarse-particle suspension flow: Measurement and modelling," *Powder Technol.*, vol. 373, pp. 647–659, 2020.

[84] M. Manninen, T. Veikko, and K. Sirpa, "On the mixture model for multiphase flow," *VTT Publications*, vol. 288, Jan. 1996.

[85] D. Gidaspow, R. Bezburuah, and J Ding, "Hydrodynamics of circulating fluidized beds: Kinetic theory approach," Illinois Inst. of Tech., Chicago, IL (United States). Dept. of Chemical, Tech. Rep., 1991.

[86] M. Sadeghi, S. Li, E. Zheng, S. G. Sontti, P. Esmaeili, and X. Zhang, "Cfd simulation of turbulent non-newtonian slurry flows in horizontal pipelines," *Industrial & Engineering Chemistry Research*, vol. 61, no. 15, pp. 5324–5339, 2022. DOI: https://doi.org/10.1021/acs.iecr.1c04471.

[87] O. B. Adeyinka, S. Samiei, Z. Xu, and J. H. Masliyah, "Effect of particle size on the rheology of athabasca clay suspensions," *The Canadian Journal of Chemical Engineering*, vol. 87, no. 3, pp. 422–434, 2009. DOI: https://doi.org/10.1002/cjce.20168.

[88] C. W. Macosko. John Wiley & Sons, 1994, p. 96, ISBN: 978-0-471-18575-8. [Online]. Available: https://app.knovel.com/hotlink/toc/id:kpRPMA0004/rheology-principles-measurements/rheology-principles-measurements.

[89] G. Brito, O. Jerez, and L. Gutierrez, "Incorporation of rheological characterization in grinding and tailings slurries to optimize the cmp magnetic separation plant," *Minerals*, vol. 11, no. 4, 2021, ISSN: 2075-163X. DOI: 10.3390/min11040386.

[90] D. Fam, J. Dodds, and O. Scrivener, "Rheology and flow of phosphate slurries (mine tailings) in pipes," *Chemical Engineering & Technology*, vol. 10, no. 1, pp. 305–311, 1987. DOI: https://doi.org/10.1002/ceat.270100137.

[91] L. Zhang, H. Wang, A. Wu, B. Klein, and X. Zhang, "A constitutive model for thixotropic cemented tailings backfill pastes," *J. Non-Newtonian Fluid Mech.*, vol. 295, p. 104 548, 2021, ISSN: 0377-0257. DOI: https://doi.org/10.1016/j.jnnfm.2021.104548.

[92] M. Syamlal and T. J. O'Brien, "Computer simulation of bubbles in a fluidized bed," in *AIChE Symp. Ser*, Publ by AIChE, vol. 85, 1989, pp. 22–31.

[93] C. Lun, S. B. Savage, D. Jeffrey, and N Chepurniy, "Kinetic theories for granular flow: Inelastic particles in couette flow and slightly inelastic particles in a general flowfield," *Journal of fluid mechanics*, vol. 140, pp. 223–256, 1984. DOI: https://doi.org/10.1017/S0022112084000586.

[94] J. T. Bulmer and T. e. Starr, "Syncrude analytical methods for oil sand and bitumen processing," p. 173, 1979.

[95] R. Maron, M. Fernald, D. Christian, O Keefe, J. Viega, and T. Bailey, "New applications of sonar-based technology in the minerals processing industry: Velocity profile measurement and pipe wall wear monitoring in hydrotransport lines," 2008.

[96] H. J. Ilgner, "Novel instrumentation for online monitoring of stationary beds and their height for settling slurries," ser. North American Conference on Multiphase Production Technology, BHR-2016-117, vol. All Days, Jun. 2016. [Online]. Available: https://onepetro.org/BHRNACMT/proceedings-pdf/BHR16/All-BHR16/BHR-2016-117/1330511/bhr-2016-117.pdf.

[97] C. o'Keefe, R. Maron, M. Fernald, T. Bailey, A. van der Spek, and D. Michael, "New developments in flow and pipe management capabilities through new velocity profile measurement and pipe wall wear monitoring instrumentation," 2009. [Online]. Available: www.CiDRA.com,resourcecentre,BI0359-2009..

[98] F. Picano, W.-P. Breugem, and L. Brandt, "Turbulent channel flow of dense suspensions of neutrally buoyant spheres," *J. Fluid Mech.*, vol. 764, pp. 463–487, 2015.

[99] T. N. Ofei and A. Y. Ismail, "Eulerian-Eulerian simulation of particle-liquid slurry flow in horizontal pipe," *J. Pet. Eng.*, vol. 2016, 2016.

[100] R. G. Gillies, "Pipeline flow of coarse particle slurries," Ph.D. dissertation, University of Saskatchewan, SK, 1993.

[101] M. Li et al., "Analysis of minimum specific energy consumption and optimal transport concentration of slurry pipeline transport systems," *Particuology*, vol. 66, pp. 38–47, 2021.

[102] B. Pang, S. Wang, G. Liu, X. Jiang, H. Lu, and Z. Li, "Numerical prediction of flow behavior of cuttings carried by herschel-bulkley fluids in horizontal well using kinetic theory of granular flow," *Powder Technol.*, vol. 329, pp. 386–398, 2018.

[103] L. Schiller and Z. Naumann, "A drag coefficient correlation," *Zeit. Ver. Deutsch. Ing.*, vol. 77, pp. 318–320, 1933.

[104] S. A. Morsi and A. J. Alexander, "An investigation of particle trajectories in two-phase flow systems," *Journal of Fluid Mechanics*, vol. 55, no. 2, 193–208, 1972. DOI: https://doi.org/10.1017/S0022112072001806.

[105] N. I. Kolev, *Multiphase Flow Dynamics 2*. Springer Berlin, Heidelberg, 2005. DOI: https://doi.org/10.1007/3-540-69835-3.

[106] M Ishii, "Two-fluid model for two-phase flow," 1987.

[107] T. Takamasa and A. Tomiyama, "Three-dimensional gas-liquid two-phase bubbly flow in a c-shaped tube," 1999.

[108] K Malysa, S Ng, J Czarnecki, and J Masliyah, "A method of visualization and characterization of aggregate flow inside a separation vessel, part 1. size, shape and rise velocity of the aggregates," *International Journal of Mineral Processing*, vol. 55, no. 3, pp. 171–188, 1999, ISSN: 0301-7516. DOI: https://doi.org/10.1016/S0301-7516(98)00031-3.

[109] K Malysa, S Ng, l Cymbalisty, J Czarnecki, and J Masliyah, "A method of visualization and characterization of aggregate flow inside a separation vessel, part 2. composition of the bitumen–air aggregates," *International Journal of Mineral Processing*, vol. 55, no. 3, pp. 189–202, 1999, ISSN: 0301-7516. DOI: https://doi.org/10.1016/S0301-7516(98)00032-5.

[110] D. Kaushal and Y. Tomita, "Solids concentration profiles and pressure drop in pipeline flow of multisized particulate slurries," *Int. J. Multiphase Flow*, vol. 28, no. 10, pp. 1697–1717, 2002.

[111] M.-z. Li, Y.-p. He, Y.-d. Liu, and C. Huang, "Hydrodynamic simulation of multi-sized high concentration slurry transport in pipelines," *Ocean Engineering*, vol. 163, pp. 691–705, 2018, ISSN: 0029-8018. DOI: https://doi.org/10.1016/j.oceaneng.2018.06.046.

[112] M. K. Gopaliya and D. R. Kaushal, "Analysis of effect of grain size on various parameters of slurry flow through pipeline using cfd," *Particulate Science and Technology*, vol. 33, no. 4, pp. 369–384, 2015. DOI: https://doi.org/10.1080/02726351.2014.971988.

[113] M. K. Gopaliya and D. Kaushal, "Modeling of sand-water slurry flow through horizontal pipe using CFD," *J. Hydrol. Hydromech.*, vol. 64, no. 3, p. 261, 2016.

[114] P. Doron, M. Simkhis, and D. Barnea, "Flow of solid-liquid mixtures in inclined pipes," *International Journal of Multiphase Flow*, vol. 23, no. 2, pp. 313–323, 1997, ISSN: 0301-9322. DOI: https://doi.org/10.1016/S0301-9322(97)80946-9.

[115] M. Kesely, V. Matousek, and P. Vlasák, "Settling slurry flow near deposition velocity in inclined pipe of negative slope," *EPJ Web Conf.*, vol. 213, p. 02 040, 2019. DOI: https://doi.org/10.1051/epjconf/201921302040.

Appendix A: Supporting Information

A.1 Validation of the model for Newtonian carrier fluid

The model was also validated with a Newtonian carrier fluid, to evaluate the performance of the model. To this end, the experimental measurements of the radial solid concentration distribution were extracted from the work by Gillies et al. [16]. Figure A.1 shows the comparison between the CFD-predicted solid concentration distribution and experimental measurements. The results show satisfactory agreement between the CFD predictions and the experimental data.

A.2 Effect of the drag force between the solid phases on the pressure drop of bimodal cases

In the main text, it was mentioned that the drag force between the solid phases in the cases with bimodal particles has a minimal effect on the pressure drop. This statement is based on the simulation of the cases with and without considering the drag force between two solid phases. The flow conditions of the simulated cases are based on the experiments in Test 21 and Test 22 of the work by Kesely [1]. Figure

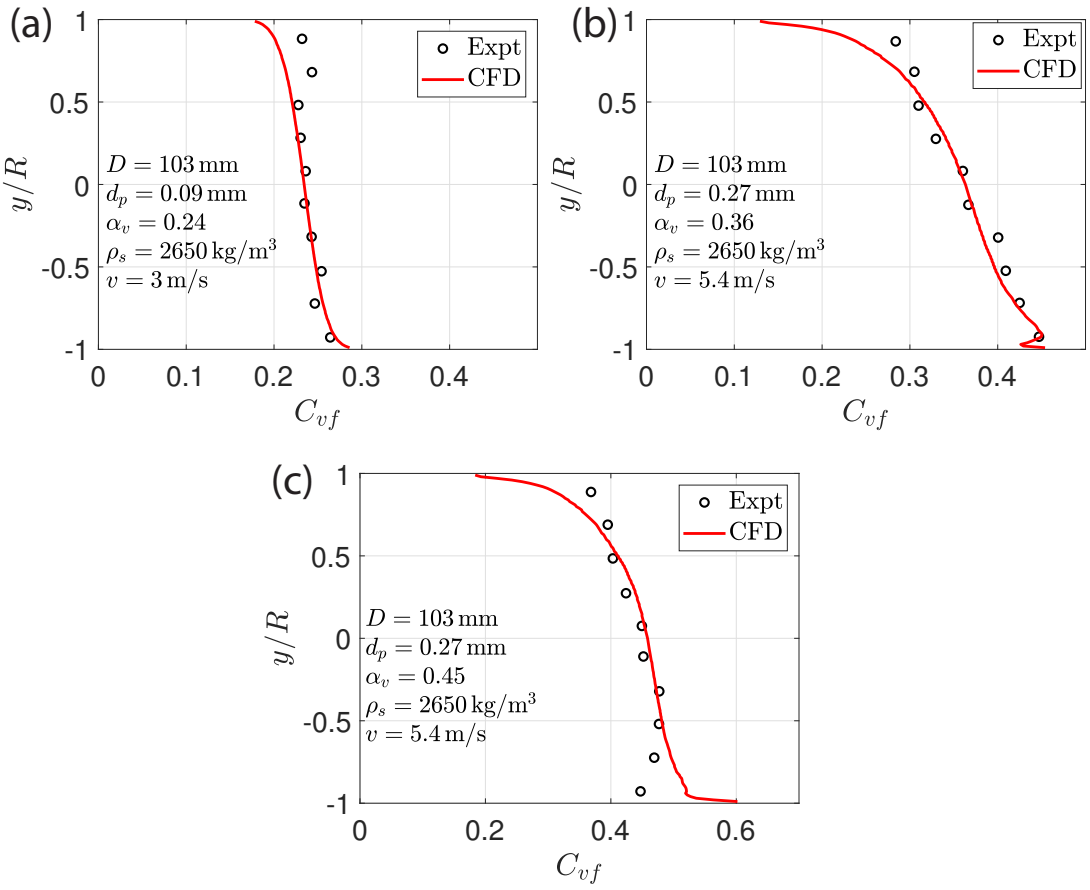

Figure A.1: Comparison of chord-averaged solids concentration of CFD (solid curve) results with experiment data (circles) for different flow conditions (a) $\alpha_v = 0.24$, $d_p = 0.09\,\text{mm}$, v = 3 m/s(b) $\alpha_v = 0.36$, $d_p = 0.27\,\text{mm}$, v = 5.4 m/s and (c) $\alpha_v = 0.45$, $d_p = 0.27\,\text{mm}$, v = 5.4 m/s.

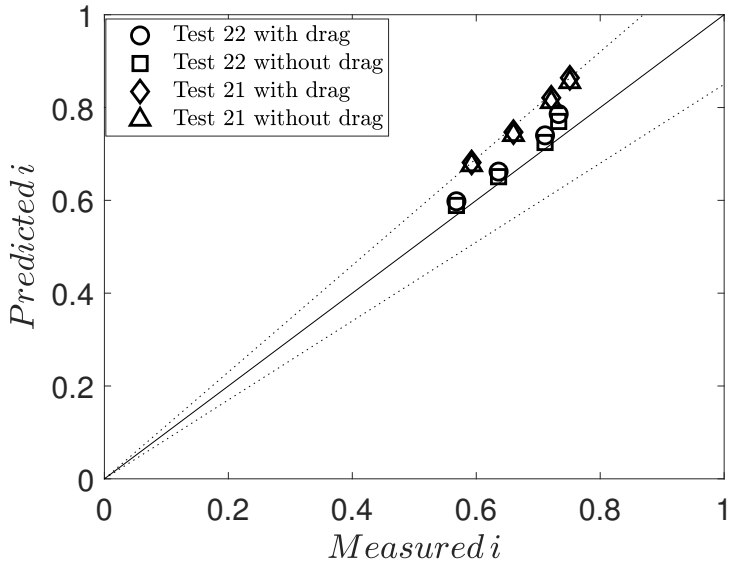

Figure A.2: Hydraulic gradient predicted by CFD for the bimodal cases with and without considering the drag force between the two solid phases vs. experimental measurements of Kesely [1].

A.2 shows the comparison between the CFD-predicted hydraulic gradient of two-phase slurries with bimodal particles and the experimental measurements. For each data point, two simulation cases were prepared and solved, one with enabling the drag force, and one with neglecting the drag force between two solid phases. The results show that for each data point, the hydraulic gradients predicted by CFD are approximately equal for the two cases with and without drag force, proving the insignificant effect of the drag force between the solid phases on pressure drop.

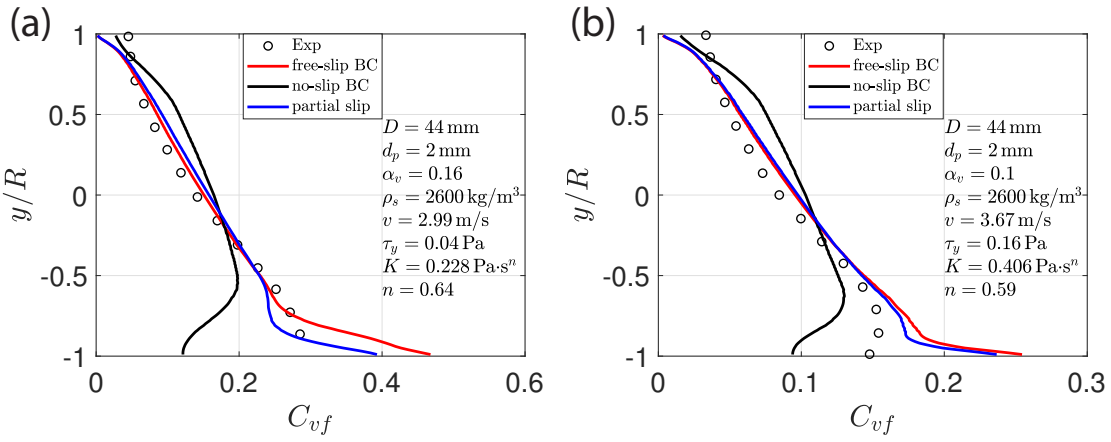

Figure A.3: Comparison of chord-averaged solids concentration of CFD results with different wall boundary conditions with experiment data (circles) for different flow conditions (a) $D = 44.0\,\text{mm}, d_p = 2\,\text{mm}, \rho_s = 2600\,\text{kg/m}^3, v_m = 2.99\,\text{m/s}, \tau_y = 0.04\,\text{Pa}, K = 0.228\,\text{Pa.s}^\text{n}, n = 0.64$ (b) $D = 44.0\,\text{mm}, d_p = 2\,\text{mm}, \rho_s = 2600\,\text{kg/m}^3, v_m = 3.67\,\text{m/s}, \tau_y = 0.16\,\text{Pa}, K = 0.406\,\text{Pa.s}^\text{n}, n = 0.59$.

A.3 Effect of solids phase wall boundary condition on the performance of the Eulerian–Eulerian model

As mentioned in the main text, the free-slip boundary condition was used for the solids phase in all of the simulations. This choice was based on the investigation of the performance of no-slip, partial-slip, and free-slip boundary conditions in the prediction of the solids concentration distribution for the cases in the validation section. The accurate prediction of the pressure drop was also considered. Fig. A.3 shows the comparison of the CFD predicted solids concentration distribution with different wall boundary conditions with the experimental measurements performed by Zheng et al. [7]. The simulations with partial-slip boundary conditions were done by assuming the value of the wall shear stress to be half of the maximum shear

stress which happens with the no-slip boundary condition. The results show that the free-slip boundary condition provides a better overall agreement between the CFD predictions and experimental data.

A.4 Comparison of first and second-order schemes in the mixture model

In Chapter 4, some first-order discretization schemes have been used for the numerical solution of the equation as mentioned in Table 2.6 such as first-order upwind for momentum, volume fraction, turbulent kinetic energy, and specific dissipation rate. The investigations conducted on the velocity distributions and pressure gradient indicated that in this study, there is no noticeable effect of numerical diffusion made by the first-order schemes compared to the results of the second-order schemes. Fig. A.4 shows the velocity distributions predicted by CFD with first and second-order discretization schemes for three representative cases compared with the field data. As shown in this figure, there is no significant difference between the results, and for most data points, the values are the same and the symbols overlap. Table A.1 presents the pressure gradient predicted by CFD with first and second-order discretization schemes for the same representative cases. As the values indicate, the choice of first or second-order schemes makes no noticeable changes in the CFD results, as for two cases the values are equal with two digits and for one case (Case 2), only 0.01 of difference is observed. Considering that first-order schemes lead to faster and easier convergence, and there is no difference between the result of first and second-order schemes, the selection of discretization schemes is justified for the results presented in Chapter 4.

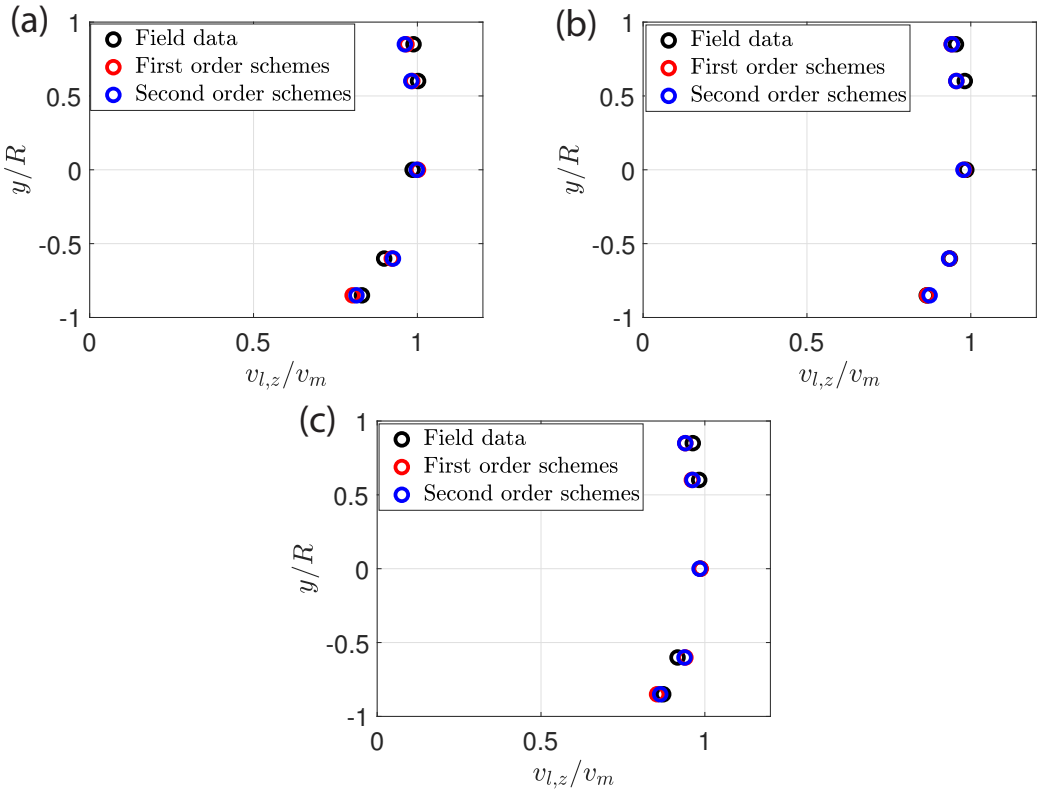

Figure A.4: Velocity distributions predicted by CFD with first and second order discretization schemes for three representative cases (a) Case 2, (b) Case 7, and (c) Case 8.

Table A.1: Pressure gradients predicted by CFD with first and second order discretization schemes for three representative cases

Case	ΔP/L predicted by 1^{st} order schemes (kPa/m)	ΔP/L predicted by 2^{nd} order schemes (kPa/m)
(2)	0.54	0.55
(7)	0.46	0.46
(8)	0.53	0.53

Appendix B: Mixture model package

B.1 Introduction

The behavior of multiphase flows can be studied and predicted accurately using the CFD technique. In the CFD package, the governing equations of the flow are solved numerically by the software, and the specifications of the flow conditions, the models, and the physics of the flow should be performed by the operator. This document presents a comprehensive step-by-step guide on the simulation of a three-phase oil sands tailings flow consisting of a non-Newtonian carrier fluid, coarse solid particles (particles larger than 44 µm in size), and bitumen droplets. The model is established and already validated against experimental measurements and has shown good accordance with the experimental data. Therefore, the predictions made by the model can be considered accurate, if the changes in the flow conditions or parameters are not dramatic, e.g., a huge change in the rheological properties of the carrier.

Using the provided document, the operator can develop and modify the model and flow conditions to study the effect of the flow parameters, or predict the key aspects of the flow. For example, the effect of solids concentration on the flow, such as pressure drop, velocity distributions, etc. can be investigated quantitatively using

this model.

B.2 Ansys Fluent

The CFD studies are conducted via Ansys Fluent 2020 R2. Ansys Fluent is a commercial package, widely used for different flow studies. This software is highly efficient in the modeling and solution of the equations, also user-friendly, and easy to use. The version of the software to open the provided files should be the same (2020 R2) or higher, although having the same version is encouraged. A file exported from a higher version can not be opened in a lower version. The installation and activation of the software are quite straightforward. Once the software is installed and the license is activated, the case and data files can be imported.

- Case file: a file usually with a "cas.h5" type which contains the setup of a simulation. The model and its properties are stored in the case file
- Data file: A file where the simulation results are stored. The type of a data file is usually "dat.h5".

The Fluent Launcher window which appears first when the software is opened is shown in Figure B.1. The desired case and data files can be selected to be opened in this window, or just by hitting "Start" and then importing them into the Fluent environment. It is also possible to open the software and arranging the setup without importing a case file. The "Dimension" tab should always be kept as 3D while using this package as the pipe is designed in three dimensions. The "Parallel" tab is to specify the number of solvers to be used. This depends on the processing power of the computer the model is being run on. For example, if your computer CPU is

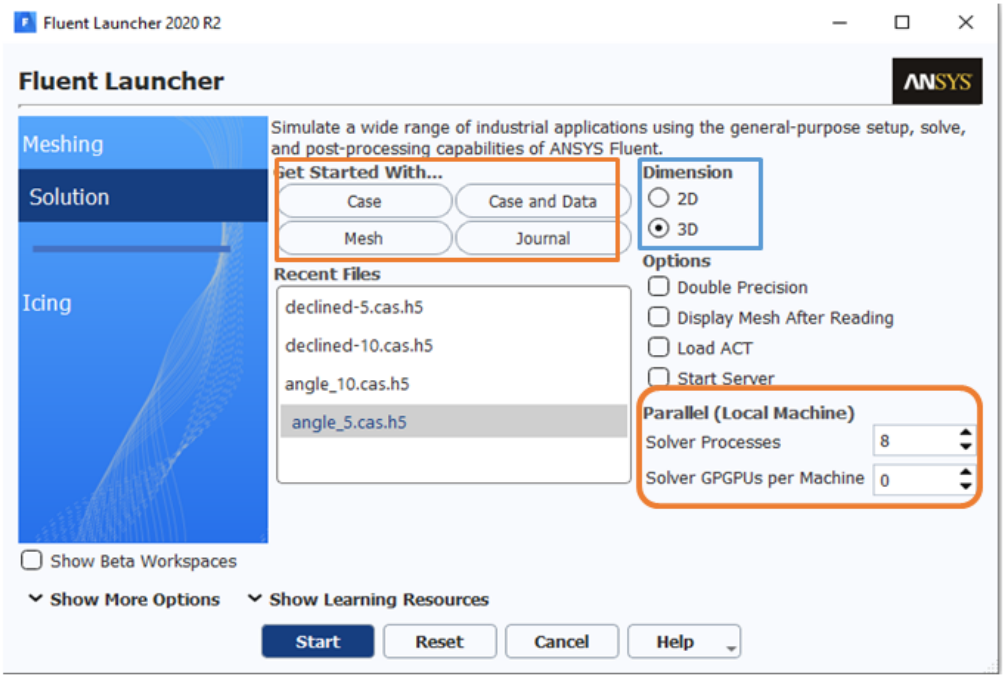

Figure B.1: Fluent launcher

built with eight cores, you can enter this number as the "Solver Processes". It is highly recommended to use this feature for running the simulation, as it can reduce the solution time significantly. By hitting "Start", the software will run, and the window shown in Figure B.2 appears.

In this interface, the case and data files have not been imported yet. The initial step is to read the case file (or case and data files if there is any data) if any file is available. To do this, do the following: File – Read – Case (or Case & Data) as shown in Figure B.3.

After choosing the type of file to be read, the browsing window will open, and go

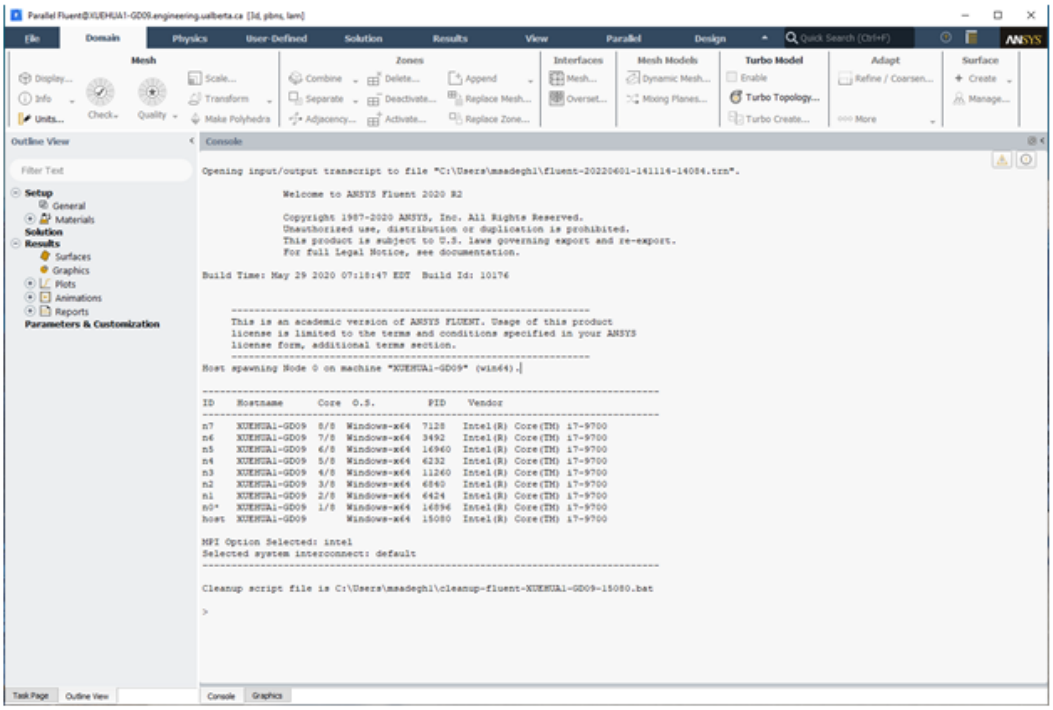

Figure B.2: Overview of the starting page of Fluent

to the directory where the case and data files are stored. Please note that the case and data files should have the same name, and while browsing, only the case file will appear and the data file will be read automatically. The appearance of the outline view where the simulation setup can be adjusted after reading the files is completed, is shown in Figure B.4.

B.3 Setup

The tabs in the outline view are described below:

General: The general setup such as the type of the simulation, the solver type,

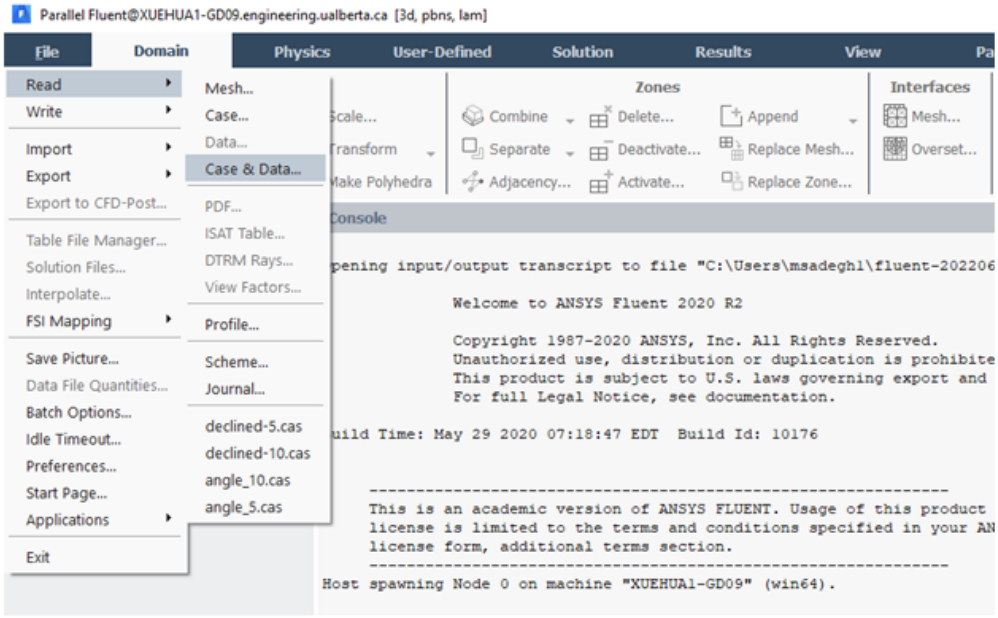

Figure B.3: Reading case and data files

etc. is specified in this tab. You should specify the steady-state or transient nature of the simulation in this tab.

The first step is to define the materials for the simulation as shown in Figure B.5. The materials are defined as fluids here. Air is defined by default, but its volume fraction in the boundary conditions will be set as zero. The physical properties of the materials are determined at a temperature of 50 °C. For the carrier fluid, the density is calculated from the experimental data of fines concentration in water, and the viscosity is defined by the Casson rheological model. As the Casson model is not available in the Ansys Fluent library, it should be added to the model as a User-Defined Function (UDF) as shown in Figure B.6.

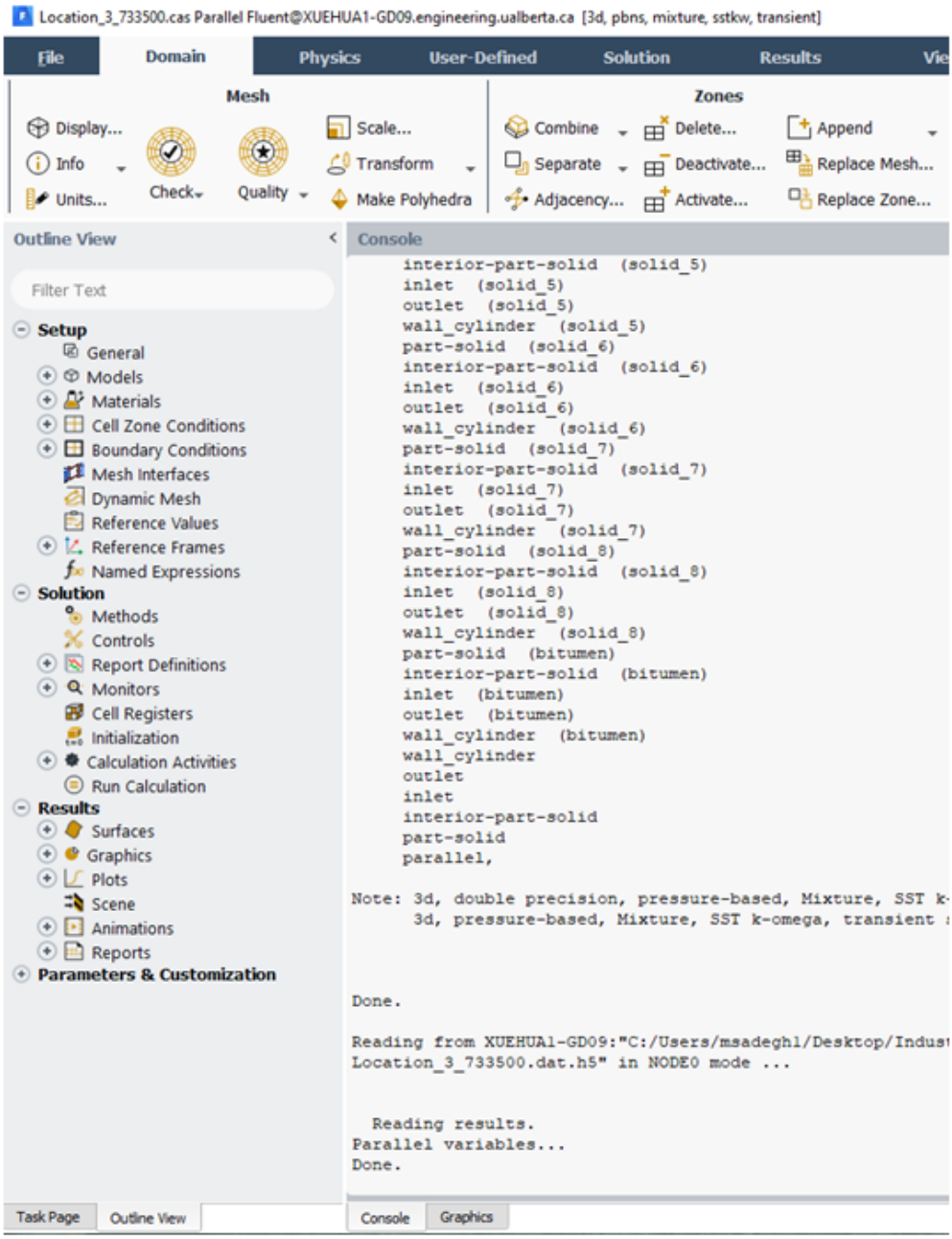

Figure B.4: Overview of Fluent after reading case and data

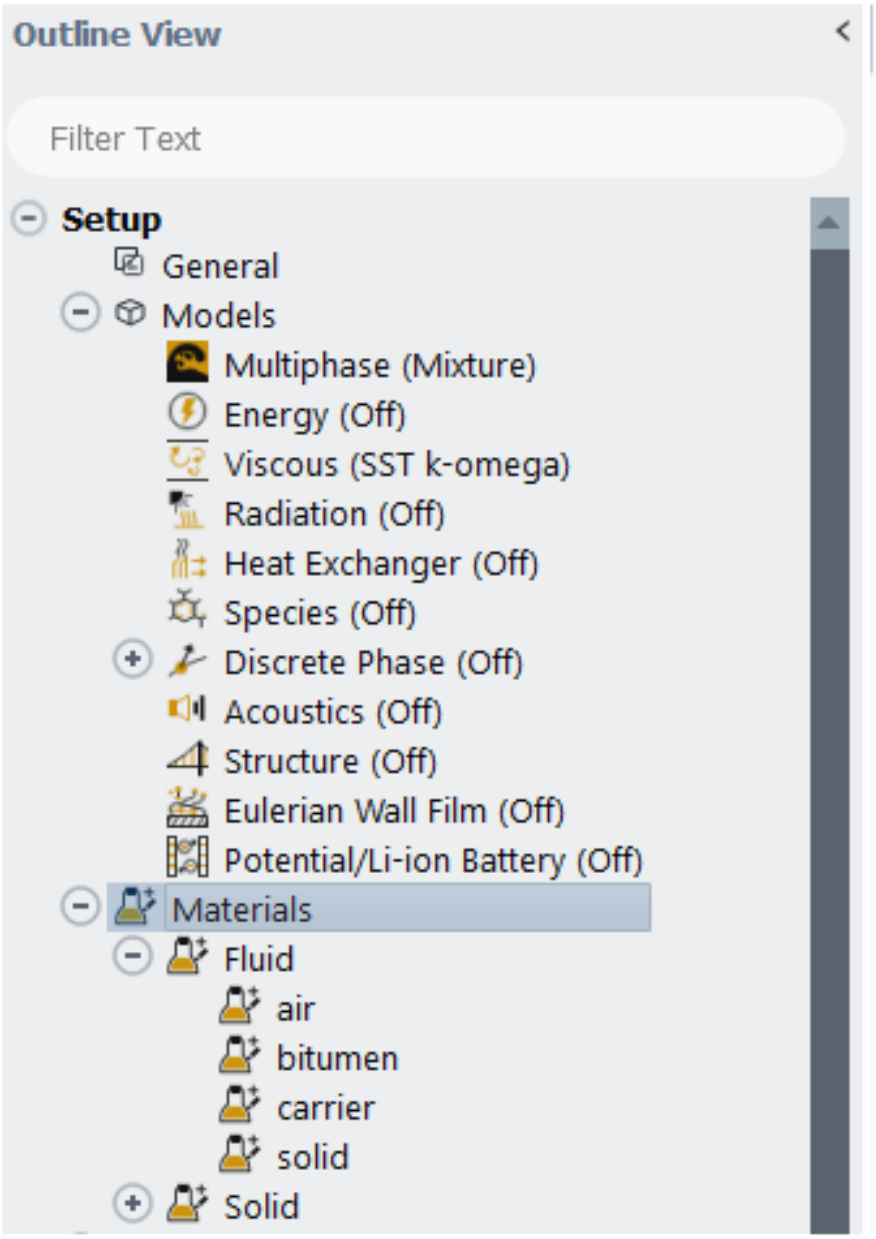

Figure B.5: The Materials tab in the outline view

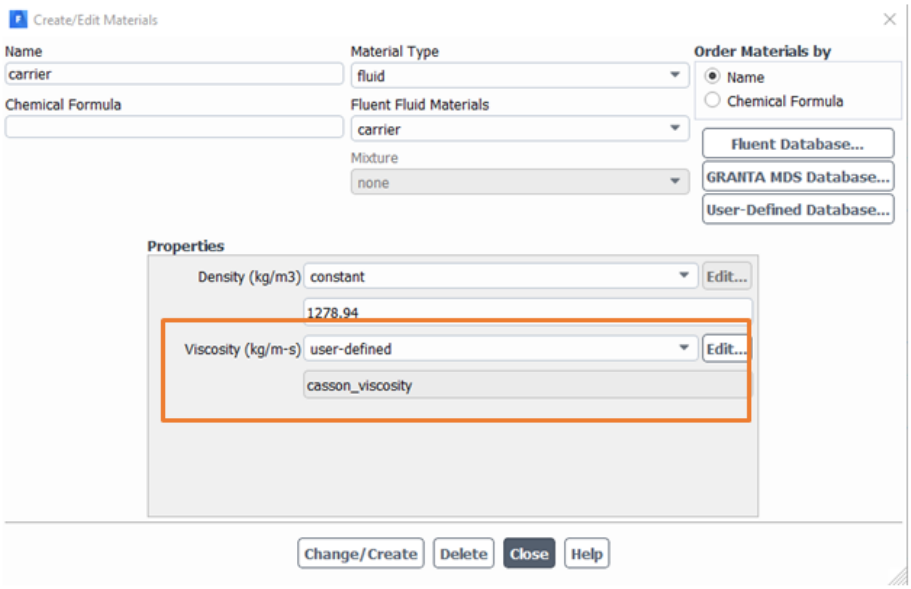

Figure B.6: The carrier fluid properties

To import a UDF into the model, go to User-Defined tab – Functions – Interpreted (Figure B.7). Then, a window will be opened to choose the UDF file. Remember to keep the UDF file in the same directory as the case and data files. After the interpretation process is completed, go to the materials tab again and open the carrier tab. In the viscosity part, choose user-defined, and then Casson viscosity.

Models: This is the main window in this simulation file. The models to describe the interactions and properties of the phases can be selected here. This tab contains multiple subsections as shown in Figure B.8:

Of the subsections of the "Models" tab, there are only two of them related to this simulation. In the "Viscous" subsection, the turbulence model is selected. The chosen model (SST k-ω) has shown high accuracy and efficiency in modeling the turbulent regime, so no changes are required. The "Multiphase" tab is where the

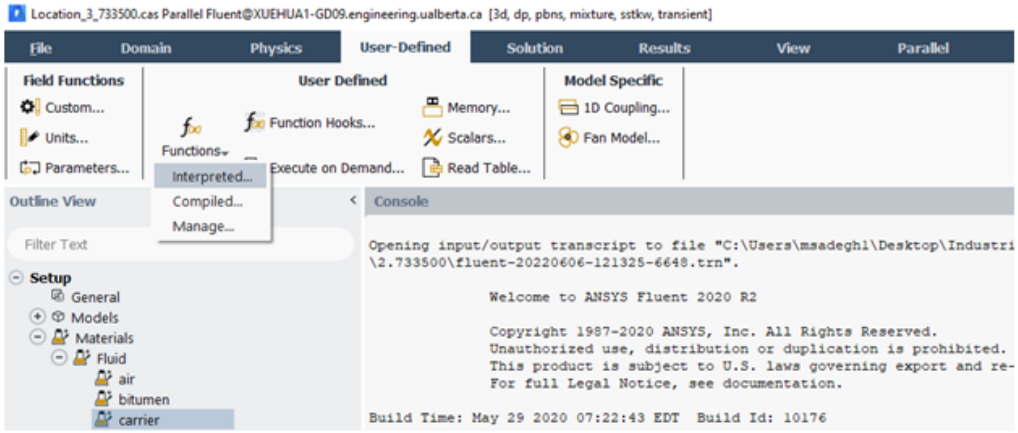

Figure B.7: Importing the UDF file for Casson viscosity

properties of the phases, interactions, and main features of the multiphase model are specified.

In the first window as shown in Figure B.9, the type of multiphase modeling is chosen which is the "mixture" model in this case. As highlighted in the picture, the number of phases is set at 10 in the initial cases. This comes from the polydisperse solid particles. Based on the PSD information, eight discrete sizes have been considered and added to the simulation as separate secondary phases. With the carrier fluid and bitumen as the two other phases, the system is made of ten phases in total. If any change in the number of solid sizes is desired, the number of phases should be changed accordingly. For example, if only d_{50} is to be considered (single-size particles), the number of phases should be changed to 3.

In the "Phases" window as shown in Figure B.10, the properties of the phases are specified. For the carrier fluid as the primary phase, the material is set as the carrier. The materials and their properties are defined in the "Materials" section in

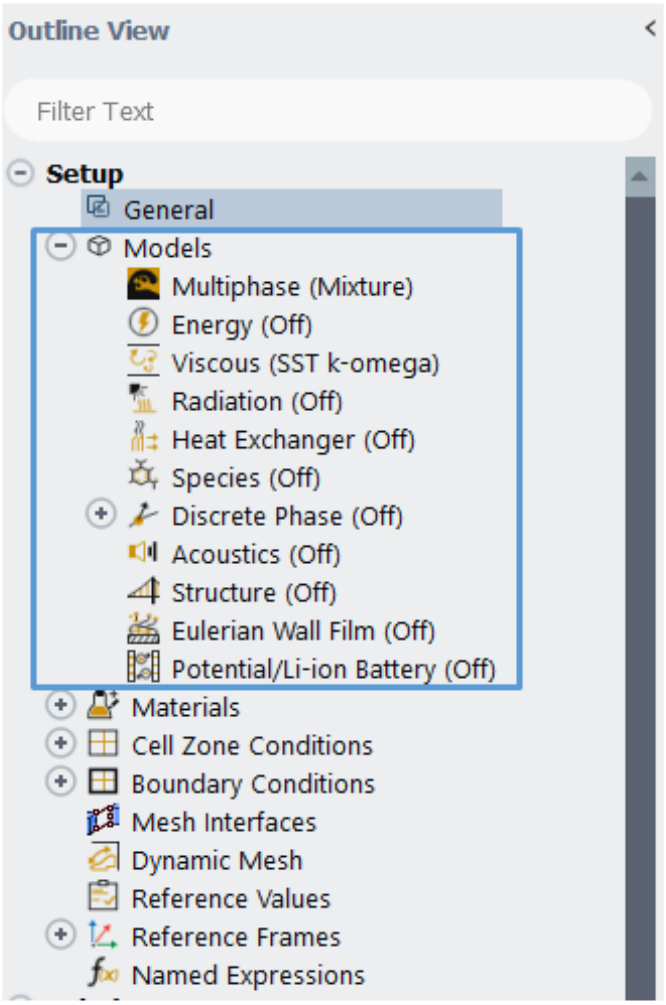

Figure B.8: The models' tab and its subsections

the outline view and will be explained later.

For the solid phases, the material is set as "solid". The particle sizes can also be specified in this tab. In the original simulation file, the sizes of solid particles in each

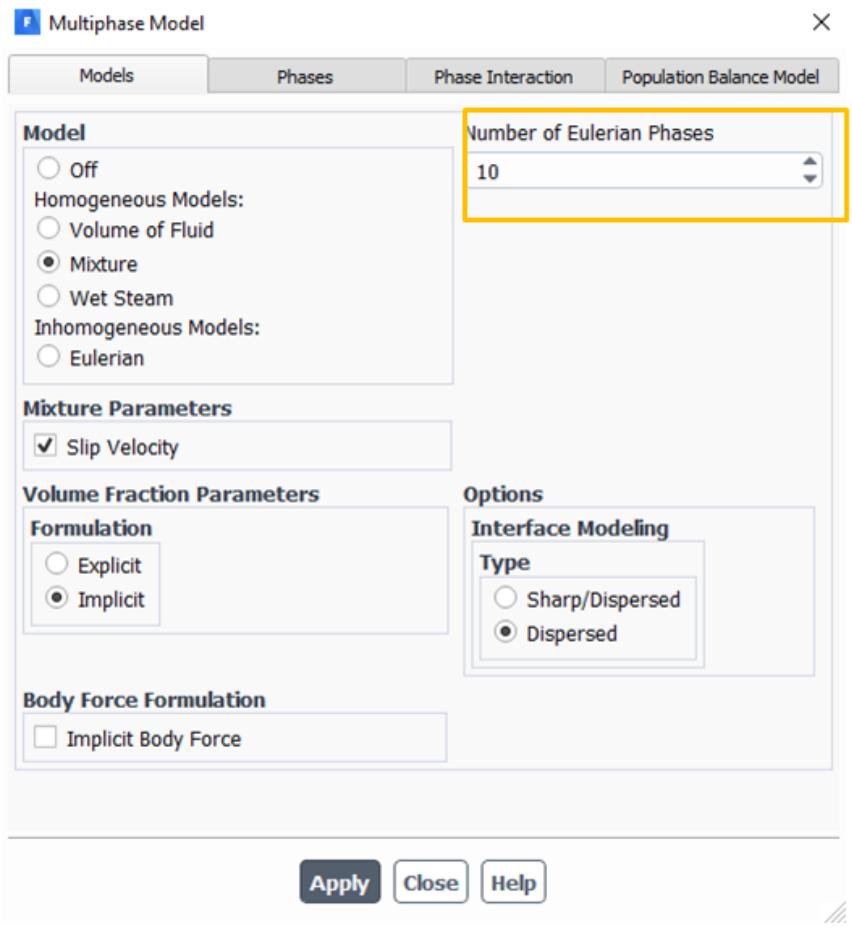

Figure B.9: The multiphase models' window

phase are shown in Table B.1. The solid sizes can be altered as desired.

The "Granular Properties" section is related to the granular kinetic theory which captures the effects of particle-particle interactions. The sub-models of the granular kinetic theory are explained in Chapter 2 of this thesis.

For the bitumen phase, the material is set as bitumen, and the diameter of the droplets is set as 400 µm, which can be altered as desired. Figure B.11 shows the

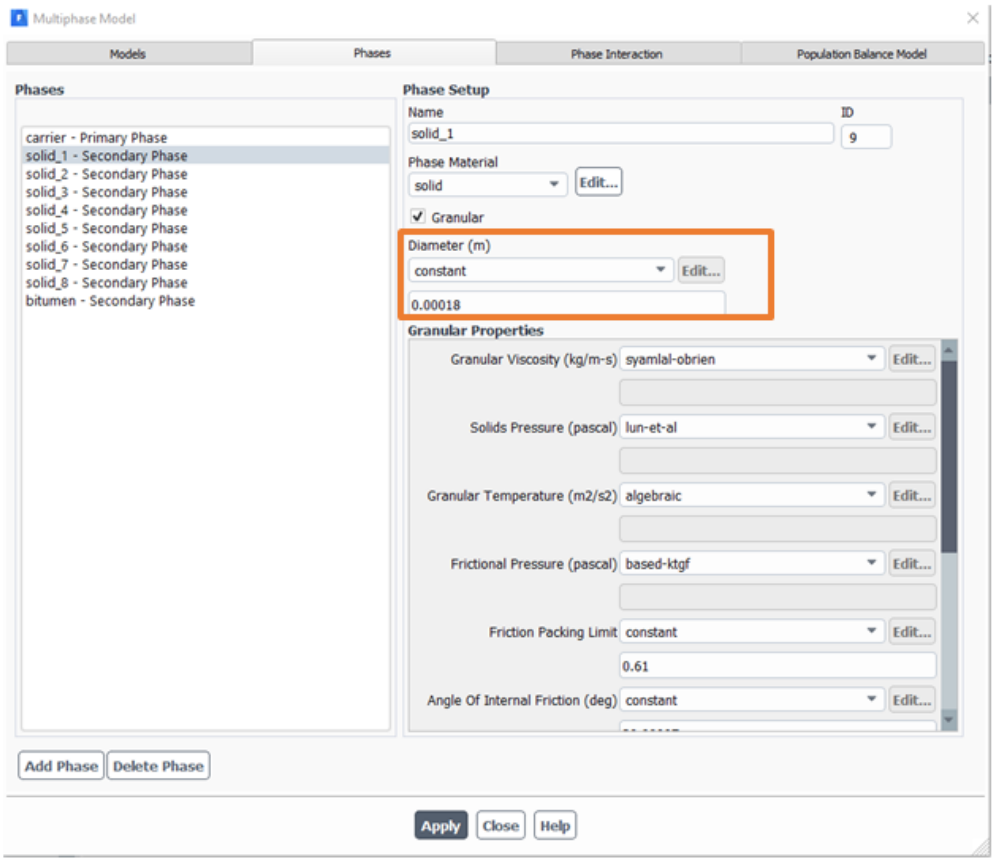

Figure B.10: Specification of the phases' properties

phase properties of bitumen.

In the "Phase Interaction" section, the setup of the mixture model which describes the momentum balance for the phases can be built. For each pair of phases, the closures for the drag coefficient and slip velocity can be selected.

Specification of the boundary conditions (BCs) is the next step for this simulation (Figure B.13). The value of velocity and volume fractions of the components should be specified at the inlet as shown in Figures B.14 & B.15.

Table B.1: The solid particles sizes

Solids	Size (μm)
solid 8	1000
solid 7	710
solid 6	500
solid 5	355
solid 4	250
solid 3	180
solid 2	125
solid 1	75

For outlet BC, the zero-gauge pressure at the outlet can be specified as shown in Figure B.16. This BC is only applied to the mixture and there is no need to put it for each phase separately.

And finally, for the wall BC, the slip condition of the mixture at the wall should be specified. No-slip, partial-slip, and free-slip conditions are the options and for this simulation, the no-slip BC is chosen for the mixture (Figure B.17).

In the next step in the methods tab, the discretization schemes for the numerical solution should be specified as shown in Figure B.18. These methods determine how the equation for each parameter is being converted to an algebraic relation with different levels of accuracy and computation cost. It is recommended to use the methods previously mentioned in this thesis, as they have been tested and their suitability has been approved.

In the "Controls" tab (Figure B.19), the values for under-relaxation factors can

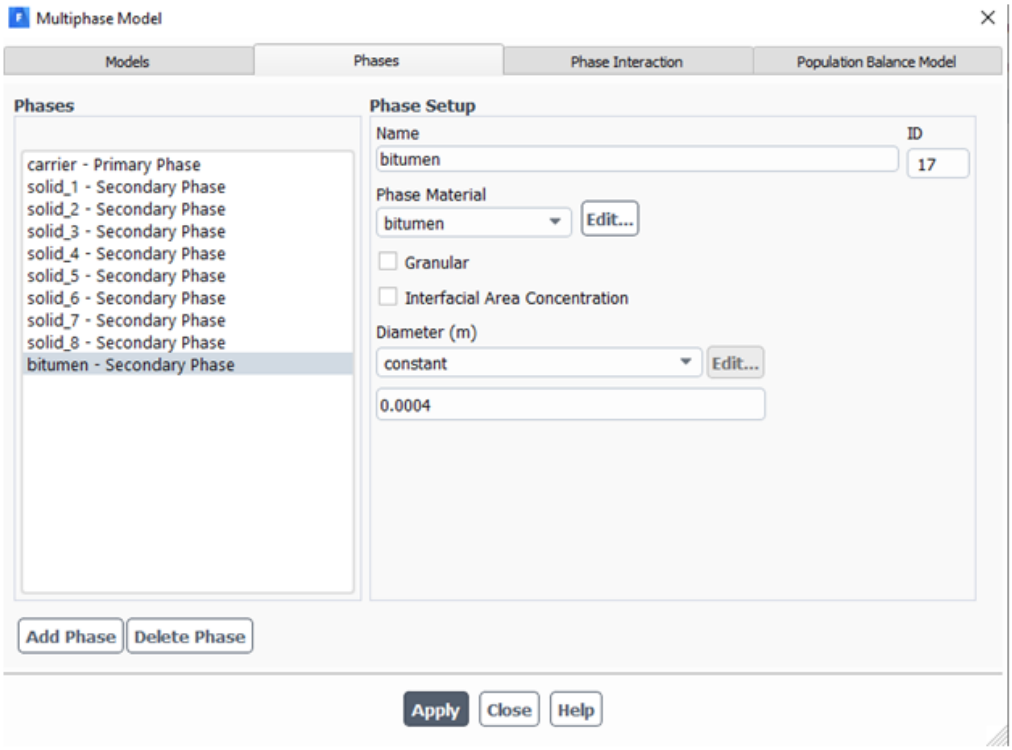

Figure B.11: Bitumen phase properties

be adjusted as required. Some default values have been set in Ansys Fluent for each factor, and they are appropriate most of the time. However, if any difficulties in terms of convergence occur, these factors may be reduced or changed to enhance the numerical stability. For the case and data provided here, the values can be kept the same.

The last step for a transient simulation before starting the solution process is the initialization. In this step, the values of each parameter in the entire domain at time zero should be specified as shown in Figure B.20. Initialization is one of the most important steps in any transient simulation and can influence the convergence and

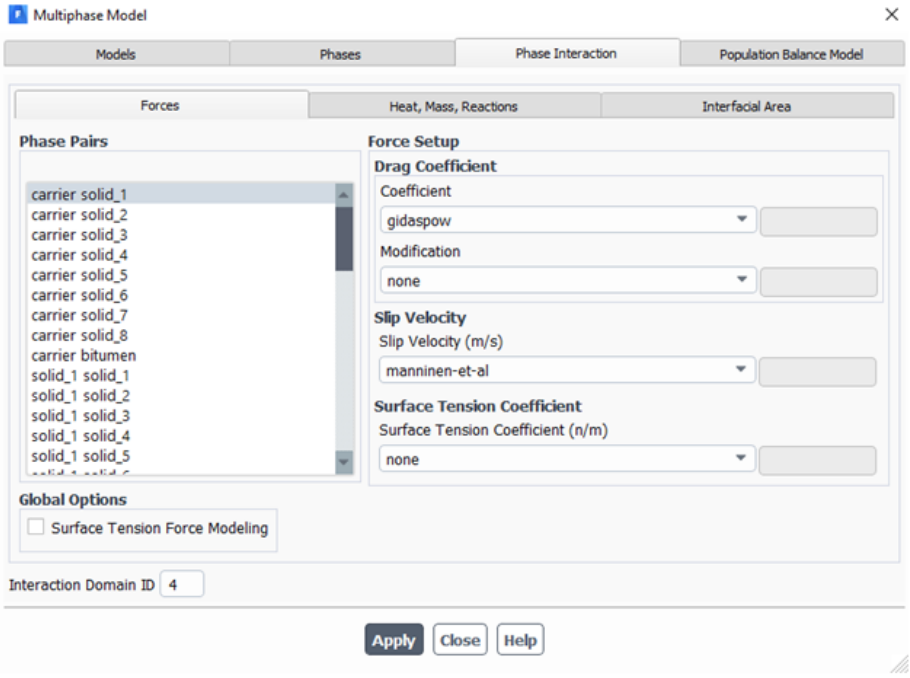

Figure B.12: Specification of the phases' interactions

solution time significantly. When a data file is imported along with a case file, if any changes are made or without changes, if the simulation is about to be continued for more time steps, Fluent will use the previously solved data as the initial condition and there is no need for the manual initialization. So, if the case and data files are read together, just change the simulation setup as desired and continue the simulation. If for any reason, the data file is not imported or a new initialization is required, the best way is to initialize the values from the inlet.

Ansys Fluent has the ability to save a case and data file while running a simulation with a frequency of the time step as specified. This is especially useful when the number of time steps is high, or the evolution of the solution with time is required

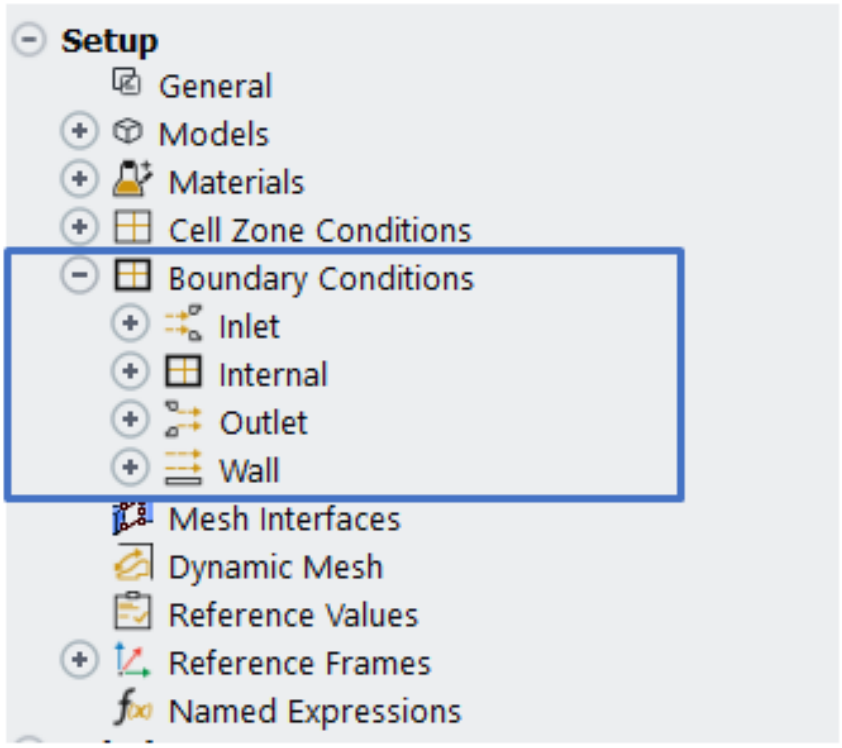

Figure B.13: The boundary conditions tab in the outline view

to be investigated. To do this, go to the "Calculation activities – Autosave (shown in Figure B.21). Specify the number of time steps you want to save the files and the name of the files, and select a directory for storing the files.

B.4 Solution

In the end, the number of time steps, time step size, and the number of iterations at each time step should be specified as shown in Figure B.22. Please note that the

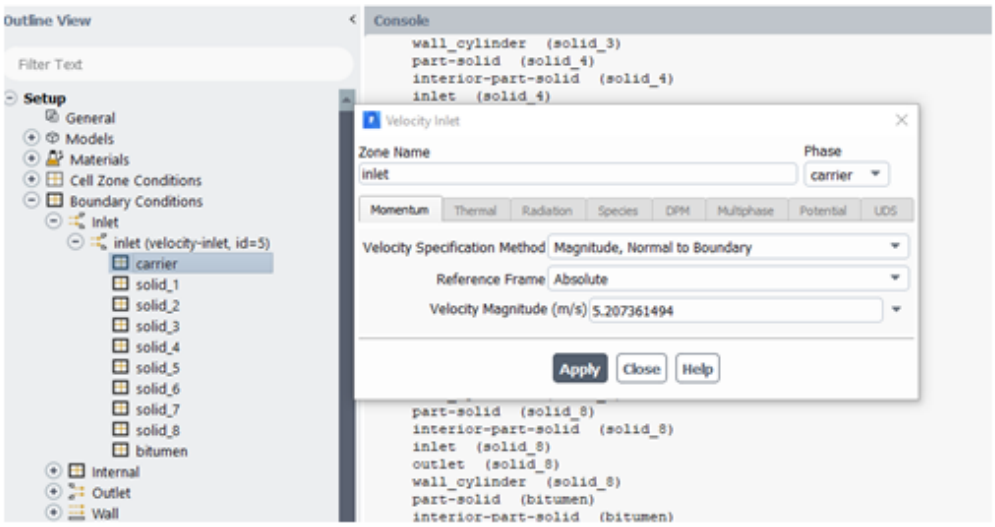

Figure B.14: Specifying the inlet BC

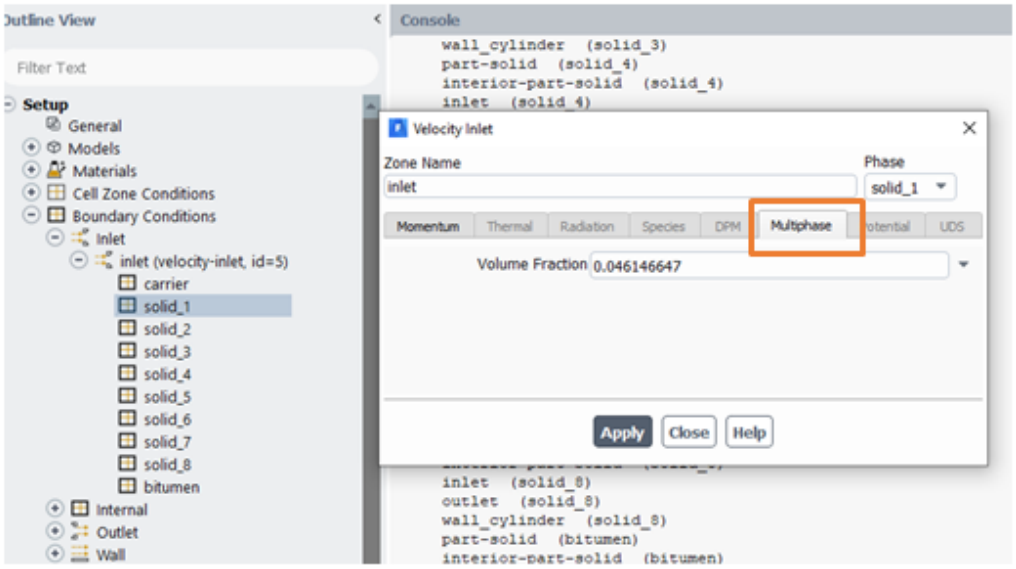

Figure B.15: Specifying the volume fractions at the inlet

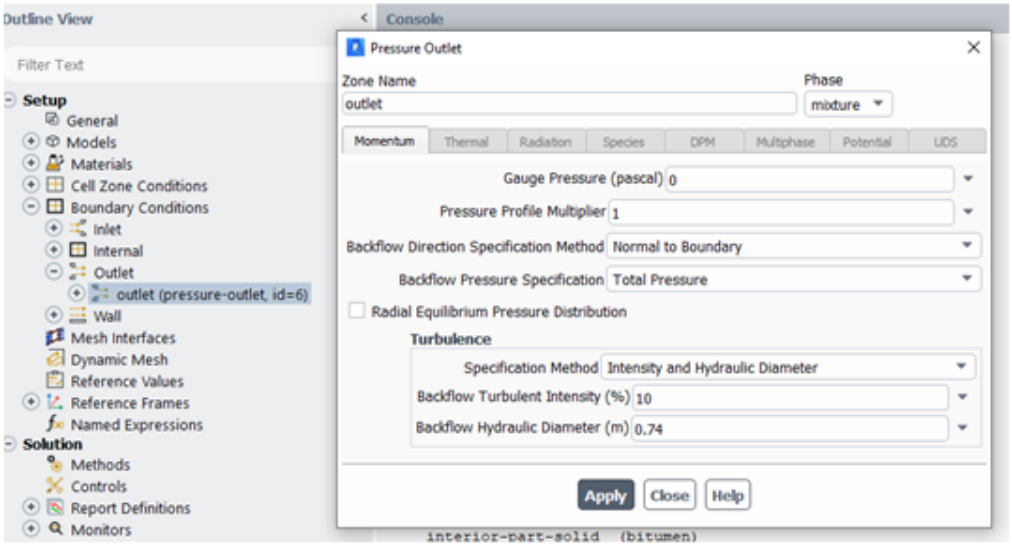

Figure B.16: Specifying the outlet BC

criteria for convergence for each parameter have been set to a residual value less than 10^{-4}. This criterion leads to acceptable accuracy and a relatively short time for convergence and completion of the simulation.

By clicking on "Calculate", the solution process starts. The progress of the simulation can be monitored by the values of residuals. The simulation can be stopped after an arbitrary number of iterations. To achieve reliable results, it is strongly recommended to let the simulation run completely.

B.5 Post–processing the results

Once the simulation is completed, the results can be post-processed and different types of figures, contours, and quantities can be extracted. CFD-post is an application from Ansys which can be used for post-processing. The results from Fluent

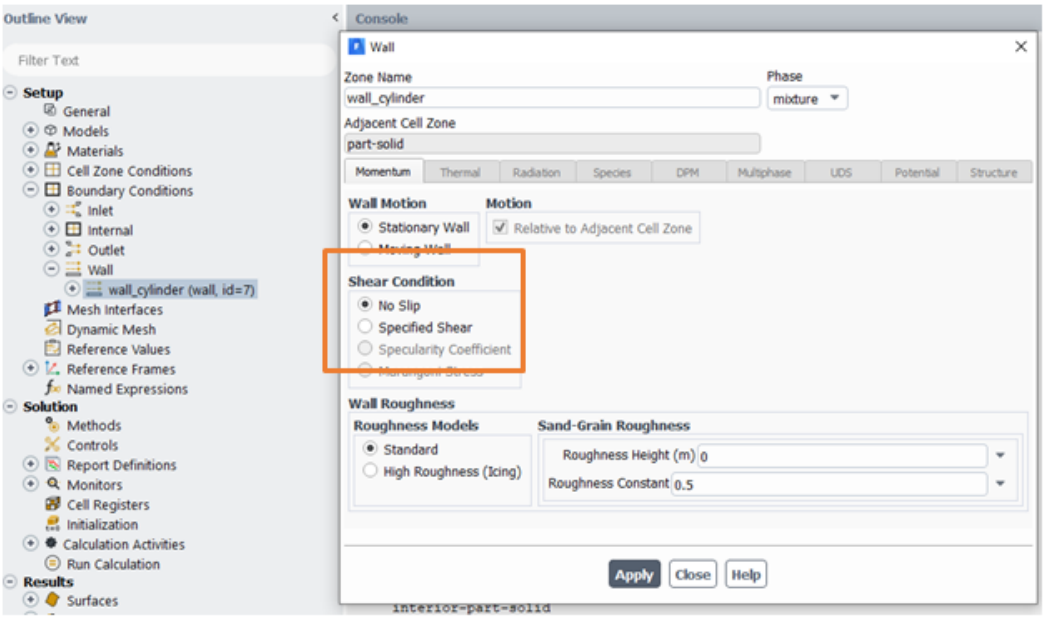

Figure B.17: Specifying the wall BC

can be directly sent to CFD-post. The post-processing procedure can also be done in Fluent itself, as it offers different types of operations on the raw data like drawing plots, getting surface or volume integrals, different types of averaging, etc.

The overview of the "Results" tab in Fluent is shown is Figure B.23. Here the calculation and visualization of some of the important parameters such as pressure drop, velocity, and concentration distributions in Ansys Fluent are explained. To calculate the pressure drop between two arbitrary locations, the area-averaged pressure on the planes should be calculated. To do this, go to Results – Surface Integrals (shown in Figure B.24). In the report type, "Area-Weighted Average" must be selected. The variable can be selected as static pressure or total pressure. And finally, the surfaces where the pressure is going to be calculated should be selected. The

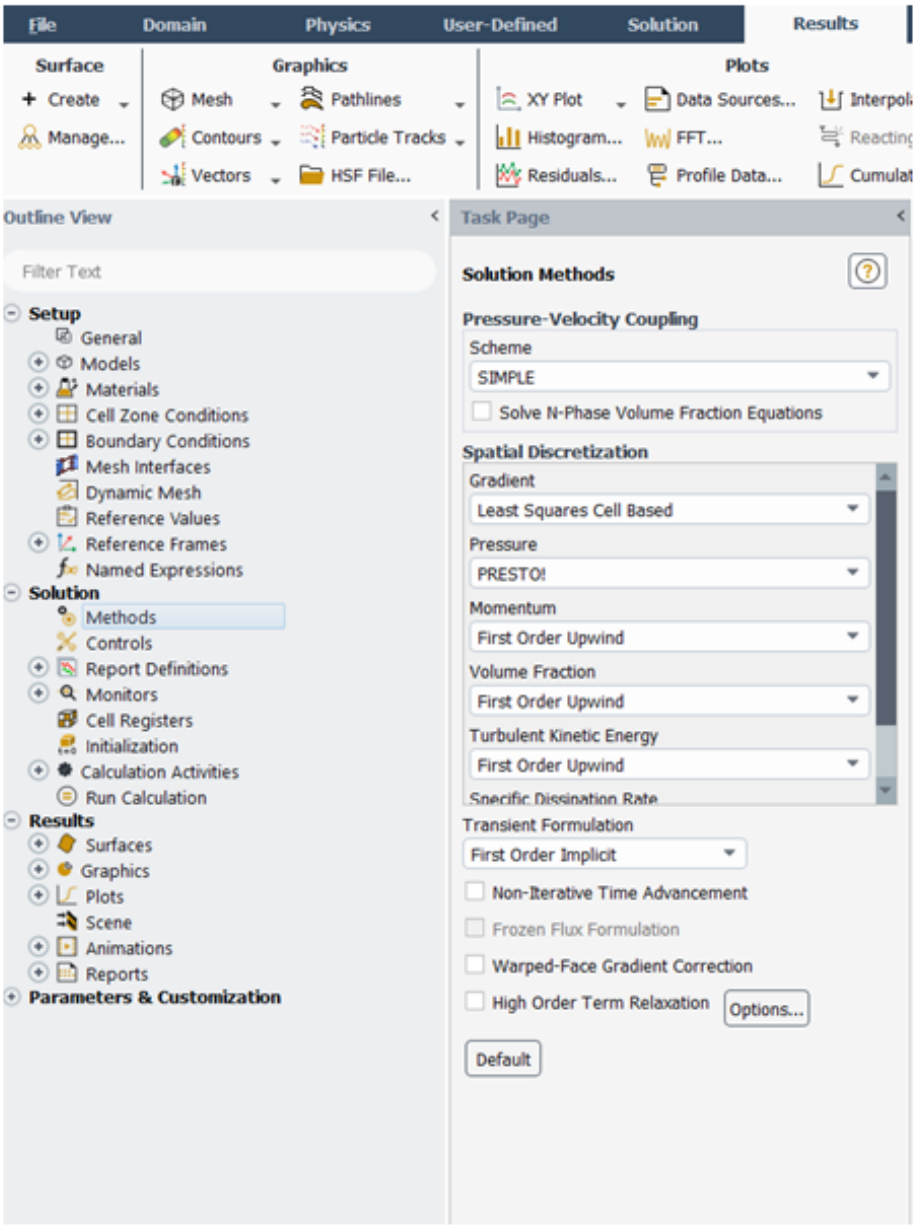

Figure B.18: The discretization methods

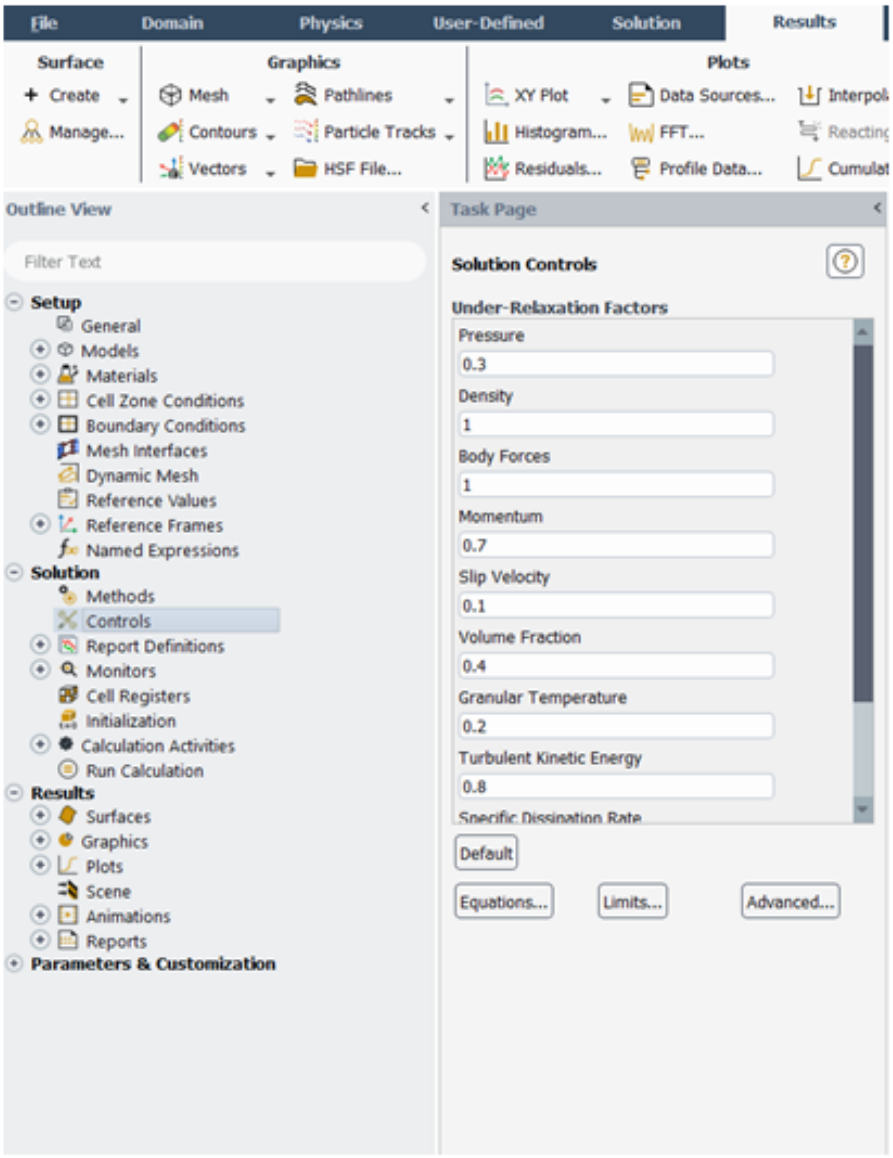

Figure B.19: The values of under-relaxation factors

available options available in the prepared case file are at 50, 90, and 100 m distance from the inlet. If any other distance is required, a new plane should be generated.

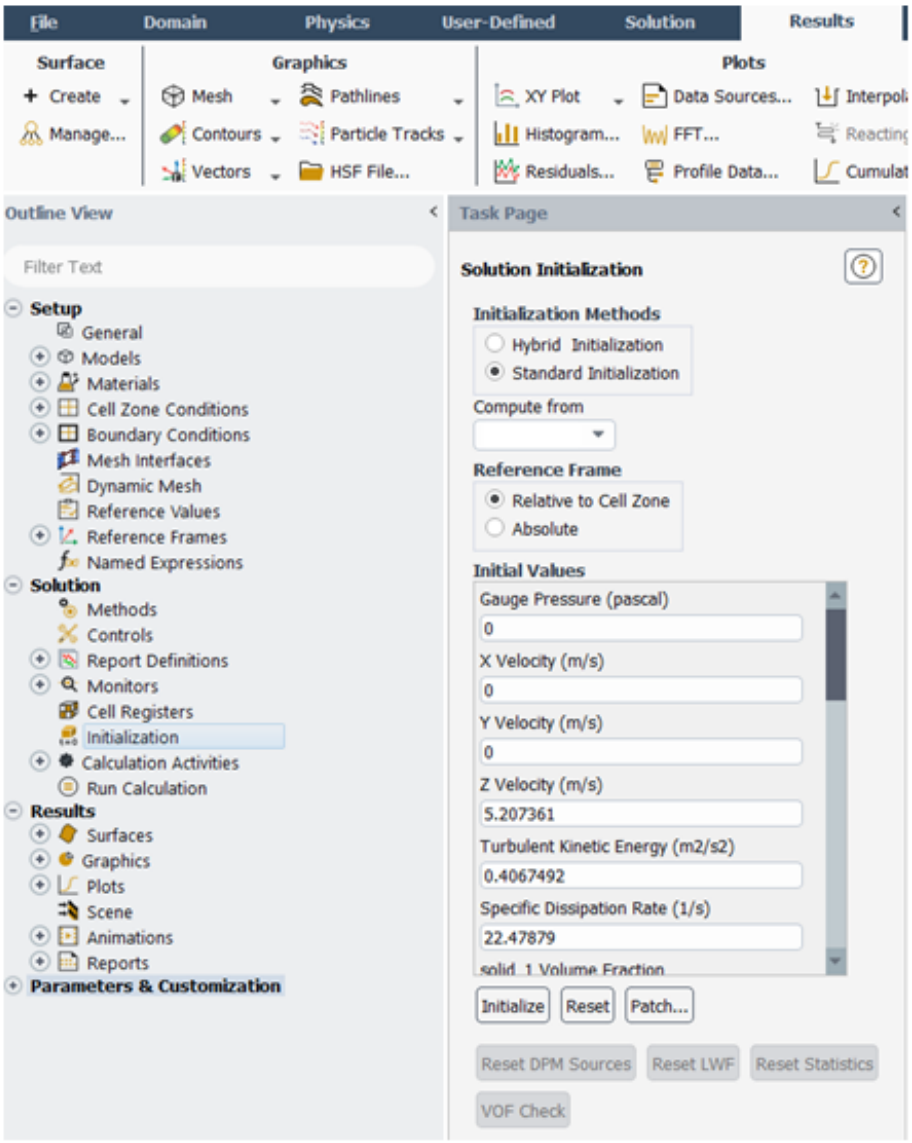

Figure B.20: The initialization tab

Once the planes are selected, click on "Compute", and the values will be printed in the Console. To calculate the pressure gradient, use the difference in the pressures at the inlet and outlet divided by the length of the pipe (105 m).

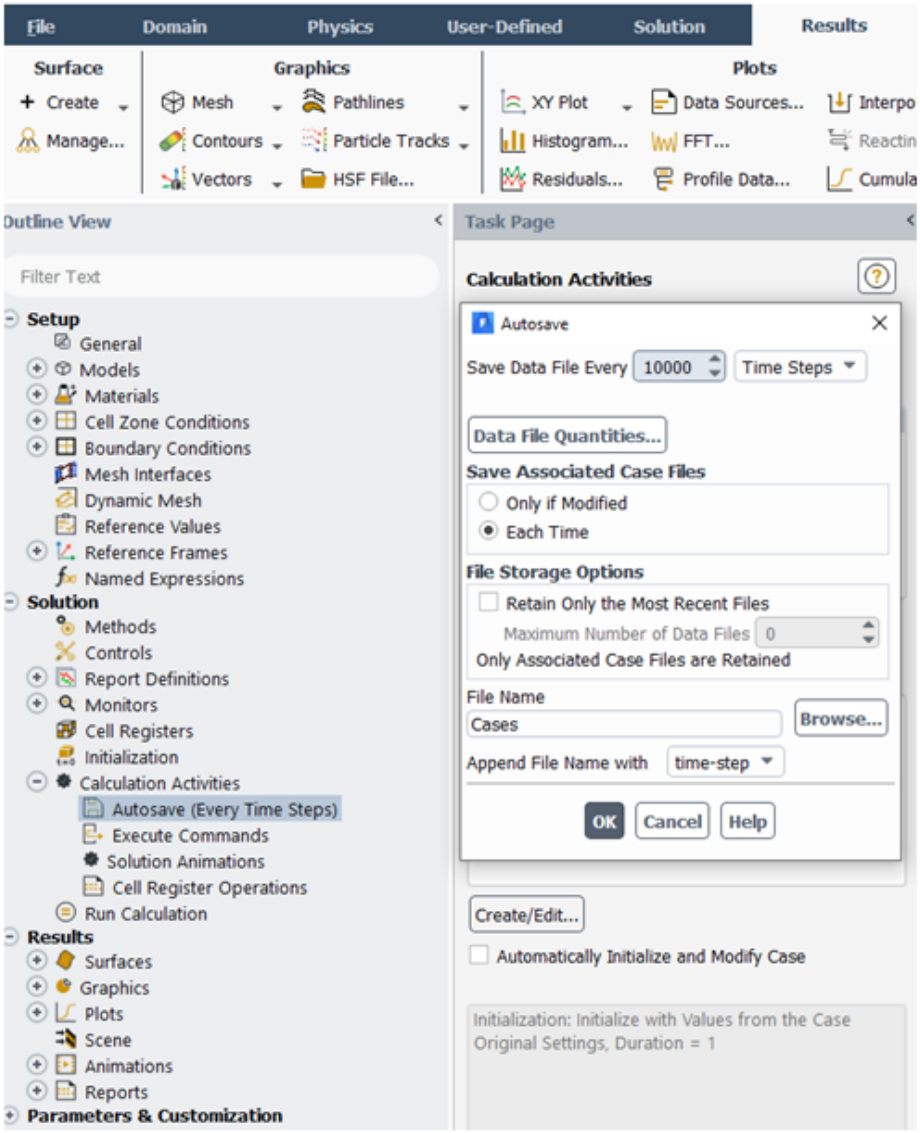

Figure B.21: Autosaving the case and data files

One of the most important types of result visualization is the contours plot. Contours can be plotted to show the distribution of any variable on a surface. To plot the contours of the desired variable, go to Results – Graphics – Contours (shown in

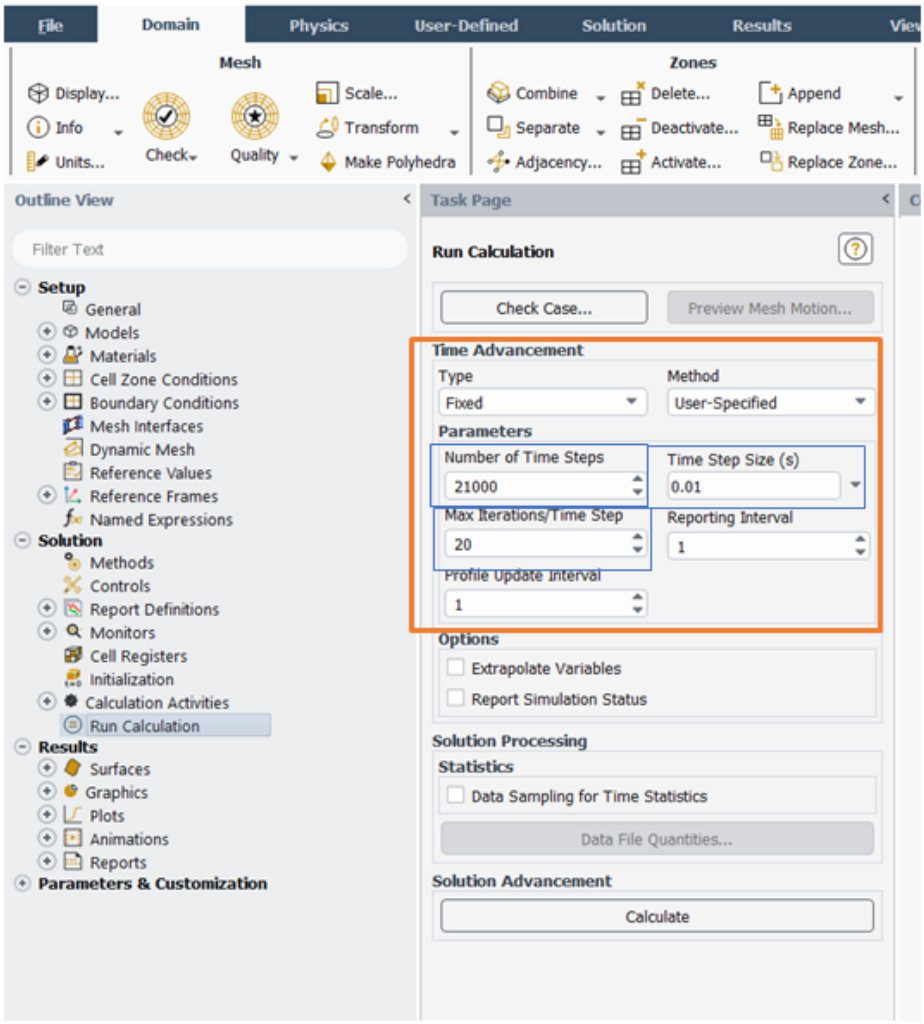

Figure B.22: The transient simulation properties

Figure B.25) In the opened window, the variable, the location, and the phase should be specified. For example, if the concentration distribution of bitumen at 100 m after the inlet is to be plotted, in the first tab, “Phases” and in the second tab “Volume fraction”, bitumen in the third tab and z100 for the surface should be selected.

As mentioned, CFD-post can also be used to process the results and draw a wide

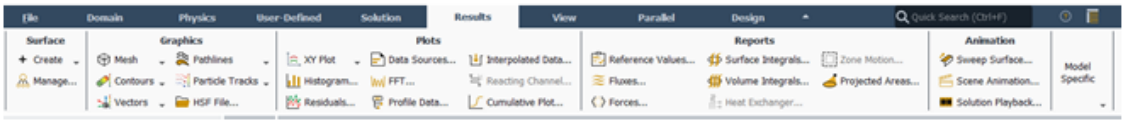

Figure B.23: Overview of the "Results" tab

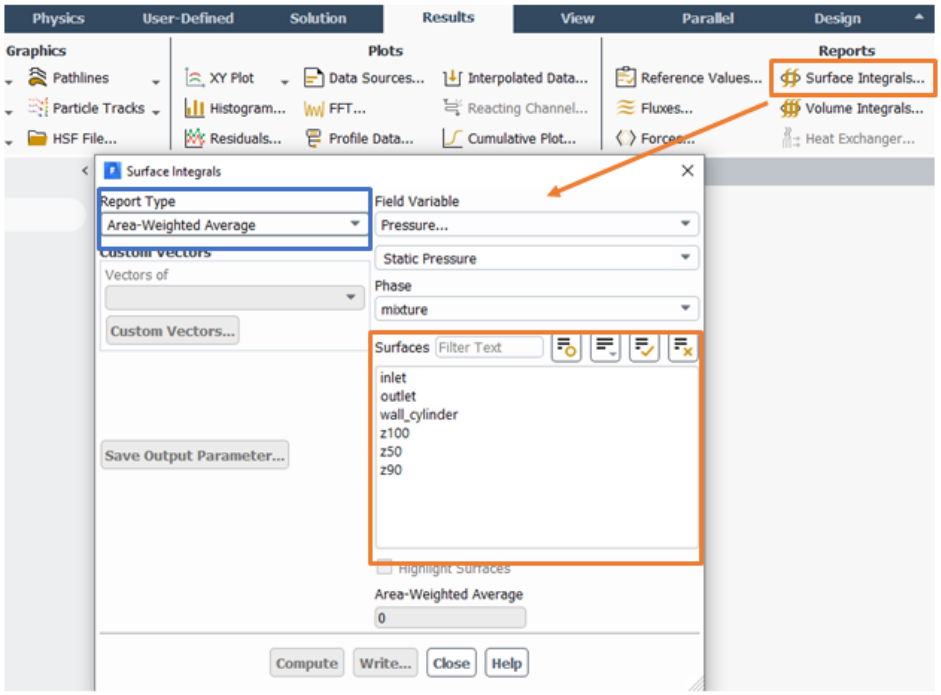

Figure B.24: Calculation of the area-averaged pressure

range of figure types, and export various parameters. It is also possible to export the values of desirable parameters with respect to the location or time and analyze them using other software, such as Matlab or Excel. However, in this document, only the calculation of the pressure drop and plotting the contours of velocity and concentration distribution was explained as the most important features of the multiphase

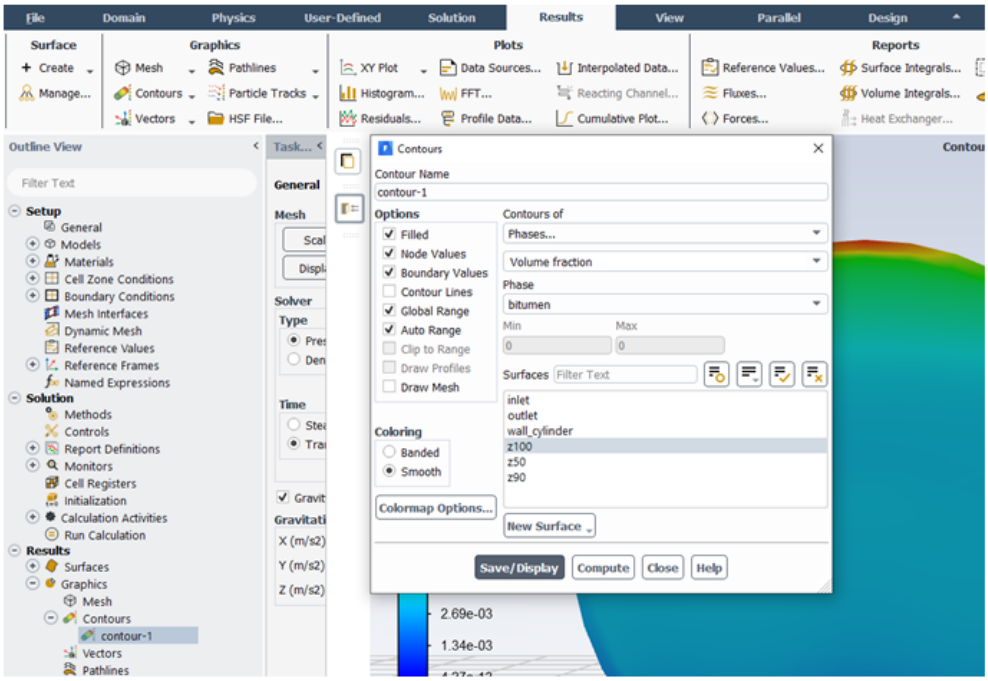

Figure B.25: Plotting the contours of variables

flow.